Electrochemistry of Room Temperature Ionic Liquids with Applications to Electrospray Propulsion

by

Kento Masuyama

Submitted to the Department of Aeronautics and Astronautics
in partial fulfillment of the requirements for the degree of

Doctor of Philosophy

at the

MASSACHUSETTS INSTITUTE OF TECHNOLOGY

June 2016

Author .....
Department of Aeronautics and Astronautics
May 13, 2016

Certified by .....
Paulo C. Lozano
Associate Professor of Aeronautics and Astronautics
Thesis Supervisor

Certified by .....
Martin Z. Bazant
Professor of Chemical Engineering
Thesis Committee

Certified by .....
Manuel Martínez-Sánchez
Professor Emeritus
Thesis Committee

Accepted by .....
Paulo C. Lozano
Chair, Graduate Program Committee

Electrochemistry of Room Temperature Ionic Liquids with Applications to Electrospray Propulsion

by

Kento Masuyama

Submitted to the Department of Aeronautics and Astronautics
on May 13, 2016, in partial fulfillment of the
requirements for the degree of
Doctor of Philosophy

Abstract

Room Temperature Ionic Liquids (RTILs) exhibit a number of physical properties that have opened new doors for technological advancements in space-based micropropulsion, focused ion beam, energy storage, and other research and industrial applications. As a family of concentrated electrolytes, RTIL electrochemical properties deviate from classical theories whose mean-field approach glossed over effects arising from the constituent ions' size and shape. Further development in the understanding of RTIL electrochemistry will drive better design towards enabling technologies, and this research contributes to the growing body of experimental data for RTIL electrochemical behavior with particular focus on applications towards electrospray propulsion devices.

Electrochemical system behavior is governed by interfacial properties, in particular the electrical double layer (EDL). With no neutral solvent to fill the space between ions, the RTIL EDL takes on a complex, multilayered structure which lead to properties distinct from traditional aqueous electrolytes. A direct consequence of the layered structure is a differential capacitance curve that exhibits a local minimum at the potential of zero charge, flanked by two peaks followed by decaying wings. Recent modeling efforts have begun to capture these effects qualitatively, but require further tuning in order to quantitatively describe real systems. An electrochemical cell was designed to allow experimental measurement of capacitance curves, and the curves for two previously unreported RTILs are presented.

The electrochemical window is a limiting potential at which electrochemical reactions start. RTILs typically have large windows on the order of 4–6 V, as compared to the 1.229 V at which water begins electrolysis. In micropropulsion, a large electrochemical window allows for longer continuous operation without adverse reactions. In energy storage, this allows for higher energy capacity by the square of potential. Another way to increase emission duration or capacity is by increasing the available electrode surface area, so that more charge can be stored before breaching the stability window. Porous materials can provide enormous specific areas, with the carbonized resorcinol-formaldehyde synthesized in this work giving approximately $1\,\mathrm{m^2\,g^{-1}}$ of

electrode surface. Through a systematic comparison of this porous electrode and a flat metal electrode, it was confirmed that an electrode with mean pore size of approximately 2 µm locally exhibits the same impedance as at a nonporous surface.

Two electrospray emitter devices were used to study the charging dynamics of flat and porous electrodes under constant current charging. Electrode charging was observed to be governed not only by capacitance, but also by ion species, current polarity, current magnitude, and ion transport dynamics. Using the Scalable ion Electrospray Propulsion System, a 480-emitter thruster developed in the Space Propulsion Laboratory at the Massachusetts Institute of Technology, it was also shown that large charging currents saturated the effects of current magnitude and resulted in charging dynamics that collapse together when parametrized by surface charge density. The work concludes by using the observed trends to propose several guidelines for future electrode design in electrospray applications.

Electrospray propulsion in particular promises to become an area of concentrated research as micro- and nano-satellites enter the market. Current propulsion systems cannot be effectively miniaturized for use on such platforms, but electrospray thrusters have demonstrated packaging in the $1\,\mathrm{cm}^3$ range including the fuel reservoir. In addition, the next step in the recently popular field of gravitational waves will employ space-based observatories, with the LISA Pathfinder technology demonstrator testing an RTIL-based propulsion system for its fine resolution control. It is the hope of the author that the work presented here will contribute to the further refinement of theoretical understanding of RTILs and provide guidance in the design of future RTIL-based technologies.

Thesis Supervisor: Paulo C. Lozano
Title: Associate Professor of Aeronautics and Astronautics

Committee Member: Martin Z. Bazant
Title: Professor of Chemical Engineering

Committee Member: Manuel Martínez-Sánchez
Title: Professor Emeritus

Acknowledgments

As I look back on the adventure that was my graduate experience at MIT, I am truly in awe of the many connections that I've made, both professionally and personally. To my friends from the entering class of 2010, man did we have some fun times. To the Graduate Association of Aeronautics and Astronautics, thank you for providing me with a forum to give to the community from which I would get so much more in return. And to the Japanese Association of MIT, thank you for allowing me to reconnect with my roots, to redefine my sense of identity, and to pretty much do anything I wanted. And of course, thank you to all of my teammates in the various sports I played over the years for giving me a venue to vent my competitive spirit and stress.

I'd like to thank my advisor Professor Paulo Lozano, committee members Pros. Manuel Martínez-Sánchez and Martin Bazant, thesis proposal evaluator Prof. Alan Grodzinsky, and thesis readers Prof. Mark Bathe, Dr. Yu-Hui Chiu and Dr. Carmen Guerra Garcia. Paulo pushed me through all of the ups and downs and provided me with the framework with which I could keep moving in the right direction. Martin introduced me to many helpful collaborators along the way, and even allowed me the use of his own equipment when his own group was competing over its use. I'd be remiss if I didn't mention my labmates - thank you for all of the help and support you've given me, from making electrodes/needles/circuits, setting up computers, to running experiments. Speaking of making things, thank you Todd for not kicking me out of the machine shop even though I'd always show up as you were trying to leave. My experience with research started with SSDL at Georgia Tech under Profs. Bobby Braun and David Spencer. My time at MIT started with the support of the MIT Energy Fellowship, funded by Lockheed-Martin. The opportunity you gave me of testing alternative energy generation in Antarctica is one I will never forget. The National Science Foundation Graduate Research Fellowship Program supported me the next few years, as I learned how to conduct research under Prof. Steven Barrett's tutelage. I couldn't have handled all of the changes in funding and getting through

the labyrinth of the course 16 graduate program without Beth Marois's guidance.

Finally, thank you to my family for giving me the freedom to pursue my dreams.

Contents

Chapter 1

Introduction

1.1 Motivation

Room temperature ionic liquids (RTILs) are a class of solvents offering improved capabilities as propellant in micropropulsion [1–7], as electrolyte in energy storage systems including supercapacitors [8–10] and batteries [11], as ion source in focused ion beam systems [12], in electrodeposition [13], organic synthesis [14, 15], catalysis [16], lubrication [17], and other applications. They are similar to molten salts in that they are purely ionic; although the exact melting temperatures differ, they are liquid at temperatures near room temperature. There are countless options of cations and anions to be chosen for particular applications, and this selection allows for the tuning of physical parameters such as conductivity, viscosity, and reduction and oxidation potentials. The electrochemical window of stability, the range of potentials between the reduction and oxidation potentials, tends to be wider than in traditional aqueous solutions, and can be as large as 3–5 V [18, 19]. This allows for much higher energy storage, which varies as $\propto V^2$, as well as synthesis and deposition techniques at higher potentials than were previously available.

Ionic liquids offer several distinct advantages as propellant for micropropulsion technologies. The negligible vapor pressure [20] allows for storage without large and massive pressurized vessels. Furthermore, controlled exposure to the vacuum environment will serve as a passive purification method, as gas contaminants including

water will selectively evaporate. The expected operating environment for many micropropulsion applications, i.e. low Earth orbit, spans a temperature range in the vicinity of room temperature (for black body reference sphere) [21]. At these temperatures many candidate ILs are in liquid phase, obviating dedicated heating elements in propulsion system design. Finally, as ionic liquids consist of cations and anions as opposed to ions and electrons as in conventional plasmas used in traditional electric propulsion (EP) systems, emitted ion beams can be of either polarity. With use of paired thrusters operating in opposite polarities, or with voltage alternation at each thruster [22, 23], spacecraft charging can be controlled and neutralizers become unnecessary. These unique advantages permit footprints far smaller than traditional EP technologies.

Electrospray propulsion can be classified into two groups: droplet emission [24] and ion emission [25]. Droplet, or cone-jet, emission gives relatively high thrust at high efficiency, whereas pure ion emission allows for even higher efficiency at reduced thrust. Although mixed modes are possible [26] (and to date more often observed experimentally), they suffer from decreased efficiency, with polydispersive losses becoming significant. Electrospray emission has yet to attain levels of maturity required for widespread application; this is due to a lack of understanding of emission physics and the corresponding lack of systematic design tools. Electrospray emitters, which serve the dual functions of transporting propellant to the emission site and amplifying the electric field with its geometry, are clearly integral components of electrospray systems; however, these are currently designed via ad-hoc methods with no well-established rules for optimization. Likewise, candidate ionic liquid propellants are selected based on trial-and-error, with loose guidelines based on conductivity and ion masses. Finally, electrochemical reactions at the electrode in contact with the propellant have been observed as life-limiting factors, degrading both electrode geometry and ionic liquid composition. Better understanding of the RTIL electrical double layer (EDL) structure and dynamics will provide keys towards better propellant selection, thruster design, and operational parameters.

1.2 Classical Double Layer Models

Electrical double layers form at the interface of a fluid in contact with another phase, often a solid electrode. Charged species are attracted to the interface by several potential mechanisms, including electrostatic forces and chemical reactions. The concept of double layers was introduced in the nineteenth century by Hermann von Helmholtz, who was studying electrodes, or electronic conductors, in contact with electrolytes, or ionic conductors. Helmholtz recognized that charged electrodes would repel coions while attracting counterions, creating a local imbalance in charge manifested as two layers of opposite polarity across the interface. His model of the double layer was but the first in a series of advancements, with work continuing to this day.

1.2.1 Helmholtz Model

Helmholtz gave the first description of the double layer in 1853 [27], imagined as a single sheet of charged particles shielding the charge on the electrode surface. The potential in such a model decays linearly over a distance equal to the closest approach of counterions. This distance is defined by the outer Helmholtz plane (OHP), drawn through the centers of the counterions separated from the electrode surface by a single solvation shell, a monolayer of solvent molecules. The stored charge is linear with the applied potential. Fig. 1-1 shows a schematic of this double layer structure and its corresponding potential profile.

The Helmholtz double layer model is essentially two sheets of opposite charge $\pm q$ separated by a distance $\delta = x_{OHP}$, analogous to parallel plates separated by a dielectric otherwise known as a capacitor with capacitance

$$C = \frac{q}{\Phi} \tag{1.1}$$

where Φ is the potential across the double layer. From parallel plate capacitor theory, $C \propto \frac{1}{\delta}$. As the double layer models become more sophisticated, the charge is not necessarily linear with potential. In such cases, a more useful measurement is

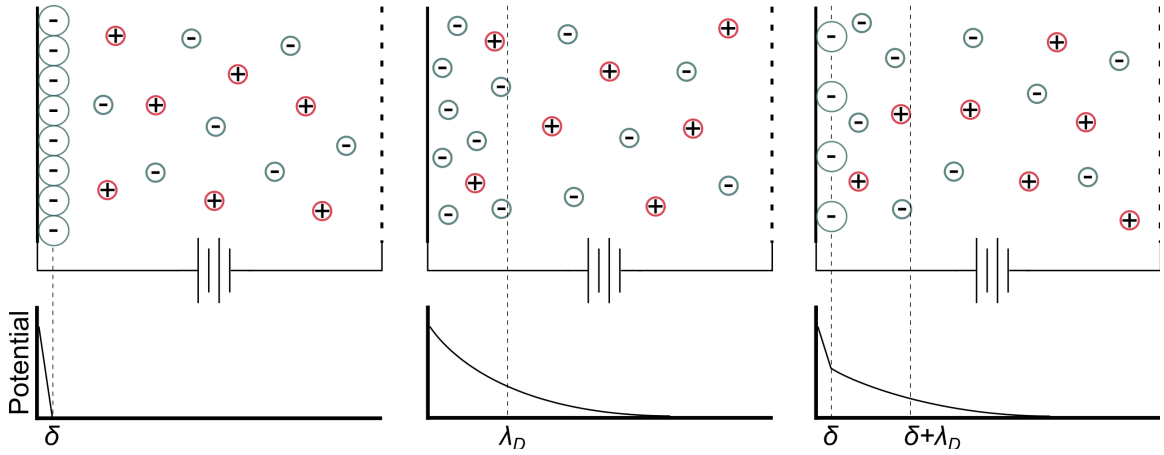

Figure 1-1: Structure and potential drop of classical double layer models. Large circles represent ions surrounded by a solvation shell which make up the compact layer. Left: the Helmholtz double layer relies on a single sheet of counterions to fully screen the field imposed by the electrode charge. Center: the Gouy-Chapman model predicts a diffuse double layer with exponentially decaying potential over a characteristic scale of the Debye length. Right: the Stern model combines the compact and diffuse layers.

differential capacitance,

$$C_d = \frac{d\sigma_q}{d\Phi} \tag{1.2}$$

the derivative of surface charge density σ_q with respect to Φ. In the Helmholtz model, ${}^{C}/_{A} = C_d$ for an electrode of area A, and is given (per unit area) by

$$C_d^H = \frac{\epsilon}{\delta} \tag{1.3}$$

where $\epsilon = \epsilon_r \epsilon_0$ is the permittivity of the electrolyte, ϵ_r is the relative static permittivity (sometimes referred to as the dielectric constant), and ϵ_0 is the vacuum permittivity.

1.2.2 Gouy-Chapman Diffuse Double Layer

In the early twentieth century, Louis Georges Gouy (1910) and David Leonard Chapman (1913) independently discovered that the capacitance at an electrode|electrolyte interface varies with applied potential as well as ion concentration, which could not be explained by the Helmholtz model. Gouy suggested that the ions in solution do not form a rigid sheet in contact with the surface, but rather form into a diffuse

layer governed by the electrostatic potential and the kinetic energy or thermal motion of the ions [28]. This balance can be described by Boltzmann statistics, and ion concentration is distributed according to

$$c_i(x) = c_{i0} e^{\frac{-z_i F \Phi(x)}{RT}} = c_{i0} e^{\frac{-z_i e \Phi(x)}{k_B T}} \tag{1.4}$$

where c_i is the concentration of the ith species at distance x from the surface, c_{i0} is the bulk ion concentration, z is the ion valence, F is Faraday's constant, R is the gas constant, T is temperature, e is elementary charge, and k_B is Boltzmann's constant. This, combined with the Poisson equation

$$-\nabla \cdot (\epsilon \nabla \Phi(x,t)) = \rho_e(x,t) \tag{1.5}$$

where ρ_e is charge density defined as

$$\rho_e = e(c_+ - c_-) \tag{1.6}$$

gives the Poisson-Boltzmann (PB) equation

$$-\rho_e = \epsilon \nabla^2 \Phi = e c_0 \left(e^{\frac{ze\Phi}{k_B T}} - e^{\frac{-ze\Phi}{k_B T}} \right) \tag{1.7}$$

formulated here for a $z:z$ electrolyte, in which $c_{+0} = c_{-0} = c_0$ is equal for both species and the permittivity does not vary across space.

For the limit $\frac{zF\Phi}{RT} \ll 1$ (or equivalently $\Phi \ll \frac{k_B T}{e}$, the thermal voltage), the PB equation can be linearized about zero electrostatic potential to give the Debye-Hückel equation [29], which in a one dimensional geometry gives the exponentially decaying potential profile

$$\Phi(x) = \Phi_0 e^{-\frac{x}{\lambda_D}} \tag{1.8}$$

This is graphically represented in Fig. 1-1. In this equation, λ_D is the characteristic length over which the potential decays from Φ_0 at the wall into the electrolyte. This

is called the Debye length, and is given by

$$\lambda_D = \sqrt{\frac{\epsilon RT}{2c_0 F^2 z^2}} \tag{1.9}$$

for symmetric $z : z$ electrolytes. The total charge density can be calculated by integrating ρ_e over x from the wall to infinity, and then differentiated by Φ to give differential capacitance

$$C_d^{DH} = \frac{\epsilon}{\lambda_D} \tag{1.10}$$

In this low voltage limit, the capacitance behaves as parallel plates separated by the Debye length.

For higher voltages, the full nonlinear PB equation must be solved. Again for symmetric $z : z$ electrolytes, the exponential terms can be replaced with a hyperbolic sine, yielding a differential capacitance

$$C_d^{GC} = \frac{\epsilon}{\lambda_D} \cosh\left(\frac{zF\Phi_0}{2RT}\right) \tag{1.11}$$

This suggests a "parabolic" curve with the Debye-Hückel capacitance as the minimum and increasing capacitance with increasing potential.

1.2.3 Stern Model

The Gouy-Chapman model breaks down at high potentials, due to modeling ions as point charges. As the surface potential is increased, the concentration of counterions near the surface reaches unphysical values. In 1924, Otto Stern proposed a model combining the Helmholtz and Gouy-Chapman models, with the diffuse layer modified to accomodate a plane of closest approach on the order of the ionic radius in attempt to account for the finite size of ions [30]. As the surface potential increases, a subset of ions would adhere to the surface in an analogous form to the Helmholtz model with their centers aligned at the OHP. The potential then is a continuous piecewise function comprising a linear component for the Stern layer and an exponential decay for the diffuse layer. See Fig. 1-1 for an illustration. An additional component of

the Stern model is the shear plane, beyond which ions are mobile. The shear plane lies some distance past the inner Stern layer, and is typically empirically obtained for specific electrode and electrolyte systems. The potential at the shear plane is defined as the ζ potential.

In the Stern model, the electrode charge q is balanced by the sum of the charges in the compact and diffuse layers. The equivalent circuit then is a series of two capacitors,

$$\frac{1}{C_d^S} = \frac{1}{C_d^H} + \frac{1}{C_d^{GC}} \tag{1.12}$$

in which the smaller of the two capacitances dominates overall capacitance.

1.2.4 Further Improvements

In both the Helmholtz and Stern models, the plane of closest approach is defined assuming a monolayer of solvent covering the electrode. In 1947, David C. Grahame recognized the possibility of specific adsorption, in which ions or neutrals come in direct contact with the electrode surface [31]. The plane through the centers of the specifically adsorbed ions defines the inner Helmholtz plane (IHP). The adsorbed ions are not necessarily counterions, and thus the magnitude of potential at IHP may be larger than at the electrode surface. With spherical ions, the potential profile will be divided into three segments, linear from the wall to IHP, linear from IHP to OHP, then exponential decay in the diffuse layer.

Although the solvent has been largely ignored thus far, dipolar solvents including water must have some interaction with the electric field. The effect of solvent molecules was farther elaborated in 1963, when Bockris, Devanathan, and Müller proposed a model recognizing the dependence of the solvent molecule alignment on excess charges at the electrode and the presence of specifically adsorbed ions [32]. For new ions to become adsorbed, work is required to shed the solvation shell and to remove the solvent molecule from the interface. The strong alignment of water dipoles affects the local permittivity of the solvent.

Starting around this time, electrochemical capacitors using activated carbon elec-

trodes became a hot research topic. In subsequent decades, the concept of pseudocapacitance due to reversible Faradaic charge-transfer processes was discovered and used to describe the significant increase in capacitance compared to earlier electrolytic capacitors. In particular, Brian E. Conway's work on ruthenium oxide electrochemical capacitors clarified the differences between battery, double-layer capacitor, and supercapacitor energy storage mechanisms [33]. Supercapacitors not only store charge in the Helmholtz double layer, but also in pseudocapacitance due to reversible redox reactions, intercalation, and electrosorption processes. The rate of such electron transfer redox reactions, in which no chemical bonding takes place, was theorized by Rudolph A. Marcus [34–40], for which he won the Nobel Prize in Chemistry in 1992.

The above summary of double layer theory development has focused on traditional electrolytes, in which solvent concentration is much larger than ion concentration. For example, ionic concentrations in typical electrolytes may be on the order of µM ($1 \times 10^{-6}\,\mathrm{mol\,L^{-1}}$) to 1M, whereas the concentration of pure water is 55.5M. However, as electrode potential is increased, the local concentration at the surface may reach a point where molecular crowding effects no longer allow the assumption of point-like charges, and measurements such as C_d deviate from the theory. For many electrolytes this is not a problem, as the breakdown of electrolyte and the onset of Faradaic reactions limits potential increase. However, in RTIL electrolytes with no solvent and high ionic concentration, this is a critical issue. With the rise in interest of RTIL electrolytes for a variety of applications, recent decades have seen a number of theoretical constructs predicting the structure and behavior of EDLs in such systems, to be discussed in Ch. 2.

1.3 Ion transport

The double layer theories above describe the locations of ions in a static picture, but many applications including electrospray require ion transport. A commonly applied model is the Poisson-Nernst-Planck equations. Starting from mass conservation

assuming incompressibility $\nabla \cdot \mathbf{u} = 0$,

$$\frac{\partial c_i}{\partial t} + \mathbf{u} \cdot \nabla c_i + \nabla \cdot \mathbf{J}_i = R_i \tag{1.13}$$

where $\mathbf{u}$ is fluid velocity, t is time, $\mathbf{J}_i$ is flux density of species i, and R_i is the production rate by reactions. Assuming a flux density of the form $\mathbf{J}_i = -\kappa_i c_i \nabla \mu_i$ where κ_i is mobility and $\mu_i = k_B T \ln a_i + z_i e \Phi$ is electrochemical potential, the Nernst-Planck equation for a dilute ideal solution (chemical activity equals concentration, $a_i = c_i$) without reactions can be expressed as

$$\frac{\partial c_i}{\partial t} + \mathbf{u} \nabla c_i - \nabla \cdot \left[D_i \left(\nabla c_i + \frac{z_i e c_i}{k_B T} \nabla \Phi \right) \right] = 0 \tag{1.14}$$

where the Einstein relationship $D_i = \kappa_i k_B T$ was used for diffusivity D_i [41]. Combining with the Poisson equation (Eq. 1.5) gives the full set of the Poisson-Nernst-Planck (PNP) equations. In applications to typical electrochemical systems where system size scale $L \gg \lambda_D$ and the bulk is electroneutral, matched asymptotic expansion becomes necessary. The derivation of the PNP equations assumes dilute solutions similar to classical double layer theories, and corrections must be made in order to accurately describe concentrated electrolytes such as RTILs [42]. These corrections are then equivalent to the work reviewed in Ch. 2 for the double layer. Applications to porous electrodes such as those used in the experiments of Ch. 4 and 5 require further adjustment, which have been documented considerably in literature [43–45].

In the case of electrosprays, the transport of ions from the reservoir to the emitter must agree with the ion emission characteristics. Electrospray emission takes place at stable structures similar to Taylor cones, which form due to the balance between electric traction, surface tension, and hydrodynamic pressure [46]. A set of electrohydrodynamic equations, the Taylor-Melcher "leaky-dielectric" model, was developed in part to investigate the deformation of fluids with finite conductivity under electric fields (summarized by Saville [47]). Although further development of the Taylor cone emission characteristics is beyond the scope of this thesis, concepts from the leaky-dielectric model have been applied to RTIL menisci; in particular Higuera has

proposed a model for charge transfer and ion evaporation in pure ionic mode [48] and recent simulation studies by Coffman have identified meniscus geometries that deviate from the strict Taylor cone [49].

1.4 Goals of this Work

Understanding of the RTIL EDL has greatly improved in the past few decades, through theoretical developments, numerical simulations, and experimental investigations as will be covered in Ch. 2. Due to the innumerable possible combinations of RTILs and electrode surfaces, further developments in understanding the exact behaviors of EDLs may require atomic resolution studies, whether by abandoning mean-field methods theoretically or by using sub-nanometer scale experimental methods such as atomic force microscopy. Another path forward exists, specifically for engineering purposes. New continuum formulation models intentionally obscure specific interionic interactions, thereby reducing computational cost while retaining the minimum necessary fidelity. With the purpose of this thesis being application of RTIL EDL theory to practical electrospray propulsion systems, a computationally tractable theory that is able to capture important qualitative features allows for rapid development without resorting to ad hoc methods. Theories are only as good as the real-world trends they can capture and therein lies a problem, that experimental data exists for so many different systems and the observed trends are not always consistent. This thesis work seeks to address these issues in a manner that will contribute generally to the field of RTIL studies as well as use electrospray propulsion as a particular case of focus. Broadly, the contributions of this work are:

- **A common experimental system for various electrochemical techniques**. In order to remove the variability in data due to differences in materials and conditions, the same electrochemical cell was employed in conducting multiple electrochemical experiments, to be detailed below. Although electrode materials and RTIL formulas are available in literature, preparation of specific electrode surfaces and RTIL samples may give rise to anomalous differences;

capacitance is known to vary drastically with surface material and geometry as well as electrolyte purity. By repeating the same procedures in preparation for each test, the use of a single common setup enhances the ability to compare data across different measurement methods. This then allows for the generated data to be used more consistently in tuning theoretical models, such as future extensions of the Bazant, Storey, and Kornyshev model [50] and related continuum theories (refer to Ch. 2). Key aspects that present the next challenges in such models may include ion size asymmetry and deviation from spherical ions.

- **Comparison of flat and porous electrode interactions with ionic liquids**. Porous electrodes are known to introduce complexities to double layer behavior. The double layer must diffuse into the porous matrix, introducing an additional time dependence into the electrode charging dynamics. However, once the ions have been transported to a given local wall surface, does it behave the same as a flat electrode? By comparing electrochemical behavior using the same ionic liquids prepared in the same manner, but in two cells using a flat versus a porous electrode, the local interfacial behaviors can be related.

- **Electrospray propulsion case study**. Electrochemical effects are potential life-limiting factors in electrospray propulsion. Although methods have been developed to mitigate such effects, better understanding of their causes will enable better design principles. Topics that may be clarified with the newly developed tools include new propellant identification, ion transport mechanisms in porous emitter structures, and charging dynamics to set critical frequencies for voltage alternation. This results in deeper insight into the governing parameters of electrode design, particularly with regards to electrode and liquid pathway geometries.

Chapter 2

Literature Review

2.1 Ionic Liquid Double Layer Studies

The inherent customizability of ionic liquids offers possibilities for drastic improvement in a number of techniques and technologies. RTILs are generally stable up to higher potentials than aqueous electrolytes, as there are no solvents to be decomposed. Ion concentration has been included in double layer models since Gouy-Chapman, but traditional models were all formulated in the dilute limit to reflect the aqueous electrolytes in common use. An early class of concentrated electrolytes to garner attention was molten salts, with the formulation of a linear capacitance model in 1964 by Dogonadze and Chizmadzhev [51]. Molten salts are similar to RTILs in that they are ionized liquids without solvent, but applications are limited due to the extreme temperatures necessary to maintain liquid phase. Understanding of the molten salt behaviors often serves as a reference point for RTIL development; diffuse layer capacitance has been derived from Poisson-Boltzmann [52], simulations on electrode charge and temperature dependences have been conducted [53], and reviews are available to provide more theory and data [54, 55]. The high concentration in molten salts and RTILs indicate that steric effects of finite ion size become important. The exact nature of these effects is still under investigation, and this literature review will cover previous works from three approaches, theoretical, computational, and experimental. For a more complete review, refer to reference [56]. A review of RTIL application to

electrospray thrusters is presented in the following section.

2.1.1 Theoretical Developments

The necessity of including volume restriction into double layer theory was recognized as early as the 1940s, when Bikerman made modifications to the Gouy-Chapman-Stern (GCS) DL model [57]. Namely, two correction factors were introduced, one to account for finite ion volume and another to account for the work necessary to displace water dipoles within an electric field. This second correction is related to the relative polarizability of solute and solvent, as discussed by Gouy [58], Frumkin [59], and Butler [60]. Application of this modified theory to mercury|electrolyte interfaces showed that at high potentials, the equivalent double layer thickness is independent of concentration and only weakly dependent on potential; furthermore, it showed a capacitance maximum at low potentials and nearly constant capacitance at high potentials. Eigen and Wicke modified Debye-Hückel theory to include corrections for space requirement not just of ions but also their hydration shells, and also for incomplete dissociation [61]. A finite number of "places" were either occupied or not by finite size particles, in an analogous framework to adsorption statistics and Eucken's treatment of hydration shells [62]. Depending on polarity, hydration shells of neighboring ions were either impenetrable or partially penetrable, and charge density profiles were derived for both cases showing deviations from different terms in the Boltzmann distribution.

Bohinc et al. approached the problem with statistical mechanics, incorporating the excluded volume effects into the lattice statistics while using a mean-field view for the electric field [63]. Application of this framework to a charged cylinder in electrolyte solution revealed decreased counterion density and increased potential in the region surrounding the interface, with enhanced results due to higher potential or larger ion size. A limit in counterion density was observed in the form of a saturating ratio of ion density at the surface to bulk, a feature unobserved in dimensionless, point-like ions. Borukhov obtained similar results in looking at counterion distribution using a modified Poisson-Boltzmann (MPB) formulation, in which the Stern layer

is allowed to increase beyond a monolayer and solvent entropy is considered [64, 65]. Counterion adsorption around a cylinder, called the *Manning condensation*, and the subsequent partial charge screening or renormalization had been observed experimentally in biological systems; Borukhov's solution found that excluded volume effects reduce condensation, although at the limit of infinite dilution this reduction vanishes due to the extended condensation layer. Analogous charge renormalization occurs around spheres, but due to the finite width of the condensation layer, this effect can persist at high dilution. Antypov also used an MPB approach, introducing a criterion for the onset of hard-core effects; furthermore several previously proposed local density functional approaches were dismissed and a nonlocal excess free energy using a constant-weight approach was employed instead [66]. The model applied around a charged macroion was in good agreement with Monte Carlo results for weakly correlated electrolytes, and at stronger correlation showed the layering effect first seen in Monte Carlo results [67] and explained in molten salts [54].

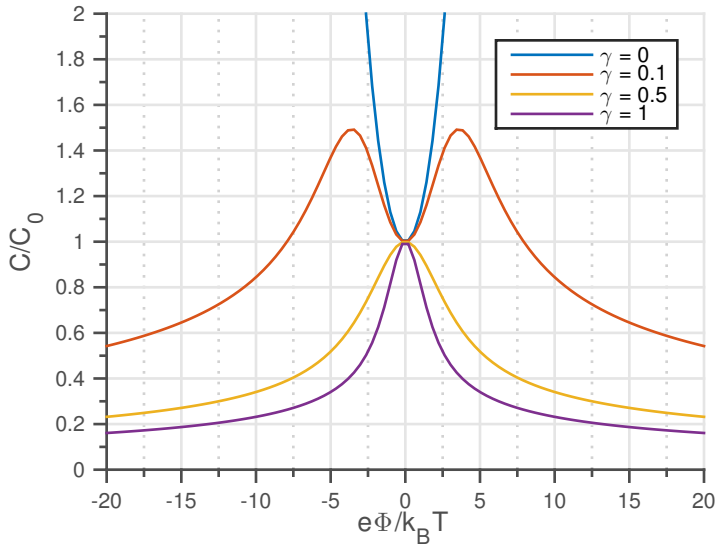

Figure 2-1: Capacitance curves generated by Kornyshev's model incorporating the lattice saturation parameter γ. The $\gamma = 0$ case is equal to Gouy-Chapman.

In 2007, Kornyshev proposed a mean field theory (MFT) with excluded volume effects specifically for the consideration of RTILs [68]. RTIL capacitance-potential curves could not be rationalized with existing theory, in which the capacitance mini-

mum is expected at the potential of zero charge (PZC). The electrolyte was modeled in a lattice-gas form with a free energy expression consisting of potential, short-range interactions, and ion distribution entropy. A simple case of symmetric ion sizes, and thus equal potential of short-range interaction, was solved analytically by neglecting said interactions and assuming constant volume, resulting in a Fermi-like distribution:

$$c_{\pm}(x) = c_0 \frac{e^{\frac{\pm e\Phi(x)}{k_B T}}}{1 - \gamma + \gamma \cosh \frac{e\Phi}{k_B T}} \tag{2.1}$$

A lattice saturation parameter $\gamma = {}^{\#\text{ occupied sites}}/_{\#\text{ total sites}}$ was introduced, and the limit $\gamma = 0$ gives Eq. 1.11, the Gouy-Chapman expression for differential capacitance. For nonzero values of γ, the differential capacitance is given by the expression

$$\frac{C_d^K}{C_d^{DH}} = \frac{\cosh \frac{e\Phi_0}{2k_B T}}{1 + 2\gamma \sinh^2 \frac{e\Phi_0}{2k_B T}} \sqrt{\frac{2\gamma \sinh^2 \frac{e\Phi_0}{2k_B T}}{\ln\left(1 + 2\gamma \sinh^2 \frac{e\Phi_0}{2k_B T}\right)}} \tag{2.2}$$

where C_d^{DH} is the linear Debye-Hückel capacitance, Eq. 1.10. Two new curve shapes were identified with increasing γ, a "camel" shape with local minimum at PZC at small γ and a "bell" shape with maximum capacitance at PZC for large γ, shown in Fig. 2-1. The $\gamma \neq 0$ curves do not show exponentially rising wings, indicating a different relative importance of the compact and diffuse layer capacitances. The solution solved in this work produced a potential profile which monotonically decreased at a less steep slope than Gouy-Chapman; for future consideration, different types of possible screening of the electrode charge were qualitatively discussed. The first was overscreening (also overcharging), a phenomenon made favorable by correlation [69] in which the first layer of counterions provides more charge than necessary to screen the electrode surface charge and the next layer of coions must compensate, leading to an oscillatory structure. Higher surface charges may not be fully shielded by a packed first layer and thus multiple layers form, leading to lattice saturation; this effectively increases the double layer thickness with potential, giving rise to the C_d inverse-square-root decay observed at high γ. The specific case of $\gamma = 1$ was recreated exactly from a GCS formulation assuming uniform permittivity but with changes to Boltzmann

energy due to ion motion replacing other ions instead of neutral solvents [70]. The resulting equation for charge density replaced the hyperbolic sine in the classical solution (integral of equation 1.11 with respect to Φ) with a hyperbolic tangent, meaning similar profiles far from the surface but with significant differences nearby. Henderson grafted the GCS model to the mean spherical approximation (MSA) in order to take advantage of the two theories' accuracies at low concentration and at low potential, respectively [71].

Bazant, Storey, and Kornyshev improved on the model in 2011, developing a continuum model (BSK) with crude approximations for individual interactions but enough fidelity to capture overscreening and crowding effects [50]. The free energy is described by a Landau-Ginzburg-like functional with terms typically used in ionic liquids, ionic crystals, and electrolytes, and an additional potential gradient term including the electrostatic correlation length l_c. This results in a modified Poisson equation:

$$\epsilon \left(l_c^2 \nabla^2 - 1 \right) \nabla^2 \Phi = \rho_e \tag{2.3}$$

which, coupled with the concentration distribution of Eq. 2.1, gives

$$-\rho_e = \epsilon (1 - l_c^2 \nabla^2) \nabla^2 \Phi = 2ec_0 \frac{\sinh\left(\frac{e\Phi}{k_B T}\right)}{1 + 2\gamma \sinh^2\left(\frac{e\Phi}{2k_B T}\right)} \tag{2.4}$$

a "Poisson-Fermi" equation as opposed to the "Poisson-Boltzmann" (Eq. 1.7). This theory, applied to a half space with symmetrical spherical ions, captured molecular scale charge density oscillations and the formation of a condensed layer of counterions extending into bulk with increasing potential, in agreement with more complex statistical mechanical treatments. These structures are drawn in Fig. 2-2. Differential capacitance dependence was given in three regimes, with a linearization of the model

for low potentials and scaling laws for moderate and high potentials:

$$\frac{C_d^{BSK}}{C_d^{DH}} \sim \begin{cases} \frac{\sqrt{2\delta_c+1}}{\delta_c+1} & |\tilde{V}| \ll 1 \\ \frac{8^{3/4}}{3(\delta_c^2\gamma\tilde{V})^{1/4}} & \frac{128}{81\gamma} \ll |\tilde{V}| \ll \frac{81\delta_c^2}{128\gamma} \\ \sqrt{\frac{2}{\gamma\tilde{V}}} & |\tilde{V}| \gg 1 \end{cases} \tag{2.5}$$

where $\delta_c = {}^{l_c}/_{\lambda_D}$ is a dimensionless correlation length, γ is the volume fraction from Kornyshev [68], and $\tilde{V}$ is the dimensionless potential relative to bulk normalized by thermal voltage. This model is in good agreement with simulations and experiments, and is simple enough for application to dynamic problems.

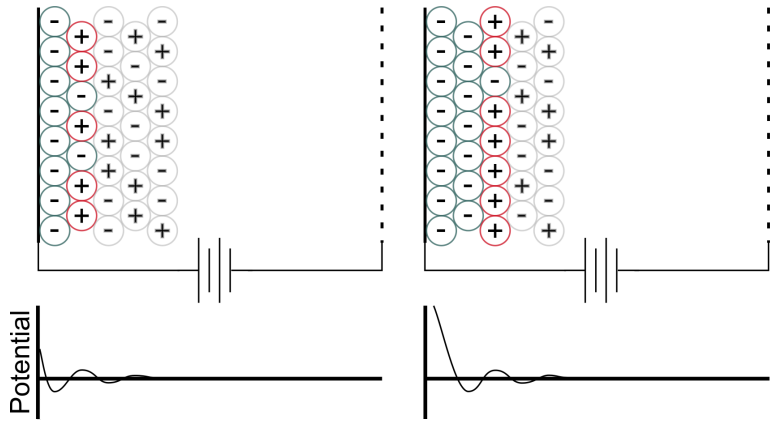

Figure 2-2: Structure [50] and potential drop [72] under overscreening and crowding regimes of charge screening. Unlike the monotonically decreasing potential profiles of classical models (Fig. 1-1), these structures produce an oscillatory distribution of potential and ion concentration.

The most recent works in theoretical development have started to account for ion size asymmetry in continuum formulations. Kilic reformulated Bikerman's solution with explicit accounting of each ion's radius [73]. This solution traced the symmetric solutions for each ion size at the wings, with a smooth transition between the two curves. At small potentials the symmetric solution was independent of ion size, and at larger potentials the double layer is expected to be dominated by one polarity ions; this intuition matches the asymmetric model results. Han et al. used a gas-lattice model as in Kornyshev's derivation, with a new parameter $\xi = {}^{a_-^3}/_{a_+^3}$ which subdivides the lattices to allow for differences in ion diameter, $a_- \neq a_+$ [74]. This allowed for the

derivation of an analytical formula for differential capacitance which simplifies to the Kornyshev model for $\xi = 1$ and furthermore to the Gouy-Chapman model for $\gamma = 0$. The resulting asymmetrical capacitance curves were in good agreement with density functional theory (DFT) simulations, although the model does not allow for explicit overscreening, as was done with electrostatic correlations in the BSK model.

The theories presented to this point were largely static and concerned with EDL structure and capacitance. However, similar approaches have been made to model RTIL EDL dynamics as well. RTILs have been considered for applications in nonlinear electrokinetic processes including electroosmosis and electrophoresis, in which voltages $\gg$ thermal voltage $\frac{k_B T}{q}$ can be applied. Kilic et al. took inspiration from previous efforts to account for steric effects and presented time-dependent equations with excluded volume constraints [42, 75]. In the first part, two simple models built on the MPB work by Kralj-Iglič et al. [76] and Borukhov [65] studied diffuse-charge dynamics in concentrated electrolytes. Charging dynamics were slowed by nonlinearity in a potential range where steric effects were insignificant. Salt adsorption or the electrolyte concentration at the electrode surface was also reduced, suggesting that equivalent circuit RC models should hold up to larger potentials. Surface conduction in the diffuse layer was reduced in importance compared to classical dilute electrolyte models. In the second part, a modified Poisson-Nernst-Planck (MPNP) model was developed and compared against classical PNP on a model one-dimensional parallel plate cell with symmetric $z : z$ electrolyte. MPNP results showed charge buildup in agreement with PNP until concentrations approach the steric threshold (critical voltage $V_{cr} \sim \frac{k_B T}{q}$), after which the EDL thickened at almost constant density. Bazant et al. considered the effect of crowding, arguing that compact layer growth would be accompanied by the shear plane advancing away from the surface [77]. A modified Helmholtz-Smoluchowski equation was derived to show that charge-induced viscosity would increase in the EDL, thereby decreasing electroosmotic mobility. Nanoscale effects which had not been included in previous mean field theories were discussed, and a framework for electrokinetic theory in concentrated solution based on nonequilibrium thermodynamics was suggested. Later, Storey and Bazant accounted for

ion size and electrostatic correlations in developing a continuum electrokinetic theory, using Bikerman's excess chemical potential and the BSK model to formulate a fourth-order modified Poisson equation [78]. Charge density oscillations in correlated electrolytes were seen to reduce electroosmotic flow, and overscreening could even reverse apparent charge of the surface and lead to flow reversal.

Most of the above theories considered simple model electrolytes at metal surfaces. However, in the past several years more complex systems have begun to be studied. Feng et al. laid out a theoretical framework for describing EDL structure and capacitance in both neat RTILs and those mixed with organic solvents [79]. The "counter-charge layer in generalized solvents" (CGS) framework sees the EDL as consisting of a counter-charge layer exactly canceling the surface charge and a bulk of generalized polarized solvents encompassing all remaining RTIL (net neutral ion pairs with dipole moment) and any solvents. The framework is applied to interpret two interesting results from molecular dynamics (MD) simulations, the slight increase in capacitance as organic solvent mass fraction is increased and the difference in capacitance with polarity despite similar distances of closest approach between cation and anion. Kornyshev et al. studied the interaction of two double layers at one interface, one in the RTIL and the other in a graphite electrode [80]. Mean field theory for RTIL as described above was combined with electronic density functional theory for the screening properties of graphite, neglecting short range Coulomb correlations. Experimental observations of U-shaped or almost constant capacitance curves at carbon electrodes suggests capacitance of the semimetal|RTIL interface is dominated by the electrode DL at low potentials and by the RTIL at higher potentials. Recently, Kornyshev and Qiao explored the three-dimensional structure of RTIL EDLs [81]. Classical theory had developed in one dimension, normal to the surface; however, experimental observations had revealed changes in capacitance and dynamics due to transitions between different lateral arrangements of adsorbed ions. Narrow pores provide an interesting case study, in which lateral ion-ion interactions are screened by walls and thus charge can be stored more effectively.

2.1.2 Simulation Work

Computer simulations have proven to be a powerful tool in corroborating new theoretical constructs. Molecular dynamics has been a particularly common tool in investigating RTIL EDLs. Unlike the mean field or statistical methods considered in many of the theories above, MD allows for calculation of intermolecular interactions in an N-body setting, typically through numerical computation of Newton's equations of motion. With careful selection of force fields, which then define potential energy and forces, trajectories of individual molecules can be traced even in complex systems where analytical solutions are infeasible. For reviews on MD analyses on RTILs, see [82–84]

Fedorov considered a dense system of singly charged spheres governed by the Lennard-Jones (LJ) and Coulomb potentials in symmetric [72] and asymmetric [85] ion size cases. Charge density oscillations indicating overscreening were clearly visible at small to moderate potentials, and as the wall charge density was increased beyond the maximum charge available in the first layer of counterions, a second layer of the same charge formed eventually leading to lattice saturation. Capacitance values showed a bell-shape as opposed to the G-C prediction, in good agreement with Kornyshev's MFT predictions. Asymmetric ion sizes also showed a bell-shape capacitance curve, however with the maximum shifted slightly away from the PZC. Fedorov et al. then applied Monte Carlo methods to study the effect of ion topology, concluding that the presence of a neutral tail in addition to the charged head gives rise to the camel shaped capacitance curve [86]. Extra degrees of freedom were introduced by the tail, including rotations and replacements of the neutral tails acting as latent voids. As tail length increased, no new qualitative features were observed but capacitance decreased; at higher potentials in the lattice saturation regime, tails acted not as latent voids but as spacers effectively increasing the EDL thickness.

With increased use of MD and growing interest in an ever-expanding number of RTILs, references for more accurate force fields became necessary. Canongia Lopes and others have developed models based on the Optimized Potentials for

Liquid Simulations-All Atom and Assisted Model Building with Energy Refinement (OPLS-AA/AMBER) framework for calculating force fields for different families of RTILs, to be validated by comparison to simulations and experimental data [87, 88]. Armed with the ability to model specific RTILs, for example the two RTIL models shown in Fig. 2-3, recent studies have focused on a number of specific interfaces. Shimizu reported that realistic renditions of nonuniform amorphous substrates such as glass could capture adsorption and stratification and give similar results to experiments [89]. Specifically, normal density profiles, lateral interfacial structures, orientational ordering, and planar density contours were studied for the interface between a 5 nm layer of the RTIL 1-(2-hydroxyethyl)-3-methylimidazolium tetrafluoroborate [hemim][BF_4] and silica, alumina, and borosilicate glass substrates. Compared to a free surface (vacuum), the presence of glass caused a slight increase in average ion number density and a significant increase in density fluctuations; these density fluctuations were much clearer for the quasispherical anion than the highly asymmetric cation. Another group simulated the interface of the RTIL 1-butyl-3-methylimidazolium bis(trifluoromethylsulfonyl)imide [bmim][Tf_2N] and silica, specifically by recreating the atomic force microscopy (AFM) experimental technique in an MD simulation [90]. Normal force via an effective short-range potential on a spherical mesoscopic probe were obtained as a function of distance from the surface, revealing density oscillations (not charge density) which are not significantly affected by surface charge. Similar results were found for the mica interface [91], and both results were seen to qualitatively agree with experimental results.

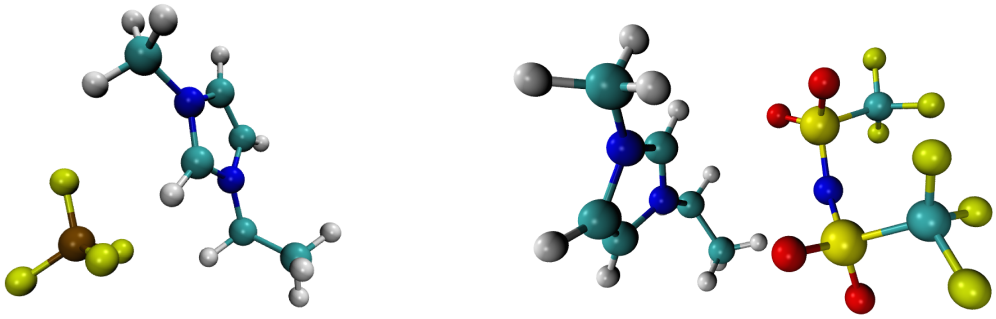

Figure 2-3: Two model RTILs for MD simulations. Left: [emim][BF_4], right: [emim][Tf_2N].

Graphite, a form of carbon with excellent electrical conductivity, and its monolayer equivalent graphene have been popular choices in RTIL interfacial studies. Lynden-Bell et al. studied short-range electric field screening by the RTIL 1,3-dimethylimidazolium chloride [dmim][Cl] at a charged graphene surface [92], and found excellent screening at distances larger than 1–2 nm. Vatamanu et al. studied the effect of graphite surface topology on EDL structure and differential capacitance in 1-alkyl-3-methylimidazolium bis(trifluoromethylsulfonyl)imide [rmim][Tf_2N] ([rmim] also often expressed as [$c_n$mim]) [93]. A rough surface gave higher capacitance than a flat surface, with qualitatively different camel-shaped curves; the effect of longer neutral alkyl tails was a slight increase in capacitance. Also, the capacitance decay scalings predicted by the BSK models were confirmed. Hu et al. extended the work to basal and prismatic graphite as well as (001) and (011) gold surfaces in two RTILs, [bmim][BF_4] and [bmim][PF_6], the latter with the hexafluorophosphate anion [94]. Capacitance for the two RTILs were similar for a given surface, and both corrugated surfaces showed more capacitance variation with potential than their flat counterparts. Specifically, the dimensions of the surface roughness relative to ion sizes was seen to be a driving factor. Si et al. studied two RTILs with a common anion, [dmim][PF_6] and [bmim][PF_6], at charged graphite [95], taking into account the local compressibility as discussed by Kornyshev [68] and manifested in the form of the [bmim] tail acting as a latent void. This results in the [dmim][PF_6] PZC being located at the local maximum of the capacitance curve, whereas the [bmim][PF_6] PZC is at a local minimum. Effects of cation adsorption were also studied, observing that in incompressible RTILs, potential variations near PZC affect not the adsorbed cation layer but the subsequent anion layer thus giving rise to different effective DL thickness. Paek et al. also studied [bmim][PF_6], combining to the MD a DFT description of the quantum capacitance of graphene [96]. Although the RTIL EDL capacitance showed a bell curve, the overall capacitance exhibited the U-shape in line with the calculated graphene capacitance and with experimental data.

MD simulations have also revealed important characteristics of the EDL structure, including transitions between structural regimes. Kirchner et al. used a coarse

grained model RTIL to show the charge-density driven transition from a multilayered alternating EDL to a surface-frozen monolayer of counterions separating the surface from non-structured bulk, referred to as a "Moire-like" structure [97]. At even higher surface charges, the superposition of two ordered monolayers gave rise to a "herring-bone" structure, also seen in experiments. These structural transitions were ascribed to a balance between surface to counterion attraction and interion steric repulsion. Merlet et al. used MD with importance sampling methods to rationalize the inconsistencies between mean-field theories and experimental observations, with the conclusion that abrupt structural changes may explain the anomalous potential dependence of capacitance [98]. Many possible structural changes exist due to the out-of-plane layering of RTIL EDLs, including local ordering of adsorbed ions, reorientation of large molecular ions, and exchange of ions between different layers. A recent short communication provided a summary on charge-driven structural transitions, using a comparison between three coarse-grained LJ sphere models (different ion size ratios) and a fully atomistic MD simulation to show that electrostatic interactions and steric effects are dominant effects [99].

RTIL electrical double layers have also been studied with numerical solutions and asymptotic matching of continuum model equations. Olesen et al. derived matched asymptotic expansions for thin double layers from the PNP equations, with consideration of strongly nonlinear effects including salt depletion near the electrodes and breakdown of the quasiequilibrium EDL structure at AC excitation on the order of the relaxation time [100]. Their results indicate that steric effects suppress the strongly nonlinear regime in concentrated electrolytes, as the EDL is unable to extract large enough numbers of ions from the bulk; weakly nonlinear RC circuit models should thus be applicable at larger voltages. Zhao used matched asymptotic expansions on the BSK model to identify a characteristic length $\sqrt{\lambda_D l_c}$ and characteristic charging time ${\lambda_D^{3/2} L}/{D l_c^{1/2}}$ to describe RTIL EDLs with strong correlations, where l_c is the correlation length as featured in BSK, L is the length scale for the electrochemical cell or system, and D is diffusivity [101]. Furthermore, the absorption of salt by the EDL was found to create a depletion region between the EDL and bulk which could potentially

break down the weakly nonlinear analysis, and a criterion was defined to assess its applicability in terms of various length scales and excess salt concentration. Yochelis used BSK-based modified PNP equations to study effects of ion density, electrostatic correlation length, confinement, and surface properties; variation of these parameters induced transitions between alternating charge layers (overscreening) and a monotonic diffuse layer similar to dilute electrolyte theory [102, 103]. Jiang et al. used a system of symmetric Lennard-Jones spheres to simulate a similar set of RTIL parameters as used in the BSK model and study EDL formation dynamics [104]. Cell potential evolution under constant current charging was found to agree with BSK results at low charging rates, but break down at higher rates as potential oscillations are induced by the sequential formation of ionic space charge layers.

Still other approaches have been proposed to describe the RTIL double layer structure. Density functional theory (DFT), previously applied successfully to aqueous electrolytes, is a computational quantum mechanics model using functionals to describe electronic structure in multi-body problems. DFT was modified for RTIL application, adding the ability to account for excluded volume effects and electrostatic correlations [105, 106]. DFT with hard spherical ions was able to capture the transition from camel to bell shape as predicted by Kornyshev, and showed qualitatively different results from MSA and GCS. Charged interfaces showed the alternating layers of cations and anions, extending beyond 10 times ionic diameter; neutral surfaces showed significant layering only in the case where cation size was much greater than anion size. When the cation was half the anion size, electrostatic interactions were strengthened and layering was reduced. The model gave asymmetric capacitance-potential curves for ions of different size. Ion topology was also considered using neutral segments of monomeric hard spheres in an analogous form to bead-spring models of polymers, and dumbbell shaped cations also formed long-range layering. Addition of solvent molecules, explicitly populated without a bulk dielectric constant in the Coulomb potential, gave effectively the same result as a relatively weak surface charge density, in that the layering structure of higher charge densities was qualitatively retained.

2.1.3 Experimental Studies

Many experimental techniques have been applied to study EDLs in ionic liquids. Traditional electrochemical methods including electrochemical impedance spectroscopy (EIS), electrocapillarity, and voltammetry are commonly employed, although difficulties in interpreting the results have delayed progress and remain presently. Typical electrochemical experiments are conducted in three-electrode cells with working (WE), counter (CE) and reference (RE) electrodes. The WE is the electrode at which the experimental observations are made, and thus its material properties are of importance. The RE's purpose is to provide a stable reference potential against which to measure the WE potential, which depends on the RE material's ability to form thermodynamic equilibrium with the electrolyte; many standards exist for use with traditional electrolytes. However, no such standards exist for use in RTILs and often quasi-reference electrodes (QRE) are utilized, which are not in thermodynamic equilibrium but are able to provide a somewhat stable potential at least for the duration of the experiment. As many RTILs are hydrophilic, the electrochemical cells are typically kept under vacuum or in an inert atmosphere such as argon or nitrogen.

Lockett et al. studied several RTILs of the [rmim][Cl] family at a glassy carbon (GC) electrode using EIS and cyclic voltammetry (CV), where the imidazolium cation [rmim] (also [$c_n$mim]) can have alkyl chains of different lengths, *i.e.* 1-ethyl-3-methylimidazolium [emim] ([$c_2$mim]), 1-butyl-3-methylimidazolium [bmim] ([$c_4$mim]), and 1-hexyl-3-methylimidazolium [hmim] ([$c_6$mim]) [107]. The common chloride anion was exploited in forming an RE, namely Ag|AgCl|RmimCl. Lockett reported capacitance increase with decreasing cation size, as can be expected from the effective decrease in EDL thickness. Capacitance was also seen to increase with temperature. In this family of RTILs, the electrochemical window is set by oxidation of chloride and reduction of the imidazolium ring, and thus the alkyl chain length is not significant in this sense. The Nyquist plot of the complex capacitance with no polarization is a straight line, although there is deviation from vertical with different alkyl chain lengths; this may be an effect of adsorption. The

capacitance curve showed a camel shape as expected from Kornyshev's theory, and thus the PZC was expected to be at the minimum. This study was followed up later with a much larger number of RTILs (in addition to the above, [bmim] with different anions bromide [Br], iodide [I], [BF_4], [PF_6], and [Tf_2N]; and 1-butyl-1-methylpyrrolidinium [bmpyr][Tf_2N] ([$c_4$mpyr][Tf_2N])) at GC, Pt, and Au electrodes, which all showed several extremas around the PZC in camel shapes [108]. However, some of these findings were brought into question by results of Alam et al. using a combination of EIS and electrocapillarity measurements. The electrocapillary curve relates surface tension to cell potential and typically takes on a parabolic shape on which the maximum corresponds to the PZC. Study of 1-propyl-3-methylimidazolium [pmim][BF_4] ([$c_3$mim][BF_4]) at Hg drop, Au, and GC electrodes showed inconsistent PZC's between the electrocapillary curves and capacitance curves, and furthermore the curves were of parabolic shape as opposed to the camel shapes reported before [109]. Another study of [emim][Cl], [bmim][Cl], [hmim][Cl], and diethylmethyl(2-methoxyethyl)ammonium [deme][BF_4] at Hg showed parabolic capacitance curves with a hump, shown to be dependent on the alkyl chain, which decreased with temperature in contrast to the results of Lockett et al. [110], also supported by Vatamanu et al.'s simulation work [93]. Further studies, including additional RTILs 1-octyl-3-methylimidazolium [omim][BF_4] ([$c_8$mim][BF_4]) and [emim][Tf_2N], showed that apparent PZC at GC electrodes could be changed by electrochemical pretreatment of the surface, that the capacitance at PZC increases with temperature, and that long alkyl chains ([hmim] and [omim]) resulted in a broadening of the electrocapillary maximum as a consequence of the crystal structure and spatial heterogeneity [111, 112]. Mixing [omim][BF_4] into [emim][BF_4] resulted in the capacitance curve taking on qualities of the longer alkyl chain with increasing [omim] concentration, including surface tension, surface charge density, and differential capacitance decrease; and the electrocapillarity curve broadening at its maximum [113]. Islam et al. were able to observe all three capacitance curves predicted by Kornyshev, bell and camel shapes at Au and Pt, and the U-shape at GC in [deme][Tf_2N], trimethylpropylammonium [tmpa][Tf_2N], 1,3-diallylimidazolium [dalim][Tf_2N], and [bmpyr][Tf_2N] [114].

Further studies on carbon electrodes revealed differences between GC and highly oriented pyrolitic graphite (HOPG), in which [emim][BF_4], [deme][Tf_2N], and trioctylmethylammonium [toma][Tf_2N] showed symmetric U shapes at HOPG as opposed to the more complex asymmetric U shapes at GC [115]. This was attributed to the electronic density in the electrode and was explained with semiconductor theories. Other interesting findings from EIS studies include the observation of two arcs in the impedance spectra of Au(100)|[bmim][PF_6] explained by ion replacement in the innermost layer [116] and the discovery of capacitive processes at two distinct time scales at Au(111)|[bmpyr][FAP] (tris(pentafluoroethyl)trifluorophosphate anion), where the slow process on the order of 1 Hz is believed to be due to charge redistribution in the innermost layer and the fast process up to 1 MHz is almost constant near PZC and due to charge redistributions with smaller activation energies [117]. The temperature dependence of the two processes were studied by Druschler et al., who found that the slow process is Arrhenius activated and the fast process can be described by the Vogel-Fulcher-Tammann law [118]. A third ultraslow process was discovered with EIS, thought to be related to the formation of vacancies at the Au surface. Ultraslow relaxation was also observed at water|RTIL interfaces in trihexyltetradecylphosphonium bis(nonafluorobutanesulfonyl)imide [thtdp][Nf_2NH], [toma][Nf_2NH], and [thtdp][TB] (tetrakis(pentafluorophenyl)borate) [119, 120]. Recent developments in RTIL synthesis have led to a new class of dicationic ionic liquids, in which the cation has +2 charge; Costa et al. applied EIS, CV, and electrocapillarity techniques to the RTIL 1,5-bis(3-dimethylimidazolium)pentane di-bis(trifluoromethylsulfonyl)imide [$c_5(mim)_2$][Tf_2N]$_2$ and found a wider electrochemical window but qualitatively similar shaped capacitance curves sensitive to electrode material [121]. For a review on voltammetry results in RTILs and a comparison to classical electrolytes, refer to reference [122]; this includes a discussion of the applicability of Butler-Volmer versus Marcus theories on electron transfer kinetics with consideration of differences in EDL structure.

Recent studies have employed *in situ* techniques to probe EDL structure, often scanning tunnel microscopy (STM) and its successor atomic force microscopy (AFM) which can resolve features smaller than 1 nm. Surfaces and multilayered structure, es-

pecially in thin films, have also been analyzed with x-ray photoelectron spectroscopy (XPS) and x-ray reflectivity (XRR) techniques. Endres amongst others started using STM as a way of analyzing the ability to electrodeposit metals in RTILs [123]. Lin et al. applied similar techniques to the Au(111) surface, discovering a potential dependent long-range surface restructuring involving the formation of pits merging into long networks and finally recovering a smooth surface via electrochemical annealing [124]. Mezger et al. used XRR to study the layered structure of three [FAP] RTILs (cations [bmpyr], [hmim], and tetrabutylammonium [tba]) at sapphire ($Al_2O_3(0001)$), finding an exponentially decaying density profile due to effects of correlation [125]. Nishi et al. also applied XRR not at an electrode but at a free surface of [toma][Nf_2NH], confirming at least four ionic layers [126]. Cremer et al. studied the growth of ionic layers by RTIL thin film deposition and XPS, observing 3D growth at amorphous silicon glass substrates of [emim][Tf_2N] [127] and 2D growth in layer-by-layer checkerboard patterns of [dmim][Tf_2N] and [omim][Tf_2N] at Au(111) surfaces [128]. Bovio et al. observed that the analogous terraced island structures of [bmim][Tf_2N] during layer formation behave as solid-like, perhaps crystalline, structures with regular step heights and stiffness leading to fragility under AFM probing [129]. This formation pattern corresponded to MD findings reported in the same paper. Min et al. found an exponentially decaying force as a function of distance using AFM at [bmim][TfO] (trifluoromethanesulfonate), [bmim][BF_4], and [thtdp][Br] in between two slabs of atomically smooth mica surfaces [130], in agreement with the density profiles seen by Mezger et al. An effective λ_D was determined to be 1–4 nm, and oscillatory forces in addition to the exponential decay were observed when the slab separation was of similar magnitude to λ_D. These findings were recreated for more combinations of surfaces (HOPG, mica) and RTILs ([bmim][Tf_2N], [bmim][BF_4], [emim][$EtSO_4$] (ethylsulfate), [hmim][Tf_2N]), with an additional finding of low friction coefficient in shear suggesting applications as lubricant [17, 131, 132]. Hayes et al. described the effects of adsorbed cation vs. anion in the packing of ions in subsequent layers as probed with AFM [133], and Gnahm et al. observed these structural differences via *in situ* STM at potentials positive and negative of PZC and related them to features

seen in CV and EIS results [134]. Endres et al. studied the effect of adding solute to the Au(111)|[bmpyr][FAP] system, reporting that beyond $\approx 10\%$ by weight of LiCl, the repulsive forces typically seen by AFM become attractive near the surface [135]. Zhang et al. made a case for the necessity of distinguishing between charged ionic layers in the EDL and neutral but still layered structures in the uncharged bulk [136]. The herringbone superstructure as found in simulations was seen by Atkin et al. with STM and AFM at the Au(111) surface, explained as the reconstruction of the gold surface [137]. Corresponding EIS measurements revealed that the ultraslow process observed by Druschler et al. was indeed due to the formation of vacancies in the herringbone structure.

Study of RTILs at carbon electrodes has also been popular, especially with regards to its application in supercapacitors. Nanjundiah et al. sought to rationalize the observation of much lower capacitance in high surface area carbon cloths in practical capacitors relative to smooth electrodes [138]. Study of [emim] RTILs with anions [Cl], [BF_4], [TfO], [Tf_2N], and tris(trifluoromethylsulfonyl)methanide [Tf_3C] revealed that rate of charge/discharge and accessibility of electrolyte to the surface drive realizable capacitance in practical systems, as porous separators inherently limited parts of the electrode surface from contacting ions. Balducci et al. then applied [bmpyr][Tf_2N] to a supercapacitor cell and ran cycling tests with a max range of 4.5 V, observing high stability and high specific capacitance over 40000 cycles [9].

2.2 Electrospray Application

Electrospray is a field emission phenomenon releasing high velocity particles from a stressed liquid meniscus upon the application of very high potentials. In practical applications, sharpened emitters are provided to focus the electric field thus reducing the required potential and to ensure cone formation at a known location. Emitters of various geometries have been studied and can be organized roughly into three groups, illustrated in Fig. 2-4: externally-wetted, capillary-flow, and porous. A common design is to use a conducting emitter as an electrode paired with an extractor electrode

downstream. There are no general requirements for the extractor, although for use in propulsion there must be an aperture to allow the beam to escape.

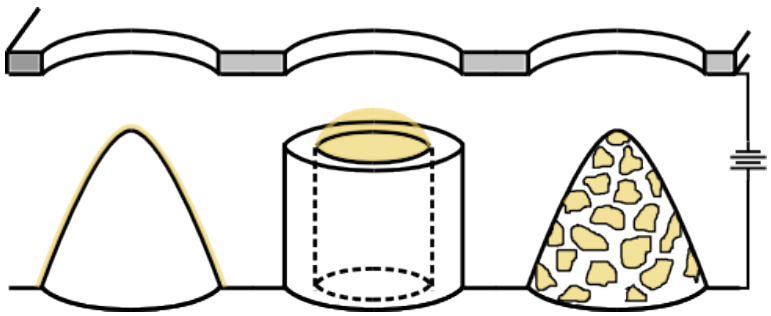

Figure 2-4: Different geometries of electrospray emitters. Left: externally wetted emitter. Center: capillary emitter. Right: porous emitter.

Characterization of externally-wetted tungsten emitters with time-of-flight (TOF) spectrometry indicated that [emim][BF_4] emitted both cations [$emim^+$] and singly solvated cations [emim][BF_4][$emim^+$] at positive polarity and analogous anions at negative polarity [139]. Ion beam emission with species of different charge-to-mass ratios result in an inefficiency mode known as polydispersity, in which particles are accelerated to different velocities and their relative velocity acts analogously to drag. This effect can be compounded by fragmentation, in which solvated ions break apart in the acceleration region, increasing velocity dispersion [140, 141]. Externally-wetted emitters are quite practical for applications such as focused ion beam for microfabrication [12], but when large arrays of emitters are desired for increased emission such as in propulsion, problems arise in propellant (electrolyte) replenishment. One solution is to use a porous material with high enough hydraulic conductivity to keep up with emission. Porous nickel was demonstrated as a capable substrate, with similar emission characteristics to previous tungsten emitters and with the ability for array fabrication via electrochemical etching [1].

The use of a metal emitter as electrode simplifies design by combining the requirements of liquid transport, field enhancement, and potential application; however, electrochemical effects were found to degrade the emitters over time. As ions of one polarity are emitted, the resulting charge imbalance leads to potential buildup between the electrode surface and electrolyte bulk. This manifests as an increase in

the double layer potential, or the total potential drop across the non-neutral sheath structure. Once this potential breaches the electrochemical window, reduction or oxidation reactions occur as governed by Faraday's law

$$\dot{m} = \frac{IM}{zF} \tag{2.6}$$

where I is current (constant in this formulation), M is molar mass of the reaction product, and $\dot{m}$ is the mass rate of product liberated. The products of RTIL electrochemical decomposition are not well known, although a preliminary study on candidate fragments was conducted with a residual gas analyzer [2]. The results are reproduced in Appendix D. Aside from the emitter degradation, buildup of these product concentrations will change RTIL properties, and if emitted may also contribute to polydispersity. Local pressure increase due to gaseous byproducts may cause arcing, through which if enough current flows could be catastrophic.

Two possible solutions have been proposed, which may be utilized separately or concurrently. From an operation perspective, alternating the voltage at a frequency faster than the EDL charging time can restrict electrochemical degradation [23]. By measuring the current onset delay at each polarity reversal, a maximum frequency of $\approx 75\,\mathrm{Hz}$ was determined [142]; the minimum frequency can be deduced from studying the potential evolution for specific systems under controlled currents, but analytical calculation requires more accurate double layer models. Earlier electrospray studies [1] interpreted the decay of voltage evolution from a linear regime as the onset of Faradaic reactions. However, this assumes an idealized constant capacitance, which is now known to be a poor model for RTIL EDLs. To better understand the nonlinear growth in double layer potential, a capacitance curve that accurately represents the system in use must be employed.

From a design perspective, another solution is to apply potential through a separate electrode so that degradation does not occur at the emitter. An earlier test attempting to fabricate emitters from dielectric materials employed such a design [143], and later a "distal" electrode in the RTIL reservoir was used specifically to demon-

strate mitigation of electrochemical degradation [144]. Although not a solution by itself, another useful modification is to delay the double layer charging. Charging dynamics are a function of both electrode and electrolyte, and use of RTILs with wide electrochemical windows is already favorable. The electrode can also be improved with careful selection of properties, with high surface area being a primary consideration as seen in supercapacitors. Increased surface area allows for wider distribution of surface charge, effectively slowing potential increase. Xerogels are highly porous solids with extremely high specific surface areas, and may be synthesized using a variety of chemical recipes. One such xerogel, resorcinol formaldehyde (RF), has been formed into electrodes for use with RTILs, with internal surface area as high as $500\,\mathrm{m}^2/\mathrm{g}$ [145]. RF can be pyrolized at temperatures above $800\,^\circ\mathrm{C}$, and can be further activated with exposure to CO_2 to form hierarchical micro- and nano-scale pores [146]. Micropores are large enough that the EDL can be assumed thin; however, when nanopores are involved their behavior may change drastically due to the EDL completely filling the pore and interacting with each other. This can change the capacitive behavior in more complex ways than simple scaling by area [147]. As all three methods are mutually compatible, the path forward seems to be to use a high surface area distal electrode with voltage alternation.

Chapter 3

Experimental Methods

Modeling double layer charging in RTILs, as outlined in Chapters 1 and 2, is made difficult by the unique solvent-less nature of the liquids and the sheer number of possible ion combinations. In this thesis, a series of experiments starting from the very fundamental and increasing in complexity to a fully developed system for actual operation in orbit is conducted to study the charging behavior with two RTILs. Using a common experimental setup, differential capacitance curves at flat platinum surfaces are obtained by impedance spectroscopy. The RTILs are then tested at carbon electrodes to compare the impedance behaviors at flat and porous electrodes. This is the same carbon electrode used in various electrospray systems developed at MIT's Space Propulsion Laboratory. Double layer charging is studied in two such systems, one a single emitter operating in the 100 nA range and the other an array of emitters totaling in the 100 µA range. This chapter presents the experimental methods used in these various tests, and their results will be presented in subsequent chapters.

Two RTILs were used for experimentation, 1-ethyl-3-methylimidazolium tetrafluoroborate [emim][BF_4] and 1-ethyl-3-methylimidazolium bis(trifluoromethylsulfonyl)imide [emim][Tf_2N]. The RTILs were purchased from Iolitec Inc. at >98% purity or better. However, [emim][BF_4] and to a lesser degree [emim][Tf_2N] are hydrophilic, absorbing ambient moisture within minutes if left open. Even trace amounts of water are expected to affect double layer measurements [148]; due to the high polarizability of water, water molecules will likely migrate to within the double layer where the high-

est electric field exists. In order to control this, the RTIL was stored in a nitrogen-purged dry box and further dried under vacuum for > 10 h prior to each experiment. Experiment-specific handling of the RTILs are discussed in their respective sections below.

3.1 Parallel Plates

As discussed in the electrospray application portion of the literature review, a better model of the RTIL capacitance curve is necessary in order to understand double layer potential evolution. In fact, the capacitance curve is a common tool by which double layer theories are compared to experimental data in order to verify the models' validity. To get accurate capacitance data, the experimental setup must be simplified so that only the properties of the interface of interest (at the working electrode) are captured. Complex geometries, including electrode surface roughness, can add extraneous effects into the data, thereby making them more difficult to interpret. In this section, a simple parallel-plate capacitor-like electrochemical cell is used in order to produce reliable data. All experiments were conducted three or more times to test repeatability.

Electrochemical impedance spectroscopy (EIS) is the common method found in literature for probing RTIL double layer capacitance. The method is well established in classical solvents and is considered accurate. The technique is typically conducted with a three electrode system, in which the working electrode is held at some constant bias potential with respect to the reference. A small AC sinusoidal voltage perturbation is applied about the constant DC bias, and the resulting current magnitude and phase shift are analyzed. Although current theoretical models for predicting double layer capacitance are incomplete, many of the key features seen in actual experimental data have been qualitatively described. A larger body of available capacitance data will help verify new models as they become available. Continuing the work of Bazant, et al. [50] and Han, et al. [74], a continuum model that incorporates both electrostatic correlations and ion size asymmetry may in the future be able to better

predict real RTIL behavior.

EIS, while a well understood and reliable method, can be slow. The method, described in detail below, requires AC perturbations to be performed over a wide range of frequencies at a number of DC offset potentials. Given that millions of RTILs can be made by selection of different cations and anions, it may be desirable to more quickly generate accurate capacitance curves for new RTILs. Using the same electrochemical cell, three methods previously unused for probing double layer capacitance were compared to the impedance method in order to gauge their potential for helping to speed up the characterization of different RTILs. These tests produced capacitance curves that were several orders of magnitude off from the impedance results, and were determined not to be accurate tests for this purpose. These results are presented in Appendix B.

3.1.1 Parallel Plate Electrochemical Cell

Design of an electrochemical cell for use with RTILs requires several considerations. Many RTILs are expensive or difficult to synthesize, and thus the cell must be able to obtain measurements with small amounts of electrolyte. Also, as will be discussed later, many RTILs are hydrophilic and in order to control for contamination, the cell must be able to be operated under vacuum. With these limitations, the cell was designed as shown in Fig. 3-1.

The working and counter electrodes, WE and CE respectively, are made identically, machined from 316 stainless steel ANSI 10-34 bolts. This material was selected for its resistance to corrosion and degradation as well as its machineability, which was necessary for producing a flat working area of precise surface area. The working end is turned down on a lathe to a diameter of 1.5 mm and faced. The face is then treated progressively with 500, 1500, and 2500 grit sandpaper, with a sonic bath cleansing in between each step. The face is further polished with a 0.1 µm Buehler polishing pad and finished with a 20 nm fused silica suspension to give a mirror-like surface. The bolts are cleaned in the sonic bath in acetone then isopropanol. In order to coat the working surface with platinum, the bolts are fitted in a PEEK casing which exposes

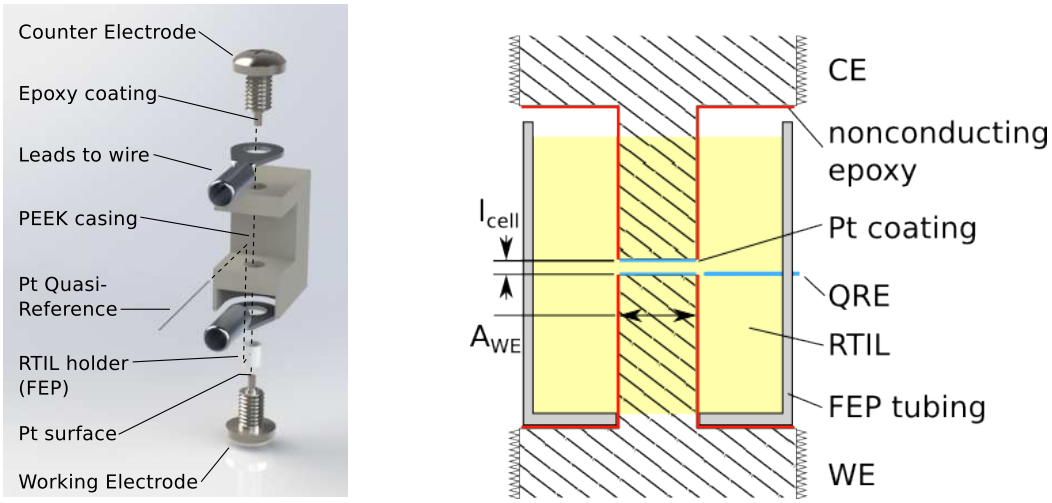

Figure 3-1: Left: Exploded view of electrochemical cell for use in vacuum. Right: Cartoon diagram of working area of cell. Platinum surface areas on working and counter electrodes are isolated by epoxy. Platinum wire serves as quasi-reference.

only the polished surface. Using the AJA International ATC-1800 sputter deposition system at the MIT Microsystems Technology Laboratories (MTL) Exploratory Materials Laboratory (EML), the surface is backsputtered then coated with a 15 nm titanium adhesion layer and 50 nm of platinum. Platinum makes for a good electrode surface as it does not readily react, and has been used often in RTIL studies [108,122]. However, this also means the platinum coating does not bond well to the steel and thus the titanium layer is necessary to maintain a more robust bond; this adhesion layer is often used for platinum sputtering as well as electroplating. Finally, the side surface of the turned down section is coated with a thin layer of non-conducting 10-3784RGR15 epoxy from Epoxies, Etc. to isolate the electrode working area.

The cell casing is machined from PEEK. The hard plastic is often used for vacuum applications due to its good outgassing properties and chemical resistivity. The WE and CE are screwed in from either side, so the electrode separation distance is easily modified by turning either bolt. In practice, the WE was kept fixed and the distance adjusted with the CE. In order to keep the RTIL in place and in electrical contact with the electrodes, a FEP tube with outer diameter of $^5/_{32}$ in. and inner diameter of $^3/_{32}$ in., purchased from Omega Engineering, Inc. is attached to the end of the WE and held in place with non-conducting epoxy. A small hole is punctured in the

FEP tubing near the plane of the WE surface to accommodate a 0.01 in. 99.99% pure platinum wire which serves as the quasi-reference electrode (QRE). The QRE is placed as close to the WE as possible to reduce electrolyte resistance and sealed in place with epoxy to prevent leakage.

3.1.2 RTIL Handling for Parallel Plate Cell

Immediately preceding each experiment, the RTIL is introduced into the electrochemical cell and held under vacuum for 10 or more hours to evaporate residual water. During this process, a voltage $> 1.23\,\mathrm{V}$ is applied for 30 minutes so that water electrolysis may further reduce water content. Particular care is necessary at the beginning of the pump-down process, as water vapor can coalesce into large bubbles whose bursting can displace significant quantities of RTIL from the working area, or if trapped in the cell, can limit the surface area of RTIL in contact with the electrodes. Furthermore, the use of multiple RTILs in the same cell requires careful cleansing in between each test. In order to help this process, the following procedure is followed:

1. Pre-dry RTIL under vacuum
2. Remove CE bolt from electrochemical cell
3. Soak all components in acetone and clean in ultrasonic bath for 1 h
4. While still wet, transfer to beaker with isopropanol and clean in ultrasonic bath for 0.5 h
5. Once dry, introduce $\approx 5\,\mu\mathrm{L}$ of RTIL into FEP tube
6. Screw CE bolt in partially, so that electrode surface is outside of FEP tube
7. Place cell in vacuum chamber and connect all electrical leads (WE, CE, and QRE)
8. Slowly evacuate chamber pressure
9. Once bubbling calms down or stops, vent chamber

10. Quickly screw in CE to desired separation distance

11. Slowly evacuate chamber pressure

12. Upon full pump down, apply 1.235 V across cell for 30 min to electrolyze residual water

13. Wait 10 h for further drying

14. Conduct electrochemical tests

15. After test, vent chamber and remove cell. Confirm electrode separation distance under microscope

Introduction of the RTIL is done with a syringe fitted with a luer to $^1/_{16}$ in. tubing adapter. Due to the ionic liquid's viscosity, it is necessary to add the liquid slowly so that the liquid could fill all of the surrounding space between the FEP tubing and the electrode without leaving air pockets underneath. During pump-down, bubbles that form near the bottom would often coalesce into large bubbles and get trapped in the space between the electrodes. This would change the amount of interfacial surface area available for the test and must be avoided. Sometimes this bubble would eventually escape on its own; other times, it was necessary to vent the chamber, remove the CE partially so that the tip was outside the FEP, and pump down again to allow further drying. The chamber could then be vented and the CE inserted fully before pumping down again. This procedure is repeated as often as necessary to avoid bubbles in between the electrode surfaces.

3.1.3 Electrochemical Impedance Spectroscopy

Electrochemical impedance spectroscopy was conducted with a Gamry Reference 3000 potentiostat. As noted in literature [107], impedance measurements must be taken in one direction at a time from open circuit potential (OCV), with enough time in between the two scans to allow for relaxation. Capacitance curves generated with

data starting from any potential other than OCV were shown to give different results every time without any repeatability.

In order to estimate the characteristic time scale for charging and relaxation, a first-order approximation of the RC time can be calculated. Electrical conductivity σ values have been reported in literature for a number of RTILs [18], and its inverse gives the electrical resistivity. Then, the simple relation

$$R_{bulk} = \frac{l_{cell}}{\sigma_{RTIL} A_{WE}} \tag{3.1}$$

where the cross-sectional area was selected to be the WE area A_{WE}, gives the bulk resistance of the cell. The interfacial capacitance can be calculated to a first-order approximation using Eq. 1.3, using the cation or anion diameter for the ion size δ. With many RTILs, the ions are not spherical and so an effective diameter must be calculated. For the 1-ethyl-3-methylimidazolium cation and tetrafluoroborate anion, molecular dimensions were found in literature as calculated from density functional theory methods [149]. For the bis(trifluoromethylsulfonyl)imide anion the dimensions could not be found; instead, the ion volume V_{ion} was determined from crystal structures using a reference pair ion of known volume [150] and the diameter a_{ion} calculated as though the volume were a sphere. The three dimensions found for [emim] and [BF_4] were averaged to give an effective diameter, as the orientation of the ions adsorbed on the electrode surface is not known. By comparing the two methods using three ions for which both numbers could be found ($[emim]^+$, $[bmim]^+$, and $[BF_4]^-$), it was seen that the second method gives an effective diameter larger by 18-67%. An alternate size scale was proposed by Zhao [101] which depends on correlation length $l_c \approx a_{ion}$ and Debye length λ_D, $\delta_{zhao} = \sqrt{\lambda_D l_c}$. The Debye length can be calculated by an alternate form of Eq. 1.9,

$$\lambda_D = \sqrt{\frac{\epsilon k_B T}{2 N_A e^2 I}} \tag{3.2}$$

where N_A is the Avogadro constant and I is ionic strength in $\mathrm{mol\,m^{-3}}$ and can be

Table 3.1: First-order size scales and key physical parameters for RTILs.

RTIL	ϵ_r	I[mol m^{-3}]	a_{cat}[Å]	a_{an}[Å]	λ_D[Å]	$\delta_{zhao,cat}$[Å]	$\delta_{zhao,an}$[Å]
[emim][BF_4]	12.9	6465.6	5.305	3.100	0.485	1.604	1.226
[emim][Tf_2N]	12.3	3884.4	5.305	7.600	0.611	1.800	2.154

calculated as $I = 1000\frac{\rho_m}{M}$ from mass density ρ_m in kg m^{-3} and molar mass M in g mol^{-1}. The static relative permittivity values were found for $T = 298.15$ K [151]. The calculated length scales are summarized in Table 3.1.

Using the conductivity values 1.3 S m^{-1} for [emim][BF_4] and 0.86 S m^{-1} for [emim][Tf_2N], and $l_{cell} = 75 * 10^{-6}$m as the electrode separation distance, Eq. 3.1 gives bulk resistances of 32.65 Ω and 49.35 Ω, respectively. Using the effective ion diameters, a capacitance-per-area of 21.53 µF cm^{-2} and 36.84 µF cm^{-2} were calculated for [emim][BF_4] for cation and anion, respectively. For [emim][Tf_2N], the values were 20.53 µF cm^{-2} and 14.33 µF cm^{-2}. Due to the small values for Debye length, the Zhao length scale is smaller than the ion size, thereby predicting larger values of capacitance (in excess of 50 µF cm^{-2} for all four ions presented). However, in light of the multilayered double layer structure now known to be prevalent in RTILs, the actual capacitance is expected to be lower than those calculated above and the Zhao scale is not expected to be accurate for purposes of calculating capacitance. Taking the largest values of resistance and capacitance calculated, the first-order RC time scale is calculated as approximately 20 µs.

In practice, a much slower time scale was observed. For example, after the electrolysis potential was applied during the RTIL drying phase, the open circuit potential decayed over a time scale on the order of 1 h. To account for this, the cell is left at open circuit for 1 h in between the positive and negative scans, as well as before subsequent repeat runs.

A "positive scan" refers to the scanning of the DC bias from OCV to 1.2 V, which was taken in 0.05 V increments. The "negative scan" scans from the same OCV to −1.2 V in 0.05 V increments. These limits were selected by first running a voltammetry scan, as shown in Fig. 3-2. Although the electrochemical window of the RTILs are expected to be at much larger potentials as indicated in Table 4.1, the

voltammetry shows significant increase in current at potentials slightly larger than the limits, indicating perhaps Faradaic reactions of impurities such as water.

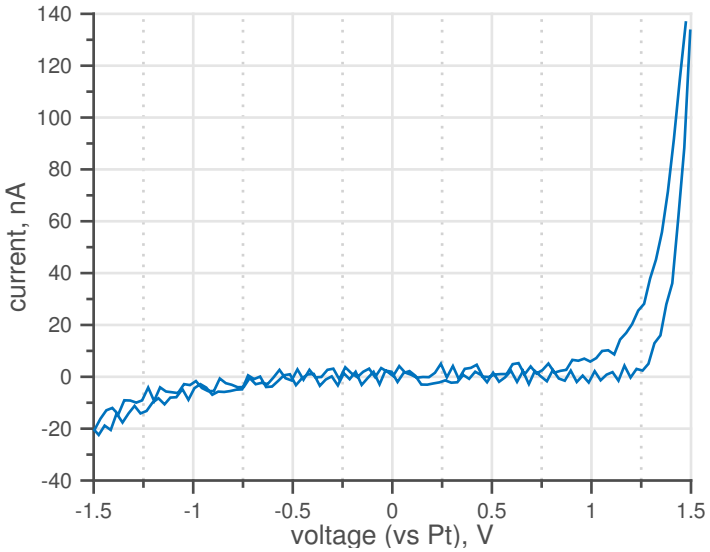

Figure 3-2: Initial voltammetry scan for determining test potential limits measured with respect to a platinum QRE. Limits were selected for following experiments as $-1.2\,\mathrm{V}$ to $1.2\,\mathrm{V}$.

The EIS method calls for an AC excitation to be applied about some DC bias potential. In practice, the steps are as follows:

1. Apply constant DC bias potential at WE with respect to QRE
2. Apply AC sinusoidal excitation potential about the DC bias
3. Record current response
4. Use current magnitude and phase shift (lag of sinusoidal pattern compared to applied potential) to populate Bode plot

At each DC bias potential, an AC excitation of amplitude $5\,\mathrm{mV}$ is applied. EIS requires a large number of frequencies to be tested so that impedance may be expressed on a Bode plot (impedance magnitude and phase plotted against frequency) or a Nyquist plot (imaginary impedance plotted against real impedance with each data point corresponding to a single frequency). For these tests, the frequency is scanned from $1\,\mathrm{MHz}$ to $0.1\,\mathrm{Hz}$ at 7 points per decade.

3.2 Porous Electrodes

Porous electrodes are attractive for a variety of applications including electrospray propulsion. The primary reason for this is the very high interfacial surface area, due to the electrolyte filling the pores. Stable monolithic structures made of porous solids such as aerogels and xerogels can have specific surface areas on the order of $100\,\mathrm{m^2\,g^{-1}}$ or greater. This area allows for greater distribution of surface charges, thereby increasing total capacitance and delaying the onset of Faradaic reactions. This has led to activated carbon electrodes being a popular material of choice for supercapacitors, organic synthesis, and electrosprays.

Despite these advantages, there are inherent complexities in dealing with porous materials. Unlike flat surfaces, the double layer cannot form instantaneously at all surfaces within the porous structure. Instead, the double layer must diffuse into the pores over a characteristic time $\tau_D \sim R'C'$ where R' and C' are resistance-per-length and capacitance-per-length, respectively. In order to interpret the behavior of electrochemistry at these porous electrodes, this double layer diffusion must be accounted for properly. In a practical sense, this means that there is some cutoff frequency which separates slow and fast electrochemical behaviors. Fast frequencies will be dominated by ion diffusion through the porous medium, and slow frequencies will reflect local interfacial effects. In order to properly understand porous electrode behavior, both components must be incorporated into the electrochemical model.

The porous electrode cell presented in this section is used for two experiments. The more fundamental study uses the same EIS method described in section 3.1.3, with scans at $0.05\,\mathrm{V}$ increments between the limiting potentials of $1.5\,\mathrm{V}$ and $-1.4\,\mathrm{V}$. The second study, chronopotentiometry, tests the electrode charging behavior under a constant current step in an experimental setup simpler than those used in electrospray systems.

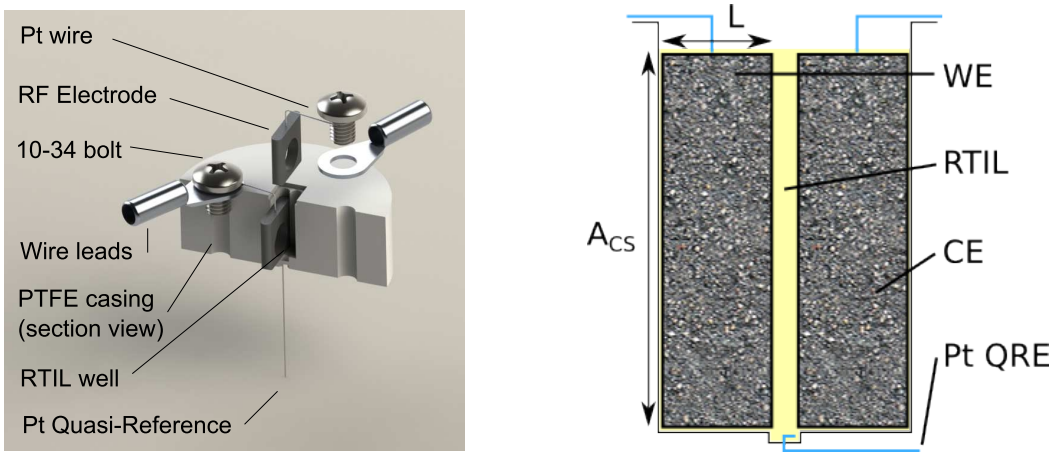

Figure 3-3: Left: Exploded section view of porous electrode electrochemical cell. Right: Cartoon diagram of working area of cell. Two carbonized RF electrodes serve as WE and CE; a Pt wire acts as quasi-reference.

Table 3.2: Resorcinol Formaldehyde ingredients. These quantities make 40 S-iEPS thruster electrodes, and can be adjusted linearly as necessary.

material	quantity (g)
Resorcinol	19.68
deionized water	24.00
Formaldehyde solution (37% wt.)	28.64
acetic acid	0.704

3.2.1 Porous Electrode Electrochemical Cell

A different electrochemical cell was designed for use with porous carbon electrodes. This cell was subject to the same considerations as in the parallel plates setup, namely use in vacuum and a focus on minimizing the necessary amount of RTIL. The final design of the cell is shown in Fig. 3-3.

The carbon electrode was designed for use with the Scalable ion Electrospray Propulsion System (S-iEPS), developed under the Game Changing Development Program of NASA's Space Technology Mission Directorate and delivered to NASA in July 2015. A resorcinol formaldehyde (RF) xerogel is synthesized using the materials and quantities shown in Table 3.2 sourced from Sigma-Aldrich, following Arestie's recipe [145]. The water, resorcinol, and formaldehyde solutions are mixed until all resorcinol particles have dissolved, then the acetic acid is mixed in as catalyst. The solution is poured into a mold and subsequently covered with a lid which holds a

platinum wire to be embedded into the xerogel. The mold is sealed in an air-tight container and dried over several days at progressively higher temperatures:

1. 24 h at room temperature
2. 24 h at 40 °C
3. 24 h at 60 °C
4. 72 h at 80 °C

The mold is then allowed to cool to room temperature and removed from the sealed container. The xerogel at this point is a brown solid with the platinum wire firmly embedded within, and the lid can also be removed. The xerogel is soaked with acetone, which helps to relieve internal stresses. After 24 h, the mold is again placed in the oven without the lid at 80 °C for 48 h of further drying.

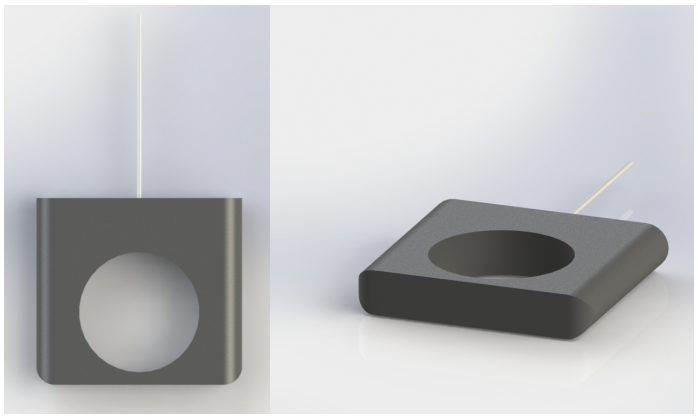

Figure 3-4: RF electrode design for S-iEPS. Overall dimensions are 10.16 x 11.20 x 2.11mm with rounded edges.

The RF xerogel is a porous monolithic structure and is not electrically conductive. In order to use this as an electrode, it is pyrolized at 900 °C for 3 h under running Argon. This completely carbonizes the RF, making it highly electrically conductive. The electrode is then ground to the specified shape, shown in Fig. 3-4, with sandpaper. The dimensions are 10.16 mm x 11.20 mm x 2.11 mm with the bottom corners rounded. These dimensions were based on the designed tank size, shown in Fig. 3-8. The tank has a port to allow RTIL transport from the reservoir to the thruster passively, using

capillary action through a series of porous materials. A hole is drilled through the carbonized electrode to mate to the tank port and allow higher hydraulic conductivity. After sanding, the electrode is cleansed in acetone for 1 h using the ultrasonic bath, clearing the porous matrix of the material that was sanded off.

The cell itself is machined from Teflon PTFE. PTFE has favorable qualities, including chemical resistivity and good outgassing properties for use under vacuum conditions. A small hole is placed in the bottom to allow insertion of the platinum wire QRE, the same as used in the parallel plate experiments. After the two carbon electrodes (WE and CE) are inserted into the cell, the wires are clamped to two metallic bolts which act as connection points for external potentiostats.

3.2.2 RTIL Handling for Porous Electrode Cell

The same RTILs as in the parallel plate experiments are used in the porous electrode tests, [emim][BF_4] and [emim][Tf_2N]. The RTILs are again held under vacuum for 10 h or longer before each experiment. This is more difficult than in the parallel plates cell, due to two factors. First, due to the size of the electrodes as set by the S-iEPS design, the cell is much larger and thus more RTIL is required. Second, due to the high porosity of the carbon electrode, trapped air and water vapor bubbles tend to coalesce and result in large bursting events. Care must be taken to pre-dry the RTIL as much as possible under vacuum before introduction into the cell, and the vacuum chamber pressure should be decreased very gradually so as to avoid more violent bubbling events. More specifically, the cell is prepared for each test using the following procedure:

1. Pre-dry RTIL under vacuum
2. Clean electrochemical cell
    - Soak all components in acetone
    - Ultrasonic bath for 1 h
    - While still wet, soak in isopropanol

- Ultrasonic bath for 0.5 h

3. Wipe inside surfaces of vacuum chamber with acetone

4. Insert small amount of RTIL into cell to coat bottom surface including QRE

5. Insert WE and CE, clamping their platinum leads to the connection bolts

6. Fill cell with RTIL until electrodes are completely saturated and all surrounding spaces are filled

7. Connect and test all electrical connections - WE, CE, and QRE

8. Slowly evacuate chamber pressure

9. Once fully pumped down, apply 1.235 V across WE and CE to electrolyze residual water

10. Wait 10 h for further drying

The chamber pressure evacuation step requires care, as large bubbles may not only displace significant amounts of RTIL from the working area, but also create undesired electrical shorts between the working area and other metallic components. Bubble formation and their bursting were recognized to be unavoidable; however, it was also observed that the RTIL volume increases noticeably under vacuum and thus some spilling is allowable as long as it does not create a liquid bridge between the working area and other components, namely exposed portions of the connection bolts. The spillage from small bubbles will often coat regions of the cell very close to the working area, and in most cases surface tension will actually pull the spilled liquid back into the working area. In the case of larger bubbles, the chamber is vented and the spilled liquid wiped off with lab wipes wetted with acetone. If it is deemed that too much RTIL has spilled, small amounts can be added until the liquid meniscus reaches the top of the electrodes, and the chamber is then reevacuated.

3.2.3 Chronopotentiometry

Chronopotentiometry (CP) is a technique in which potential variation is measured over time under constant current conditions. In this three electrode setup, the constant current passes through the WE and CE, while the potential is measured across the WE and QRE. This technique is often used in conjunction with the Nernst equation

$$\Phi_{red} = \Phi^{\Theta}_{red} + \frac{RT}{zF} \ln \frac{a_O}{a_R} \tag{3.3}$$

to track the redox reaction potential Φ_{red} and thus the surface concentrations of reaction species [28]. Φ^{Θ}_{red} is the standard half-cell reduction potential, and a_O and a_R are the chemical activities of the oxidizing and reducing species, related to concentration by $a_i = \gamma_i c_i$ where γ_i is the activity coefficient. However in this case, the measured potential tracks the evolution of the double layer potential as the potential is not allowed to grow past the electrochemical window. The potential is not the exact value of the double layer potential, but is rather offset by a resistive loss through the bulk electrolyte of finite conductivity and also by a double layer potential at the probe. These offsets however can be considered constant. The bulk resistance is a constant value and as the current is constant by nature of the experiment, the IR potential drop is constant. Also the probe double layer is assumed to remain constant, as it is only connected to the WE across a large impedance (the Gamry Reference 3000 electrometer has a $> 100\,\mathrm{T}\Omega$ input impedance) and is effectively floating with the liquid potential. If no current passes into or out of the double layer, then the double layer charge remains constant as does its potential. As such, the only variable component of potential is the double layer at the WE, and all variation in potential is attributed to changes in the amount of charge contained at the WE double layer.

Chronopotentiometry tests were conducted with a Gamry Reference 3000 potentiostat. Three values of constant current were tested, 50, 100, and 150 µA. These numbers were selected to be of similar magnitude to expected operating conditions of the NASA thruster, for which the carbon electrode of Fig. 3-4 was designed. After the electrode and RTIL are prepared as described above, the cell and potentiostat are

allowed to relax at open circuit. A two step current profile is then applied, at one of the three values above for 1800 s and then a negative current at the same magnitude for 1800 s. In order to prevent electrochemical reactions, thresholds were set at -1.4 V and 1.5 V so that the current would be cut off if the probe voltage surpassed those values. The cell is allowed to rest for > 1 h at open circuit before any subsequent tests at different current levels.

3.3 Externally-Wetted Solid Emitter

The single-needle externally-wetted emitter is a relatively simple implementation of RTIL electrospray. A solid needle and a distal electrode are connected via an RTIL liquid bridge. The distal electrode can be of various materials and shapes - in order to facilitate liquid retention and to suppress geometric effects by enforcing rotational symmetry, a ring geometry is used here. A potential is applied between the distal electrode and a downstream extractor electrode, which provides the electric field necessary to induce the formation of a Taylor cone-like structure and subsequent ion or droplet emission. In order to support this liquid meniscus, the needle tip must be of sufficient sharpness (tip radius on the order of 5 µm) and straightness. Furthermore, the needle surface must be conducive to RTIL transport from the reservoir in the ring distal electrode to the tip; this condition is typically met by roughening the surface. Fig. 3-5 shows a cartoon diagram of typical components that make up a needle emitter.

As the applied voltage is increased, the electric traction acting on the RTIL surface increases. When this force exceeds the restorative force due to surface tension, the surface deforms to form a sharp tip, which further enhances the electric field. When this exceeds the startup voltage, ion emission occurs by field evaporation. As ions of one polarity are emitted, ions of the opposite charge are left in excess in the bulk. In order for the liquid bulk to retain quasineutrality, the excess countercharge builds up at interfaces in the double layer. By studying the double layer charging current and potential evolution, the capacitance of this system can be obtained, for comparison

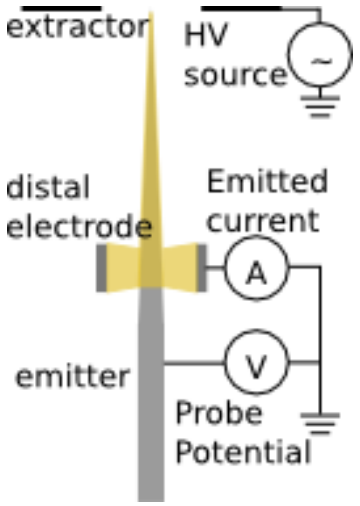

Figure 3-5: Main components for a solid needle electrospray emitter experiment. In this configuration, the needle is floating at a potential close to the RTIL potential. The electric field created between the liquid and the extractor plate causes field emission of cations or anions, depending on the polarity of potential applied.

with fundamental theories governing simpler geometries.

3.3.1 Experimental Setup

A needle was electrochemically etched from a 0.5 mm diameter tungsten wire. The wire was first cut to length and cleaned with water, acetone, and isopropanol. A beaker was prepared with 1M NaOH and a large metal cylinder electrode. The wire was attached to a vertical stage and suspended above the cylinder. A power supply was connected to the wire and the cylinder, and 7 mm of the wire was submerged into the NaOH. A voltage of 5 V AC was applied for 10 s to activate the surface. Afterwards, the wire was raised 4 mm and applied with 25 V DC to cut the wire. This process etches the wire in a way to create a tip of sufficient sharpness. The needle was then smoothed by applying 5 V DC for 2–4 min. After cleaning in water, the needle surface is chemically treated to provide adequate roughness for sufficient adhesion with the RTIL. Specifically, 25 mL of 1M NaOH is mixed with 9 g of potassium hexacyanoferrate(III) at 90 °C with a magnetic stirrer and the needle tip is submerged for 30 s. The needle is given a final cleansing with water, acetone, and isopropanol.

From previous experience, it has been observed that the current level available

from a particular needle is heavily influenced by its surface and tip sharpness. The most noticeable effect is the startup voltage. Larger tip radii tend to require higher applied potentials before current emission onset. In order to control for this, the same needle was used for all tests except one, with the same cleaning process involving acetone and isopropanol in the ultrasonic bath in between every cycling of the vacuum chamber. Before the final test, the needle tip is believed to have been damaged when the needle holder was knocked over during disassembly for cleaning. Stable emission could not be achieved in subsequent tests, including for configurations which had been tested previously. The final test was then conducted with a backup needle created with the same process at the same time, and verified to have similar startup voltages as the primary needle.

The needle is held in place by a PEEK holder. This holder has four holes sized and spaced for compatibility with eV Parts from Kimball Physics. The distal electrode is held by a separate PEEK holder, and separated from the needle holder by several spacers. Small spacers are stacked so that their positions can be rearranged to adjust the distance between the needle tip and distal electrode, without changing the distance between the needle tip and extractor. The extractor is a stainless steel plate with a 0.062 in. hole aligned with the needle. A steel lead wire is spot welded onto the extractor and the needle is fitted with a socket to allow for electrical connections. A solid model of the setup is shown in Fig. 3-6.

Two distal electrodes and respective PEEK holders are used for these tests. The first is a simple stainless steel cylinder, 0.125 in. in length and 0.071 in. in inner diameter. A steel wire is spot welded to the cylinder to provide an electrical connection. The second is a piece of carbon xerogel, with an embedded platinum wire for connectivity. Carbon xerogels tend to form a thin layer of skin upon synthesis, which has little to no porosity. For this reason, the electrode was polished to remove the skin in order to allow for the RTIL to saturate the porous structure. A hole 0.071 in. in diameter is drilled into the center of the 0.2x0.2x0.125 in. carbon monolith to mimic the internal face geometry of the stainless steel electrode. The second configuration is shown in Fig. 3-7. The xerogel was made in the same process as the electrode used

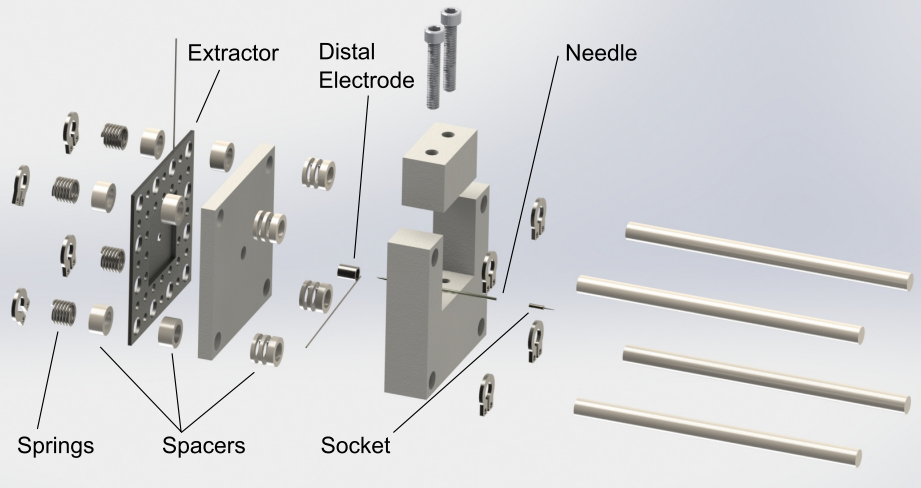

Figure 3-6: Exploded view of the solid needle emitter experimental setup. The distal electrode in this configuration is a stainless steel cylinder connected with a steel wire.

in section 3.2, so the same porosity (calculated in Ch. 4) was assumed.

The single-needle emitter is placed in a vacuum chamber for firing and testing. An in-house power supply is used to apply voltages up to 2 kV and also to read current. A Keithley 6517 electrometer is used to measure the potential between the distal electrode and needle, which corresponds to the variable double layer potential at the distal electrode surface offset by a constant double layer potential at the needle surface and some bulk liquid resistive loss. The electrical layout of the experiment is the same as shown in the cartoon of Fig. 3-5.

3.3.2 Experimental Methods

Before testing, the RTIL is pre-dried under rough vacuum for several hours. The dried RTIL is then introduced via pipette into the distal electrode, so that the menisci are just protruding from the ends and the entire inside surface of the ring is in contact with the liquid. With the porous distal electrode, care is taken to ensure full saturation. Over several cycles, enough RTIL is deposited on top of the electrode to make a significant meniscus and the electrode and associated PEEK holder are placed under vacuum to allow all gases to escape from the porous matrix while pulling in RTIL from the top via capillary action and gravity. This is repeated until the liquid meniscus is

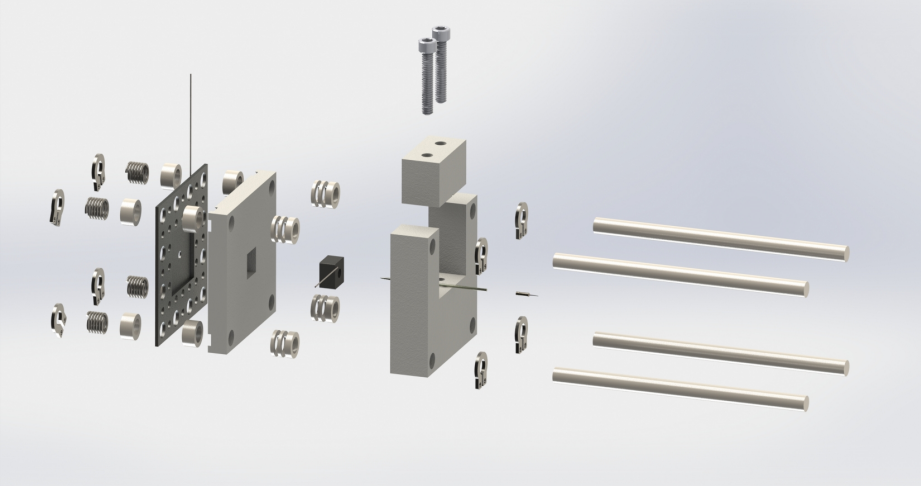

Figure 3-7: Alternate configuration of the solid needle emitter experimental setup. The distal electrode is a porous carbon monolith with a circular hole cutout of the same dimensions as the internal surface of the stainless steel cylinder electrode.

no longer pulled into the electrode, and excess liquid is removed by pipette. The setup is then assembled so that as the needle passes through the ring, it is wetted from the tip to the final position of the distal electrode. The extractor is placed so that it is about 0.5 mm from the needle tip. The extractor should be electrically isolated from the needle and distal electrodes; the resistance through the RTIL bridge connecting the needle and distal electrode is on the order of 1 MΩ.

The setup is then placed inside a vacuum chamber, with shielded cables connecting the leads to electrical ports for connection to the power supply, electrometer, and data acquisition system. The chamber is pumped down and held under high vacuum for no less than 10 h before testing. In order to achieve stable operation, the needle is first fired by manually increasing the potential until a beam current is measured. After finding the appropriate potential for the desired current level in one polarity, the potential is decreased to negative potentials. In order to achieve the same magnitude current in the opposite polarity, it may require a different magnitude of potential. Using these potential values, a square wave is programmed to achieve equal magnitude current in alternating polarities at specified frequencies. In reality, the potential profile is a trapezoid so as to not overload the power supply, with 0.1 s transition period.

Table 3.3: Summary of tested conditions for solid needle emitter with SS and RF distal electrodes. Listed currents are mean values.

			[emim][BF_4]	[emim][Tf_2N]
	time, s	separation, mm	current, nA	current, nA
SS	15	1.27	-115, +75	-100, -125, +75, +100
	15	2.54	-115, -125, +75, +115	-115, -125, +75, +115
RF	5400	2.54	-150, +80	-135, +135

For the solid stainless steel (SS) electrode, the emitter was operated at two needle tip to distal electrode spacing distances. The spacing was governed by the thinnest available eV Parts spacers, with a thickness 0.05 in. or 1.27 mm. As a result, the needle was tested at 1.27 and 2.54 mm. At each spacing, emission was attempted at two current levels per polarity. Table 3.3 summarizes the conducted tests for [emim][BF_4] and [emim][Tf_2N]. The tests were considered "successful" if data was gathered for at least three periods at currents close to the desired value. However, most tests included brief segments where the current jumped to higher or lower values, or the current decayed over time and needed to be adjusted by raising or lowering the applied potential. If these effects were seen to have had a noticeable impact on the collected data, they will be discussed in the appropriate data analysis section.

For the porous (RF) electrode, no stable operation was possible at a separation distance of 1.27 mm. All tests were then conducted at 2.54 mm. Furthermore, the emitted current was unstable and would either oscillate significantly or completely cut off at currents below ≈ 90 nA. As much longer times on the order of 90 min were required to see the probe potential variation, this unstable behavior was unacceptable. All tests were conducted at a targeted current of 100 nA so that results could be compared against SS electrode results.

3.4 Scalable ion Electrospray Propulsion System

The Scalable ion Electrospray Propulsion System (S-iEPS) was developed in the Space Propulsion Laboratory under the Game Changing Development Program of NASA's Space Technology Mission Directive [3]. The thruster, shown in Fig. 3-8, comprises

of a porous glass emitter chip, a gridded extractor electrode, a nonconducting silicon frame, a fuel reservoir, and a carbonized RF distal electrode. The reservoir, packed with a porous sponge-like material to help transport the RTIL propellant, also houses the distal electrode. A series of porous materials connects the reservoir (through the hole in the distal electrode and a matching hole in the tank) to the bottom of the porous glass emitter chip, providing enough hydraulic conductivity to resupply the chip with RTIL under normal operation. The emitter chip is manufactured from a porous glass substrate, which is polished with a Buehler 100 nm polishing pad. 480 tips, each with a tip radius on the order of 5 microns, are etched into the surface via laser ablation. As a voltage of $\approx 800\,\mathrm{V}$ is applied between the distal electrode and extractor electrode, the ionic liquid at each emitter tip is stressed under the electric field. Traditional theory predicted that this liquid meniscus would then form a Taylor cone under the balance of electric traction, hydraulic pressure, and surface tension; however, the exact geometry of this structure for RTILs is unconfirmed. Despite this lack of knowledge, it is understood that the meniscus forms a sharp feature which acts to greatly enhance the electric field strength, to the point where ions are able to overcome the potential barrier and evaporate. With careful design of the field topology and electrode apertures, the evaporated ions form a collimated beam and can then be used for propulsion and other focused ion beam applications.

As ions of one polarity are emitted, there is an excess of the countercharge left in the propellant. Due to bulk quasineutrality, this excess countercharge is expected to build up at interfaces in electrical double layers. In the case of this thruster geometry, there are two interfaces of interest. The first is at the liquid meniscus surface, from where the ion beam is emitted. From XRR measurements [126] it is known that a double layer can form at free surfaces. However, under the condition of constant current emission, the potential across this double layer should remain constant. This leaves the second interface of interest, at the surface of the carbon distal electrode. As charge in this double layer builds up, there is a corresponding increase in the

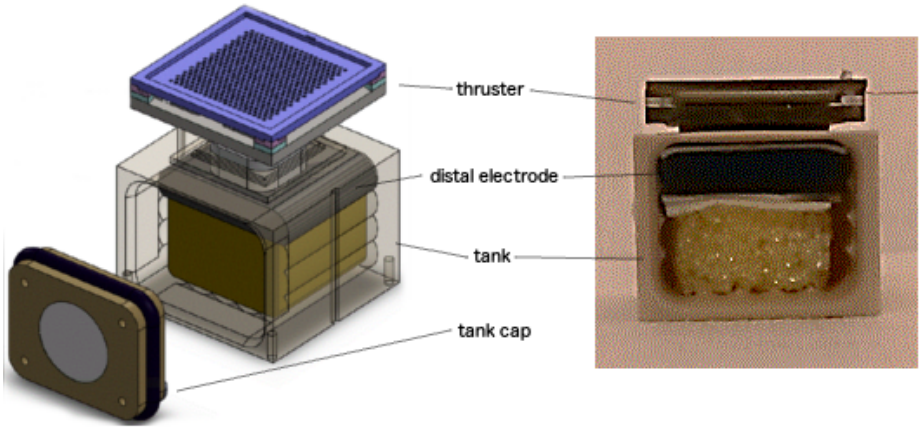

Figure 3-8: 3D model and photograph showing S-iEPS components. The thruster includes a 480-tip emitter array and an extractor electrode with apertures mated to each tip. A port connects the thruster to the tank, which includes the porous carbon electrode and an electrically inactive foam to ensure all propellant gets to the electrode. 3D model rendering by Corey Fucetola [152], photograph by David Krejci [153].

potential drop across the double layer as governed by capacitance,

$$I = \frac{dQ}{dt} = \frac{d}{dt}(CV) = \left(C + V\frac{dC}{dV}\right)\frac{dV}{dt} \tag{3.4}$$

where capacitance C is a function of voltage V. Once the double layer potential increases beyond the electrochemical window, the rate of Faradaic reactions increases dramatically. These reactions have been identified as life-limiting hazards in electrospray operation. Reactions tend to consume electrode materials, and thus electrode geometry can be compromised. The reaction products can also be considered impurities, which may change propellant properties as well as decrease polydispersive efficiency if they are emitted.

3.4.1 Experimental Setup

A standard test setup for the S-iEPS thruster as used in SPL [3] was modified for this experiment. A platinum wire probe was inserted into the thruster propellant reservoir so that the wire was in contact with the RTIL, as shown in Fig. 3-9. The thruster is typically operated with the high voltage applied at the carbon electrode

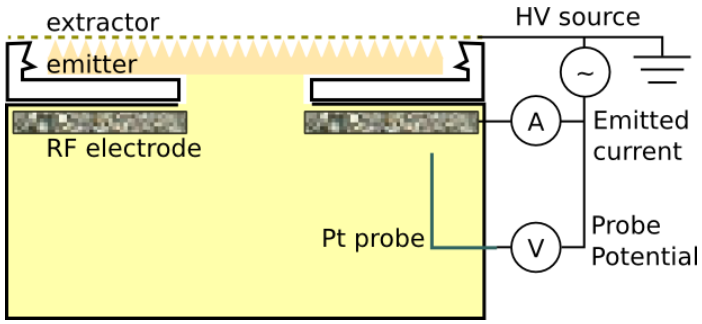

Figure 3-9: Cartoon drawing of S-iEPS thruster and tank with platinum probe. The extractor electrode is grounded and the carbon electrode potential is raised to some value to give the desired current. The probe measures the potential drop between the bulk RTIL and carbon electrode, offset by its own double layer potential drop.

and the extractor left as a floating ground. As such, in order to measure the double layer potential between the propellant RTIL bulk and the carbon electrode, the probe was expected to be at high potentials as well, on the order of 800 V. A Keithley electrometer was used to track the potential, but as it could not be floated to such high potentials, a differential potential measurement circuit was necessary. The circuit, shown in Fig. 3-10, uses an isolation amplifier to allow for measurement of the potential difference between the probe and carbon electrode at a floating potential. In order to get accurate measurements, the current throughput of this circuit must be kept minimal, and thus a high-impedance operational amplifier was included to allow only pico-Ampére levels of current.

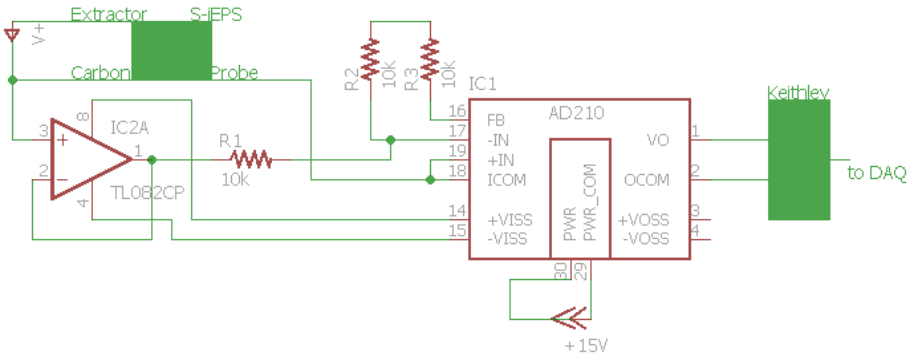

Figure 3-10: Circuit schematic for measuring double layer potential at S-iEPS carbon electrode

3.4.2 Experimental Methods

The S-iEPS thruster is fired by applying a high voltage to the carbon electrode while keeping the extractor at a floating ground. The emitted current is sensitive to the applied potential, and decreases slightly over time. A portion of the emitted current is intercepted by the extractor electrode, which from a thruster operation perspective is an inefficiency. However, from the perspective of studying the carbon electrode capacitance, the interception current is not of interest and only the emitted current needs to be tracked. As a current is emitted in the ion beam, excess charge builds up at the carbon electrode surface. This in turn raises the double layer potential in a manner governed by the differential capacitance. As such, as the thruster is fired in a single polarity, the double layer potential is expected to increase monotonically until Faradaic reactions start. Upon the onset of reactions, subsequently added charges are reduced or oxidized and do not add to potential.

To study potential growth in the double layer, the thruster was fired with a voltage alternation period of 300 s. Three current levels were tested, at 50, 100, and 150 µA. As noted above, the thruster is operated by controlling the potential and the emitted current tends to decrease over time. For this reason, the potential was manually adjusted in an attempt to keep the current as constant as possible. Fig. 3-11 shows a typical response output over one voltage alternation cycle.

It is important to note here that the potential difference between the probe and the carbon electrode is not exactly the double layer potential. Rather, there is a second double layer at the probe surface which has its own potential drop. However, the high impedance of the measurement circuit is expected to keep this probe from participating in any reactions, and the double layer potential at this probe can be assumed to remain constant. As such, the magnitudes measured in these tests are offset by some constant value while their derivative with respect to time is expected to be an accurate representation of the carbon electrode double layer properties.

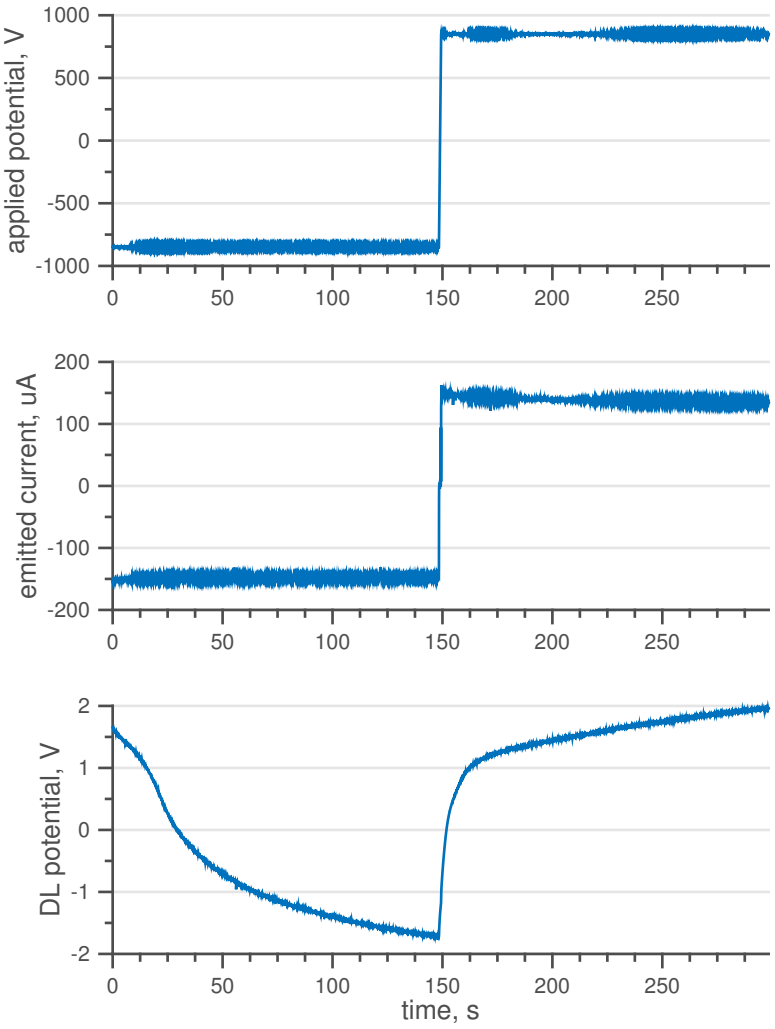

Figure 3-11: S-iEPS behavior over one typical voltage alternation cycle from a series of such cycles. Input voltage is manually adjusted to maintain output current $\approx$ 150 µA.

Chapter 4

Double Layer Capacitance

In this chapter, the results from the fundamental studies on RTIL double layers are presented. First, the two RTILs [emim][BF_4] and [emim][Tf_2N] are tested at flat platinum surfaces using impedance spectroscopy, described in section 3.1.3. The resulting Nyquist and Bode plots are analyzed to generate differential capacitance curves as a function of electrode potential. The curves for these two liquids at a platinum surface are new, with no known published versions to the author's knowledge; however, they are of comparable magnitude and shape to liquids of the same family. Using a second experimental setup, the RTIL double layers are studied at porous carbon electrodes and compared to the flat electrode results. It is shown that the local behavior of the RTIL EDL inside the porous matrix is fitted well by the same fitting parameters governing the flat electrodes. Data for higher frequencies in porous electrodes are dominated by a Warburg-like behavior, indicating the importance of diffusion for the spreading of the double layer throughout the porous matrix.

4.1 Flat Electrodes

Fundamental tests in electrochemistry are most often conducted on flat electrodes, either planar (e.g., Au, Pt) or spherical (with surface curvature $\gg$ double layer length scale, e.g., dropping mercury electrode). The flat surface allows for an approximation of one-dimensional behavior, allowing for interpretation with the 1D double layer

models presented in Ch. 1 and 2. In this study, a planar electrode was constructed by machining a stainless steel bolt to the desired dimensions and coating the working surface with platinum, as described in section 3.1.1.

4.1.1 Capacitance Modeling

Equivalent Circuit Models

Differential capacitance, as discussed in Ch. 1 and Ch. 2, is a commonly used parameter for probing EDL properties. However, capacitance is not a directly measurable property, and a model must be assumed in order to interpret the data. In the case of EIS, impedance is measured by studying the magnitude and phase shift of the current response to a sinusoidal voltage signal. In order to connect the obtained impedance to capacitance, an equivalent circuit model is designed using some network of ideal resistors, capacitors, inductors, and other electrical circuit models.

Many simple equivalent circuit models are known to accurately approximate specific electrochemical systems. When studying electrodes, two idealized cases are the ideally polarizable electrode at which no reactions take place and the ideally conducting electrode at which there is no reaction resistance, shown in Fig. 4-1. In the ideally polarizable electrode, an equivalent series bulk impedance is placed in series with a capacitor. The capacitor models the charge stored in the EDL and is not necessarily a constant value as the amount of stored charge increases. In the ideally conducting electrode, the bulk impedance is the only element, as the assumption calls for free transfer of electrons across the interface without resistance. In both cases, the bulk capacitance in parallel to the bulk resistance is often ignored [107] unless $C_{bulk} = \epsilon/L$ is expected to be a significant contribution.

When treating electrochemical systems, the electrochemical stability window is an often used limit within which the ideally polarizable electrode assumption is valid. As the potential increases beyond the anodic window limit, the reduction reaction becomes favored and Faradaic current flows. In the opposite polarity, if the potential is lowered beyond the cathodic limit, the oxidation reaction is favored and again

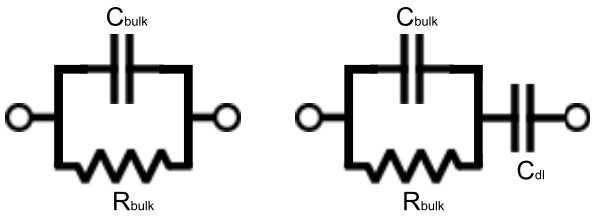

Figure 4-1: Simple equivalent circuits. Left: ideally conducting electrode, Right: ideally polarizing electrode.

Table 4.1: Electrochemical window of RTILs.

RTIL	cathodic limit [V]	anodic limit [V]	window [V]
[emim][BF_4]	-2.1	2.2	4.3
[emim][Tf_2N]	-1.8	2.5	4.3

Faradaic current flows. For water, the window is 1.229 V. The electrochemical window limit potentials for many RTILs exist in literature [18], of which relevant RTILs is reproduced in table 4.1.

In reality, some amount of Faradaic reactions take place within the electrochemical window due to the statistical nature of electron energies. Accounting for this, a more accurate model might include an additional resistance in parallel to the double layer capacitance of the ideally polarizable electrode. This typically high value of resistance accounts for the small Faradaic current flowing across the interface. This partially polarizable electrode is shown in Figure 4-2.

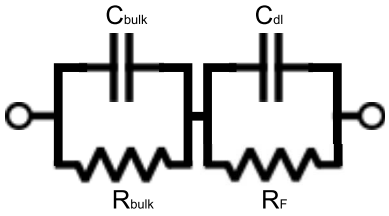

Figure 4-2: The partially polarizable electrode model includes the double layer capacitance and a Faradaic resistance at the interface.

Finally, non-ideal behavior of the double layer capacitance must be incorporated. Electrochemical capacitors often display frequency dispersion, or a strong dependence on the measurement frequency. Several different causes can lead to this, including electrode surface roughness. A common way to account for this is to replace the ideal capacitor in the equivalent circuit model with a constant phase element (CPE). A

Table 4.2: Circuit Element Impedances

element	impedance
Resistor	$Z_R = R$
Capacitor	$Z_C = {}^{1}/_{j\omega C}$
Inductor	$Z_L = j\omega L$
CPE	$Z_{CPE} = {}^{1}/_{Y_0(j\omega)^{\alpha}}$

CPE is a mathematical abstraction that adds an extra parameter α to account for non-ideal behavior in the double layer capacitance, to be discussed in more depth below.

Circuit Model Impedance

In order to fit the experimental data, the impedance of the model equivalent circuit must be obtained parametrically. The impedance of circuit elements including resistors, capacitors, and CPEs are well established as summarized in Table 4.2 and can be combined following simple rules for parallel and series circuits. The impedance of an ideal resistor is simply the resistance. For the ideal capacitor and inductor, the impedance is imaginary and dependent on frequency. If accounting for nonideal behavior using a CPE, the ideal capacitance C is replaced by admittance Y_0 and an additional parameter α is introduced. The case of $\alpha = 1$ clearly indicates ideal capacitance, whereas $\alpha = 0$ becomes a pure resistance. As such, $0 < \alpha < 1$ indicates a "leaky" capacitor, where some current may flow across the element.

Impedances of multiple circuit elements can be combined as with resistances in parallel and series circuits. Namely, for two elements in series,

$$Z_{series} = Z_1 + Z_2 \tag{4.1}$$

and for two elements in parallel,

$$\frac{1}{Z_{parallel}} = \frac{1}{Z_1} + \frac{1}{Z_2} \tag{4.2}$$

where Z_1 and Z_2 can take any of the element impedances listed above. Using these,

the impedances of the electrode models presented above can be calculated, neglecting bulk capacitance. We have for the ideally conducting electrode

$$Z_{ICE} = R_{bulk} \tag{4.3}$$

where the bulk resistance is the only circuit component. The ideally polarizable electrode gives

$$\begin{aligned} Z_{IPE} &= R_{bulk} + \frac{1}{j\omega C} \\ Z_{IPE} &= R_{bulk} + \frac{1}{Y_0 (j\omega)^{\alpha}} \end{aligned} \tag{4.4}$$

where the top equation is for an ideal capacitor and the bottom equation replaces the capacitor with a CPE. Finally for the partially polarizable electrode, the total impedance is

$$\begin{aligned} Z_{PPE} &= R_{bulk} + \frac{1}{\frac{1}{R_F} + j\omega C} \\ Z_{PPE} &= R_{bulk} + \frac{1}{\frac{1}{R_F} + Y_0 (j\omega)^{\alpha}} \end{aligned} \tag{4.5}$$

where again the top expression employs an ideal capacitor and the bottom equation a CPE.

Data Fitting

Impedance data is typically presented in two types of plots: Nyquist plot and Bode plot. The two plots represent the same data in different ways. The Nyquist plot plots the negative imaginary impedance against the real impedance, whereas the Bode plot plots both the complex impedance magnitude and its phase against the frequency. An example of each plot is shown in Fig. 4-4. Due to the equivalent circuit elements' impedances being treated theoretically in the complex plane, the fully assembled equivalent circuit theoretical impedance models are also represented in complex notation, $Z = Z_{real} + iZ_{imag}$. This is more directly visualized on a Nyquist

plot; however, this resulting plot does not readily convey information about the frequency. In order to properly analyze the system dynamics, data fitting is conducted in terms of $Z = f(\omega)$ and not $Z_{real} = f(Z_{imag})$. The ultimate quality of the fit then is more easily seen on a Bode plot, for which the data is first converted into magnitude and phase $Z = Z_{mod}e^{iZ_{ph}}$. In this work, the equivalent circuit model fits were conducted in two domains, one in terms of $(\omega, Z_{real}, Z_{imag})$ and the other in terms of $(\omega, Z_{mod}, Z_{ph})$, at each DC bias potential. It was confirmed that both fits converged to similar parameter values.

From the obtained experimental data, the simplest way to obtain the capacitance is by using Eq. 4.4 for the ideally polarizable electrode. This was taken as an appropriate assumption, based on the cyclic voltammogram in Fig. 3-2 which shows significant increase in Faradaic current at the electrochemical window voltage of $V \geq 1.2\,\mathrm{V}$ and equivalently no significant sign of reactions within the range of tested potentials. The experimental impedance data is first expressed in complex notation, which when compared with Eq. 4.4 gives

$$C = -(\omega Z_{imag})^{-1} \tag{4.6}$$

and the real (resistive) component of impedance is discarded. This method has been used in previous impedance studies of RTILs [107, 108]. A representative plot using this method is shown in Fig. 4-3, where the frequency was arbitrarily selected at ω =0.1 Hz and the complex impedance was given by the fitted ideally polarizable model. The capacitance as calculated by this method was seen to decrease monotonically with frequency, and thus the smallest frequency tested was selected to give the largest signal.

This method however raised uncertainties, in terms of how to interpret the capacitance magnitude and in the trustworthiness of the capacitance vs. potential curve shape. The shape was observed to change depending on the selected frequency. This was explained by studying the Nyquist plots at higher potentials. At applied potentials of $\Phi < -0.4$ and $0.8 < \Phi < 1.3$, the Nyquist plot began to curve down, indicating a resistive element in parallel to the double layer capacitance. An example is shown in

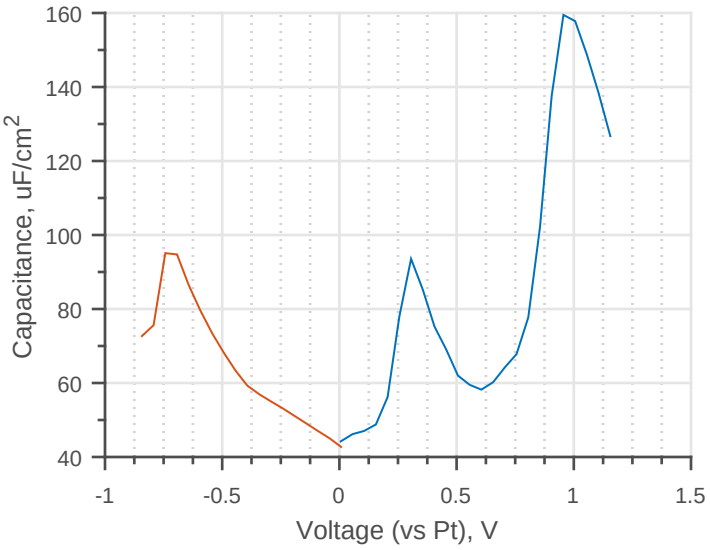

Figure 4-3: Capacitance plot calculated with Eq. 4.6 at the arbitrary frequency ω =0.1 Hz.

Fig. 4-6. This behavior would typically indicate the onset of Faradaic reactions, but the applied potential is too small to fit with the electrochemical window measured above, much less the limit potential values published in literature. The reactions then may be due to trace contaminants in the RTIL such as water, or they may be signs of dissociation reactions of bonded cation-anion pairs [154, 155]. Furthermore, although similar shaped plots were obtained across three trials conducted in the same day, subsequent repeat tests several weeks later in particularly humid conditions revealed significant variation in the obtained capacitance curves. This is discussed further in Appendix A.

In order to select the proper frequency at which to calculate capacitance, properties of Nyquist plots generated with idealized circuit models were considered. For a series RC circuit, or equivalently an ideally polarizable electrode without bulk capacitance, the Nyquist plot is a vertical line offset from the y-axis by the value of the resistance. Given such a Nyquist plot, one way to obtain the capacitance value would be simply using Eq. 4.6 at some arbitrary frequency. For a constant linear capacitor there is no frequency-dependence and the calculated capacitance would be constant. If however the ideal capacitor is replaced by a CPE with $\alpha < 1$, the calculated value

decreases monotonically with increasing frequency. Assuming for the moment that the α is of a high value and the element behaves closely to an ideal capacitor, it is now imperative that an appropriate frequency be identified. There are three reference points on the Nyquist plot where the frequency can be specified. The first is the x-intercept, corresponding to $\omega \to \infty$. On the other end, $-Z_{imag} \to \infty$ corresponds to $\omega = 0$. These two cases are equivalent to a short circuit and an open circuit, respectively. The third and most practical point is the intersection of the line with a 45° line through the origin. The frequency at that intersection in $\mathrm{rad\,s^{-1}}$ is equal to $1/RC$. On the Nyquist plot, decreasing values of α tend to rotate the line in a clockwise direction; however for high values of α at which the line is still close to vertical, this intersection point is a robust reference point at which the earlier confusion regarding capacitance magnitude can be accurately resolved.

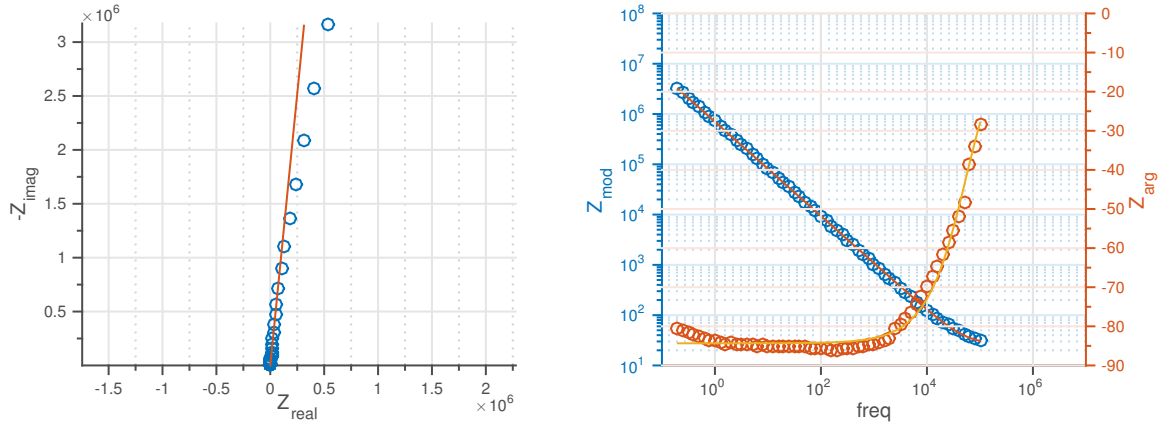

Figure 4-4: Impedance data for [emim][BF_4] at a flat electrode polarized to −0.03 V vs. Pt. Left plot shows the Nyquist plot, right plot shows the Bode plot. Fits generated with a series R+CPE ($\alpha = 0.94$) equivalent circuit.

The Nyquist plots generated for low polarization values in fact show such a slightly tilted line. As such, an equivalent circuit model consisting of a bulk resistance in series with a CPE is applied, as given by Eq. 4.4 and shown in both Nyquist and Bode plot forms in Fig. 4-4. Capacitance is then calculated as

$$-Z_{imag}(45°) = \frac{1}{j\omega C} \tag{4.7}$$

where $-Z_{imag}(45°)$ is the imaginary impedance value at the intersection point. Of course, the intersection point does not lie exactly on any of the discrete experimental data points. To estimate the frequency at the intersection point, the two adjacent data points were used to interpolate. The projections of the points onto the imaginary axis were used for a logarithmic interpolation, following

$$\omega_x = \omega_2^f \omega_1^{1-f} \tag{4.8}$$

where $f = {}^{Z_{imag,x}-Z_{imag,1}}/_{Z_{imag,2}-Z_{imag,1}}$ and the subscripts x, 1, and 2 indicate the intersection, the data point immediately below the intersection, and the data point immediately above the intersection, respectively. This method is inexact, as it assumes that the data points are spaced evenly apart. Such an assumption becomes less accurate at lower frequencies, but the intersection point was observed to be at a high frequency where the data points are clustered close to each other, and the distances between points do not vary too drastically. Also, the frequency must be factored by 2π to convert from Hz to rad s^{-1}. Fig. 4-5 shows a zoomed in view of the same Nyquist plot, indicating the intersection point.

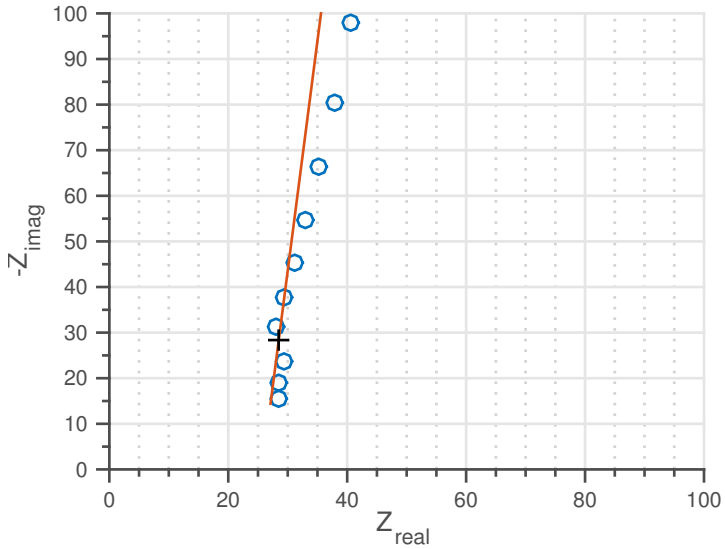

Figure 4-5: Zoomed in view of Nyquist plot at −0.03 V vs. Pt during a positive scan. The + indicates the intersection point between the data and the 45° line.

The capacitances calculated by this method can be verified by recalling that

Eq. 4.7 comes from an ideal series RC circuit in which $-Z_{imag}(45°) = Z_{real}(45°) = R_{bulk}$. Thus, we rearrange the equation as

$$\omega(45°) = \frac{1}{RC} \tag{4.9}$$

where we can plug in either a theoretical or experimentally measured value for R. The theoretical value was calculated above using Eq. 3.1. An experimental value can be extracted from the same Nyquist plot, by extrapolating the curve to the real axis and reading the value of the real impedance.

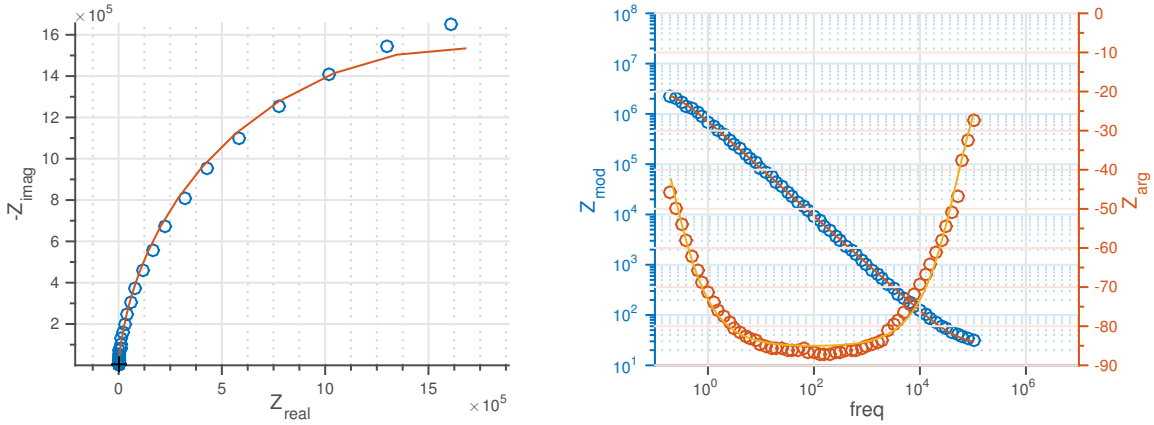

Figure 4-6: Impedance data for [emim][BF_4] at a flat electrode polarized to 0.87 V vs. Pt. The semicircle fit is achieved with a Randle's circuit, and the double layer capacitance can be calculated from the high frequency 45° intersection.

At larger applied DC bias, the Nyquist plot takes on greater curvature, incorporating qualities of a large semicircle. This can be interpreted as an additional resistance in parallel with the capacitive element, which physically represents Faradaic transfer resistance R_F as in Fig. 4-2. In such cases, the Faradaic resistance can be read from the Nyquist plot as the width of the semicircle. There are several difficulties with accurate determination of the semicircle. At moderate voltages, there is not enough curvature to determine any accuracy for the fit. At the largest voltages tested, the low frequency tail rises up, indicating another capacitive element in parallel with the bulk resistance, perhaps the bulk capacitance between the WE and CE surfaces or a Warburg element to account for ion diffusion to the electrode surface. This effect

limits the number of data points to be fitted with the semicircle. Finally, due to the imperfect capacitance, the semicircle is flattened vertically by an amount determined by the CPE α factor. Given the high values of $\alpha \approx 0.9$ found at lower DC biases, a good first approximation can be found by neglecting the flattening effect, instead fitting a perfect semicircle centered on the real axis to the data points excluding the rising tail. With a Randle's equivalent circuit fit, as in the example of Fig. 4-6, the frequency at the top of the semicircle is related to capacitance by

$$\omega_{top} = \frac{1}{R_F C} \tag{4.10}$$

where the frequency at the top ω_{top} can be found by interpolating between the two adjacent points using the angle as domain. These calculations can be used as a check for the capacitance values calculated with the above method based on the intersection at 45°. The large semicircle, as discussed above, is introduced by effects of the Faradaic transfer resistance and the system capacitance, which are at very different scales from the double layer charging of interest in this work. Zooming in to the high frequency region of the Nyquist plot where the 45° intersection occurs reveals a similar shape locally to the lower DC bias cases and can be interpreted as the simpler ideally blocking electrode with an imperfect capacitor. This use of only the high frequency behavior is discussed further and justified in Appendix A.

Figures 4-7 and 4-8 show the final capacitance curves calculated by the 45° intersection method discussed above, for [emim][BF_4] and [emim][Tf_2N], respectively. Both curves display two humps separated by a local minimum at some potential near the PZC. This is in qualitative agreement with previously published results found in literature, and also matches the "camel" shaped plots predicted by the more recent concentrated-solution double layer theories. Following the BSK theory, the double layer is in the overscreening phase at low to moderate potentials, between the two peaks. In this phase, the double layer thickness does not vary greatly, but the relative concentrations of cations and anions change in response to the increasing potential. This results in rising capacitance, similar to dilute solution models like GCS. As

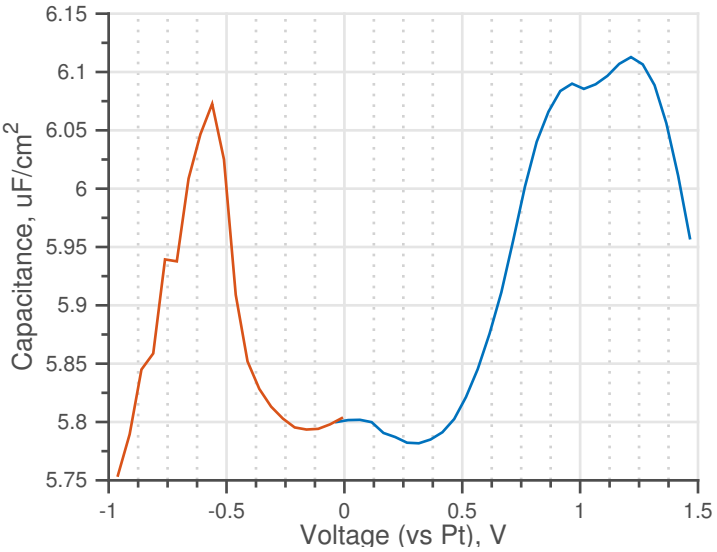

Figure 4-7: Capacitance vs. polarization curve for a Pt|[emim][BF_4] interface under vacuum.

the potential grows larger, the cation or anion population saturates, and the double layer must increase its thickness in order to accommodate further electrode charging. This then causes the capacitance to drop, akin to increasing the separation distance between two parallel plates. The two humps have different heights due to the size differences between cation and anion; in [emim][BF_4] the positive peak has a slightly larger magnitude due to the anion having a smaller size and in [emim][Tf_2N] the positive peak is expected to be lower due to the larger anion. Repeat tests for [emim][BF_4] gave consistent curves, and one test for [emim][Tf_2N] showed a slight upward shift only on the positive scan which gave a slightly more positive peak than for the negative scan. The repeatability of these curves is shown in Appendix A.

Capacitance curves for the two specific RTILs tested in this work were not available in previous literature. The most similar RTILs available were [bmim][BF_4] and [bmim][Tf_2N], tested at platinum and gold electrodes, respectively [108]. The curves from literature and the present work are grouped by anion and plotted together in Fig. 4-9. Due to the different cations, the curves are not expected to be the same. However, similar orders of magnitude would be some indication of consistency. The [BF_4] anion cases show a difference of about $1\,\mu F\,cm^{-3}$ near their local minima, and

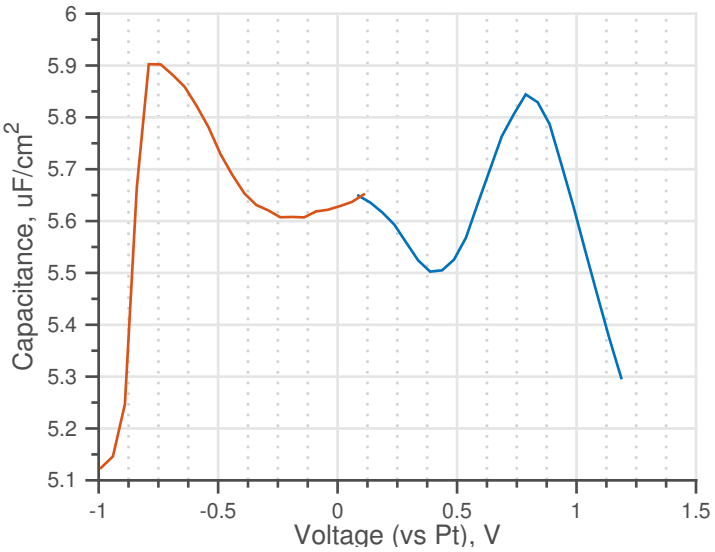

Figure 4-8: Capacitance vs. polarization curve for a Pt|[emim][Tf_2N] interface under vacuum.

a similar difference in capacitance between the minimum and peak. Although the shorter alkyl chain length of [emim] compared to [bmim] suggests that it should have the higher capacitance [86, 107], this difference may also be due to the different experimental apparatus used. For example, the electrode used here may be smoother, as surface roughness is known to increase the value of capacitance [93]. The data gathered in this work also shows a larger gap between the two peaks by almost 0.5 V. In fact, the Kornyshev model given in Eq. 2.2 predicts even closer peaks, with peak separation about 10% of the experimental curve as shown in Fig. 4-10. Experimental data has been observed to feature peaks farther apart than models and simulations before in literature [86], where addition of neutral tails to MD simulations was found to predict peaks somewhat farther apart but still not quite far enough to match experimental results. The [TF_2] anion cases are much more difficult to compare, as the curve from literature does not display the shape typically expected of RTILs. The magnitudes are comparable, but beyond that no conclusions can be drawn. This particular curve from literature was taken at a different electrode material, gold instead of platinum, and that may have an effect on the curves. Finally, the magnitudes of the measured capacitances are two to six times smaller than the first order estimates

from linear theory presented at the beginning of this section. The estimates were based on charge screening in a monolayer of counterions. In contrast, the actual double layers in RTILs are expected to exhibit a multilayered structure which effectively increases the capacitor separation distance. Two to six layers fits well within the range of observed numbers of ion layers in literature as reviewed in Ch. 2.

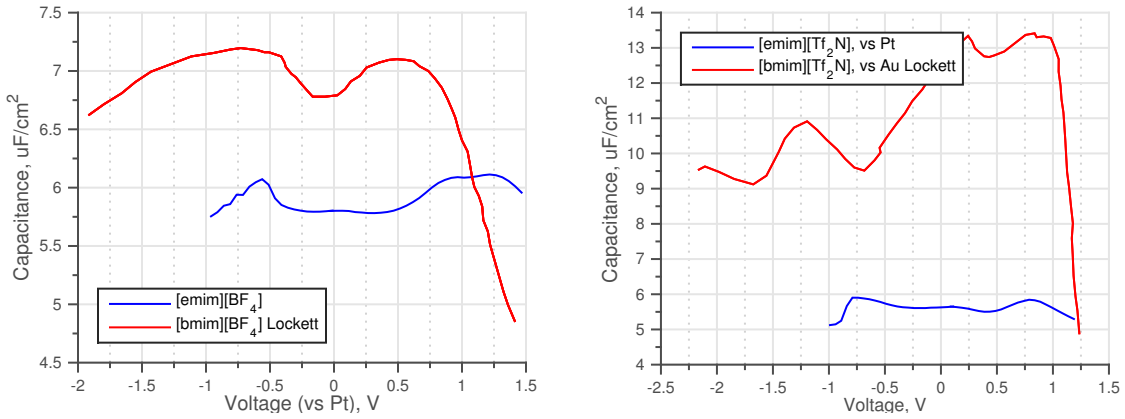

Figure 4-9: Comparisons of capacitance curves to those from literature. The present work used RTILs with the [emim] cation, whereas the literature values were taken with the [bmim] cation.

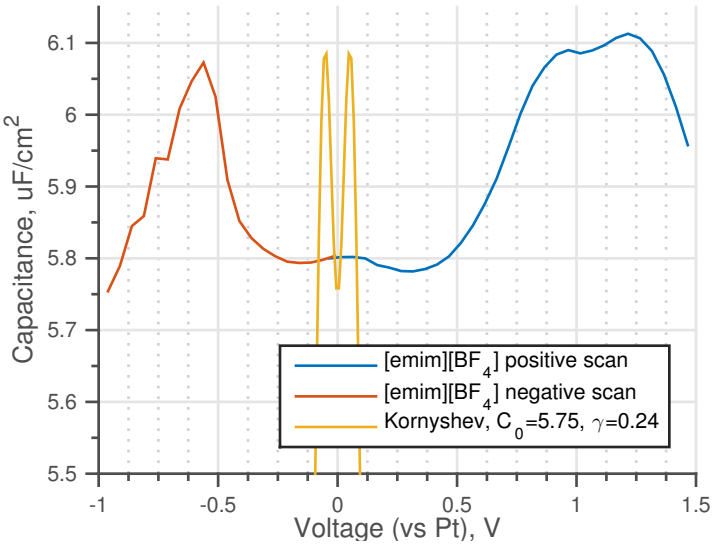

Figure 4-10: Comparison of experimentally obtained capacitance curve to Kornyshev model (Eq. 2.2) with C_0 and γ selected to match hump height.

One final comparison can be made between the experimentally obtained curves

and the mean field model. In the BSK model, asymptotic analyses were conducted in three potential ranges, with the scalings given in Eq. 2.5. According to these scaling laws, the decaying wings of the capacitance curve for $\gamma \neq 0$ varies as $\sim V^{-1/4}$ at moderate voltages and as $\sim V^{-1/2}$ at larger voltages. This can be visualized on a log-log plot of capacitance vs voltage, in which the power factor becomes the slope. Fig. 4-11 shows the positive tail for [emim][BF_4] and [emim][Tf_2N] and slopes corresponding to the two scaling regimes. Although the potential range tested does not extend far enough to verify the inverse square root clearly, the slope does tend near $^{-1}/_{4}$ at one point then begin to slope down in the correct direction. This finding gives further support to the importance of crowding effects that dominate the double layer structure at larger electrode potentials.

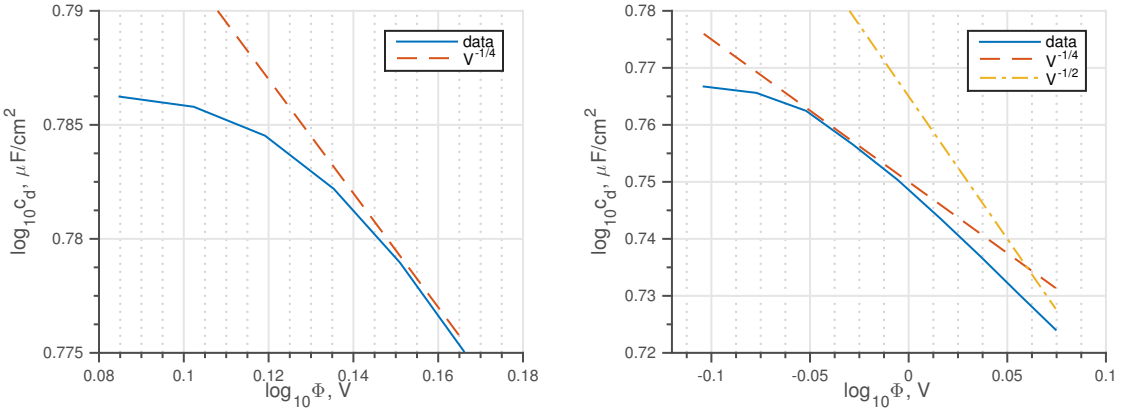

Figure 4-11: Comparisons of capacitance curve tails to asymptotic scaling laws of the BSK model. The slopes approach $^{-1}/_{4}$ at moderate voltages then tend towards $^{-1}/_{2}$ at larger voltages.

The capacitance curves generated by electrochemical impedance spectroscopy for the two RTILs show the major characteristics suggested by the most recent theoretical models, namely a local minimum between two peaks and decreasing wings beyond those peaks. The magnitudes of the capacitance are also close to those given in literature for similar RTILs. This suggests that the electrochemical cell is behaving properly. For the alternative methods attempted in Appendix B, the impedance-generated capacitance curves here serve as the references to which their results will be compared.

4.1.2 Continuum Model for RTIL Capacitance

The two capacitance curves generated with impedance spectroscopy are valuable resources both for scientists looking for such information, and for validating theoretical models of the RTIL double layer. Recent continuum mean-field models, described in Ch. 2, have finally begun to capture qualitatively the features seen in experimentally obtained capacitance curves. Collaborators from Professor Bazant's group have proposed a new model, effectively merging the modified Poisson equation of the BSK model and the multi-tiered lattice model of Han et al. This model should then be able to capture both electrostatic correlation effects and asymmetry in ion sizes, albeit still with spherical ion models. The capacitance curves from this work are being used to tune the new model, with the particular goal of quantifying the effects of ion size asymmetry. This will lead to the next step in continuum modeling of the RTIL double layer behavior, and provide a new tool in RTIL selection for future applications.

4.2 Porous Electrodes

Porous electrodes are implemented for one particular goal, to increase the available surface area. In fuel cells or supercapacitors, the larger area allows for more reaction sites to increase energy production or pseudocapacitance for energy storage. In the case of electrospray devices, the larger surface area is useful for increasing the total double layer capacitance and thus allowing for longer operation in a given polarity before Faradaic reactions begin to degrade the electrode and electrolyte. In the case of pore sizes being on the order of the double layer thickness or smaller, it is known that the double layers overlap and lead to qualitatively different behavior [156]. It is unclear however how pores much larger than the double layer may affect local double layer structure and thus its capacitive properties. In this study, the same impedance method as for the flat electrode tests above is conducted at microporous carbon electrodes described in section 3.2.1 for comparison at various applied potentials.

4.2.1 Capacitance Modeling

RC Transmission Line Models

Porous electrodes are often analyzed using an "*RC* transmission-line" model, in which pores are characterized by a network of series resistances per length R' and parallel capacitances per length C'. Mathematically, this model is identical to the semi-infinite linear diffusion Warburg impedance [157],

$$Z_W = A_W \left(\frac{1}{\sqrt{\omega}} + \frac{1}{j\sqrt{\omega}} \right) \tag{4.11}$$

where A_W is the Warburg coefficient. Two derivations of the Warburg impedance are given by Taylor and Gileadi, with emphasis on the physical origin of its capacitive behavior [158]. The equivalent circuit case with the *RC* network was solved by de Levie [43], using the "linear diffusion" equation

$$\frac{\partial^2 \Phi}{\partial z^2} - R'C' \frac{\partial \Phi}{\partial t} = 0 \tag{4.12}$$

under a harmonic perturbation $\Phi(0,t) = \Phi_0 \sin \omega t$. Use of the frequency-independent C' gives the 45° phase lag; generalization for other phase shifts have been demonstrated with R' and C' expressed using gamma functions [159].

For small electrodes in which the double layer may diffuse entirely across all pore surfaces, the semi-infinite assumption must be modified. In fuel cell analyses, the impedance model is often modified with a Dirichlet boundary condition, where ion concentration and thus double layer charge is zero at $x = L$. This is analogous to having a resistive cutoff, where the finite length *RC* transmission line is shorted at the end. This model is often used to portray porous electrodes, where the end of the pore is directly connected (electrically shorted) to the external circuit, and also diffusion of salt across a finite domain. This "finite-length Warburg" model results in impedance of the following form:

$$Z_{FLW} = R'L \sqrt{\frac{Z_S}{R'}} \tanh \sqrt{\frac{R'}{Z_s}} \tag{4.13}$$

where Z_s is a more general surface impedance per length in place of the ideal capacitance per length C'. This can be represented schematically as a finite RC transmission line, shown in Fig. 4-12.

A second possibility is to use a Neumann boundary condition, or a zero-flux boundary which makes the system act as a capacitor at low frequency. This "bounded Warburg" model gives impedance of the form

$$Z_{BW} = R'L\sqrt{\frac{Z_S}{R'}}\coth\sqrt{\frac{R'}{Z_s}} \tag{4.14}$$

where the hyperbolic tangent is replaced by a hyperbolic cotangent. This model is often applied to intercalation batteries and to supercapacitor electrodes, in which ions that reach the end of the pore do not immediately react at the surface but rather serve to charge up the local double layer. In both Eq. 4.13 and Eq. 4.14, a good starting point for the generalized surface impedance may be a CPE, as can be seen by comparison to the results of section 4.1.

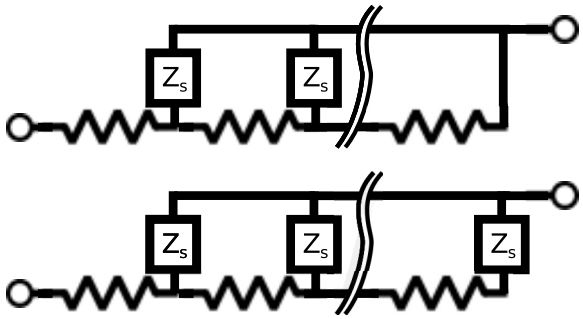

Figure 4-12: Finite length RC transmission line models. Top: Resistive cutoff for porous electrodes or diffusion. Bottom: Capacitive cutoff for solid diffusion in intercalation electrodes.

In the system under present consideration, the porous electrode serves like that of a supercapacitor and builds up a double layer even at the pore end. As such, the bounded Warburg model is considered in further detail. As formulated above, the generalized surface impedance Z_s should describe the double layer charging at some local area within the porous structure, without regard to the diffusion dynamics. It is then hypothesized that this surface impedance can be taken directly from the

parallel-plate experiment results of section 4.1, and appropriately scaled by surface area. It was concluded that those results, especially at smaller applied voltages, could be interpreted as a constant phase element in series with bulk electrolyte resistance. This impedance behavior is given by three fitting parameters, resistance R and CPE parameters Y_0 and α. Due to the different geometries of the two experimental setups, the bulk resistance will not be equal. However, Z_S relies only on the two other parameters Y_0 and α, and all other parameters of the impedance model can be selected via best fit to the porous electrode data. Following the more complete derivation in Appendix C, the bounded-Warburg type impedance has the form

$$Z(\omega) = C_1\sqrt{Z_s}\coth\left(C_2\sqrt{\frac{1}{Z_s}}\right) \tag{4.15}$$

where $Z_s = Z_{CPE} = {}^{1}/_{Y_0(j\omega)^\alpha}$ with Y_0 and α taken from parallel plate data fits, $C_1 = \frac{1}{A_{cs}}\sqrt{\frac{A_{pp}}{\bar{a}\sigma'}}$, and $C_2 = \sqrt{\frac{\bar{a}L^2}{\sigma' A_{pp}}}$. The area terms A_{cs} and A_{pp} are cross sectional area of the porous electrode and the parallel plate WE area. L is the thickness of the porous electrode, such that $A_{cs}L$ is the volume of the electrode. $\bar{a}$ is the specific wall area, defined as wall area per volume. σ' is an apparent conductivity, which is the RTIL conductivity σ scaled by factors determined by pore geometry.

Data Fitting

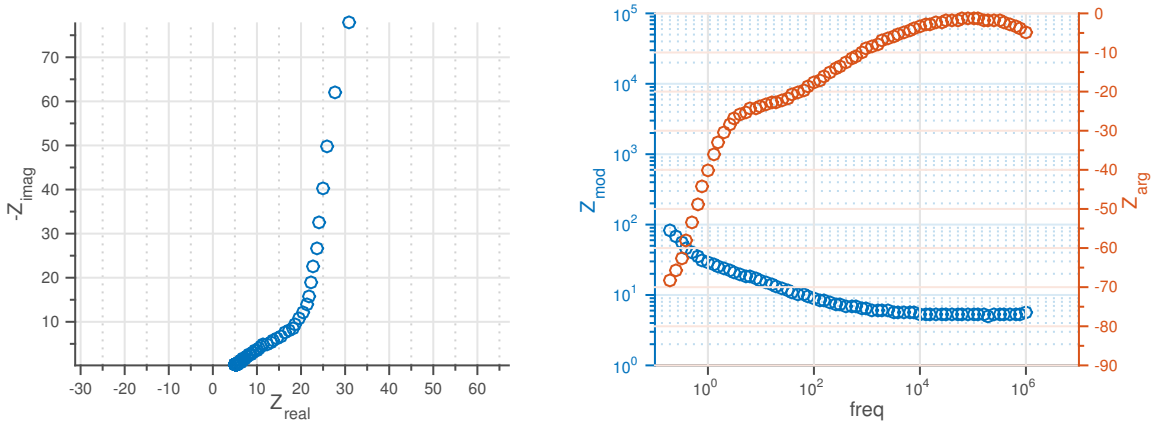

Figure 4-13: Impedance data for [emim][BF_4] with a porous electrode polarized to 0.01 V. Left plot shows the Nyquist plot, right plot shows the Bode plot.

Fig. 4-13 shows a representative set of Nyquist and Bode plots from the porous electrode experiment. Both plots reveal significantly different behavior from the flat parallel plates results. The porous electrodes give significantly smaller impedance magnitudes, by about five orders of magnitude at the lowest frequencies. The smaller impedance can be explained in part by the larger amount of available surface area along the pore walls. However, the plot of the phase angle reveals differences in behavior beyond the available surface area. Whereas the flat electrode started almost purely capacitive at low frequency before becoming closer to pure resistance at high frequency, the porous electrode never shows an argument larger than $|70°|$ but instead approaches much closer to ideal resistance at higher frequencies. The transition from capacitive to resistive behavior occurs at much lower frequencies, around 1 Hz as opposed to 10 kHz in the parallel plate results. The Nyquist plot also reveals information about the setup's behavior. The highest frequencies are close to a line slanted at $\approx 34°$. This behavior holds until the real component of impedance reaches $Z_{real} \approx 20$ then turns sharply upwards. According to the hypothesis put forth in the introduction of this chapter, this sharp change in behavior is expected to delineate the transition from ion diffusion to surface impedance. At first glance, this seems to be a reasonable conclusion: a slanted line close to 45° is indicative of a generalized Warburg diffusion [159], and the lower frequency section is a line much closer to vertical, similar to the CPE behavior seen in the parallel plate electrode results.

Fig. 4-14 and 4-15 show the porous electrode impedance data for [emim][BF_4] fitted with Eq. 4.15 plus a series bulk electrolyte resistance. In order to find the appropriate values of Y_0 and α, the parallel plate impedance result from the test with the closest applied DC voltage was selected. Using those two values as constants, the data was fitted with three parameters, R_{bulk}, C_1 and C_2. As was discussed in section 4.1, at higher applied potentials the Nyquist plot for the parallel plate tests took on curvature indicating some leakage current. In order to estimate only the double layer capacitor behavior as modeled by a CPE, a high-frequency filter was employed as is discussed in Appendix A. The filter threshold frequency was selected as 100 Hz to get reasonable fits to the porous electrode data and to ensure enough

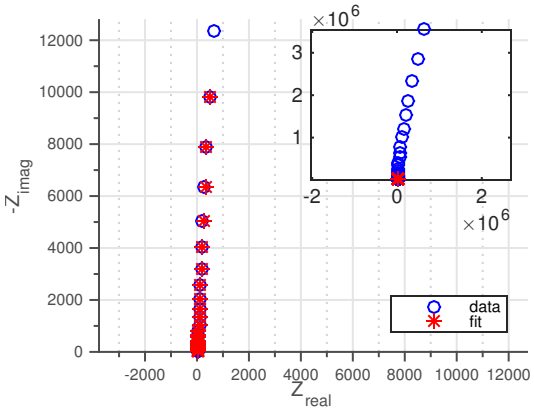

(a) Parallel plates at −0.011 V

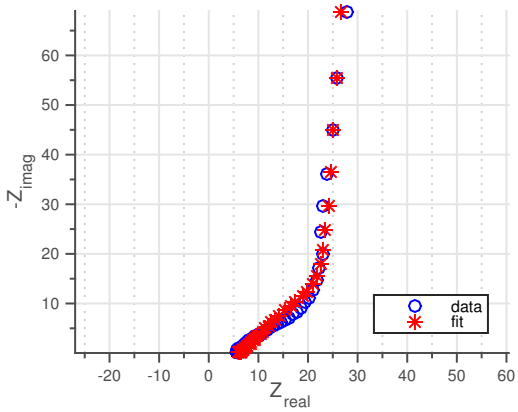

(b) Porous electrode at −0.035 V

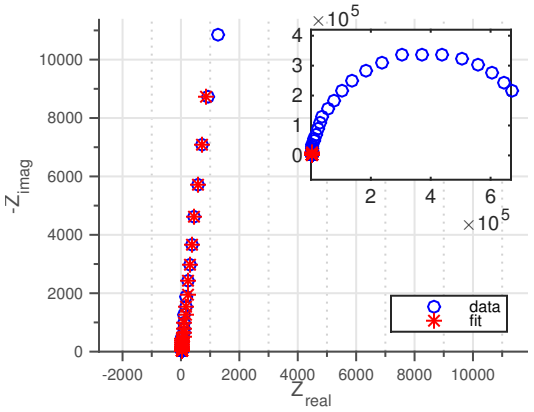

(c) Parallel plates at −0.511 V

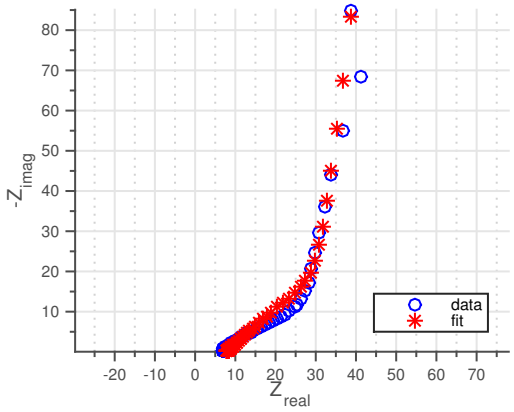

(d) Porous electrode at −0.535 V

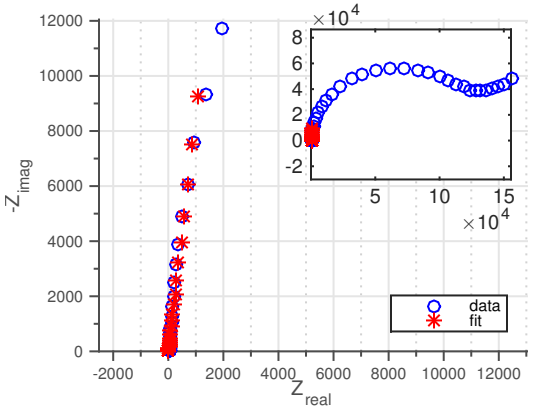

(e) Parallel plates at −0.911 V

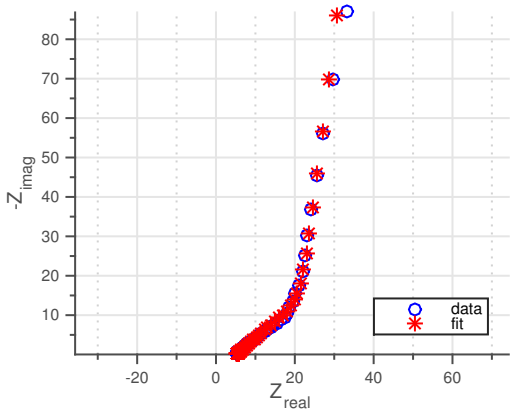

(f) Porous electrode at −0.935 V

Figure 4-14: [emim][BF_4] impedance data for parallel plate and porous electrodes at similar negative polarizations. The fitting parameters from the high frequency (> 100 Hz) portion of the parallel plate data were used to generate the porous electrode fits. Insets show the full Nyquist plot.

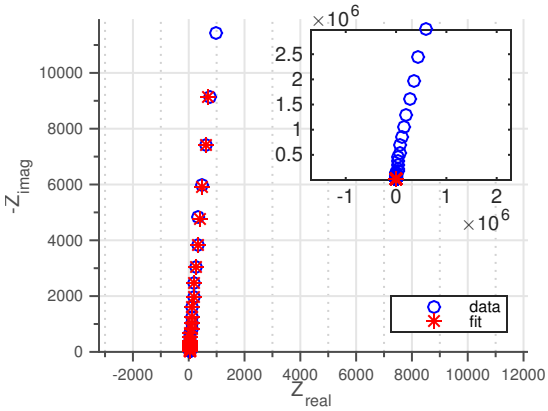

(a) Parallel plates at 0.016 V

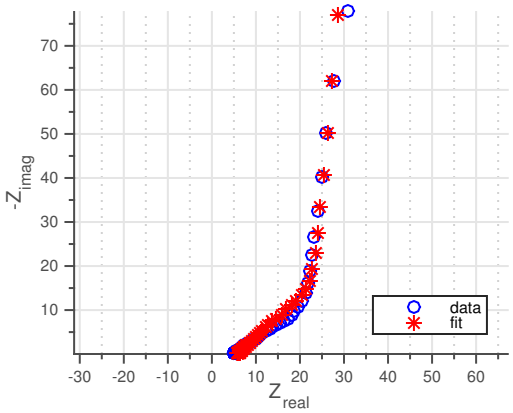

(b) Porous electrode at 0.013 V

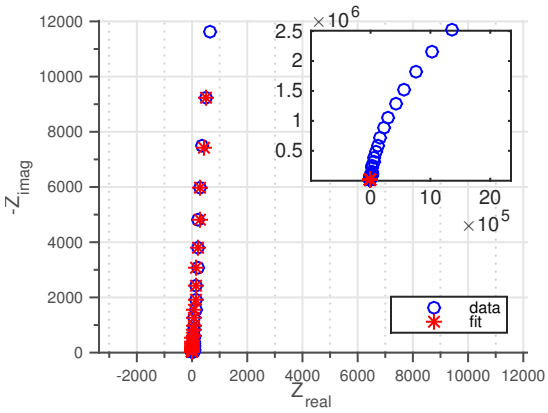

(c) Parallel plates at 0.766 V

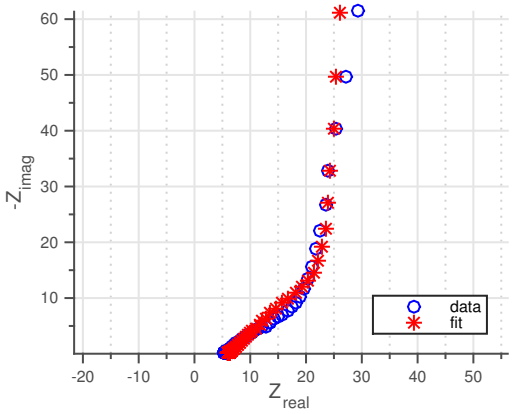

(d) Porous electrode at 0.763 V

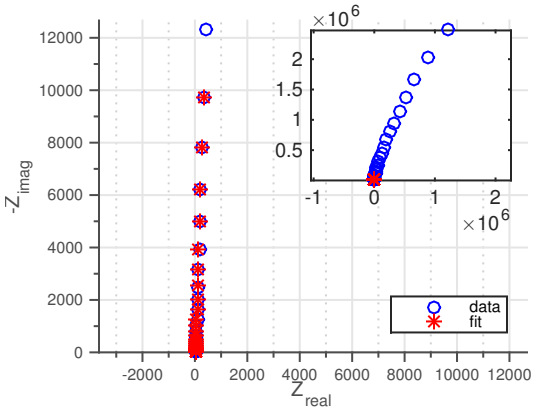

(e) Parallel plates at 1.466 V

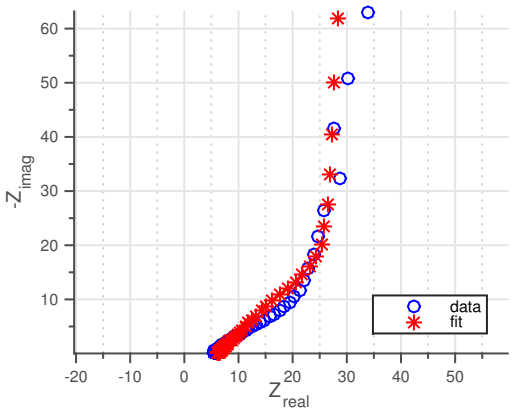

(f) Porous electrode at 1.463 V

Figure 4-15: [emim][BF_4] impedance data for parallel plate and porous electrodes at similar positive polarizations. The fitting parameters from the high frequency (> 100 Hz) portion of the parallel plate data were used to generate the porous electrode fits. Insets show the full Nyquist plot.

data points were accounted for in the fitting. The equivalent data for [emim][Tf_2N] is shown in Fig. 4-16 and 4-17.

As stated in the derivation of Eq. 4.15, the two fitting parameters C_1 and C_2 represent combinations of physical parameters. The values of porous electrode cross sectional area A_{cs}, porous electrode thickness L, and parallel-plate electrode area A_{pp} are known from the experimental designs. This leaves two unknowns, specific wall area $\bar{a}$ and apparent conductivity $\sigma' = \frac{\epsilon_p \sigma}{\tau}$. Decomposing σ' reveals two unknown parameters, porosity ϵ_p and tortuosity τ which along with $\bar{a}$ are important characteristics of the porous electrode structure. Rearranging C_1 and C_2 gives

$$\bar{a}\epsilon_p = \frac{\tau A_{pp}}{\sigma A_{cs}^2 C_1^2} \tag{4.16}$$

$$\frac{\bar{a}}{\epsilon_p} = \frac{\sigma A_{pp} C_2^2}{\tau L^2} \tag{4.17}$$

$$\bar{a} = \frac{A_{pp} C_2}{A_{cs} L C_1} \tag{4.18}$$

$$\epsilon_p = \frac{\tau L}{A_{cs} C_1 C_2} \tag{4.19}$$

for specific wall area and porosity in terms of the fitting parameters and tortuosity. By expressing total wall area and total pore volume in terms of characteristic pore radius r_p, characteristic pore length l_p, and some number n_p of pores, it is possible to define

$$\frac{\epsilon_p}{\bar{a}} = \frac{\frac{\pi r_p^2 n_p l_p}{A_{cs} L}}{\frac{2\pi r_p n_p l_p}{A_{cs} L}} = \frac{r_p}{2} \tag{4.20}$$

for a characteristic pore radius in terms of $\bar{a}$ and ϵ_p.

For each Nyquist plot, there are two fitting parameters with three unknowns, $\bar{a}$, ϵ_p, and τ. Tortuosity is a measure of how convoluted pore pathways are, defined as the ratio of length along the pore between two points and the straight line connecting those same two points. τ then must be a value greater than or equal to 1. As a starting point, $\tau = 1$ is assigned to get numbers for porosity and pore size, and later the accuracy of those numbers is verified using scanning electron microscopy.

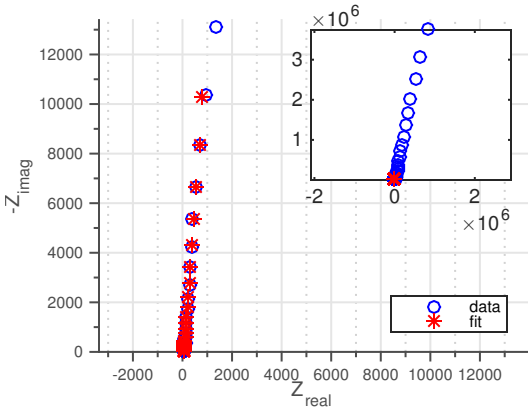

(a) Parallel plates at −0.034 V

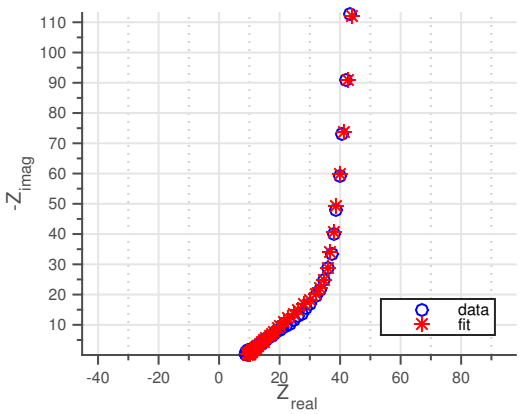

(b) Porous electrode at −0.032 V

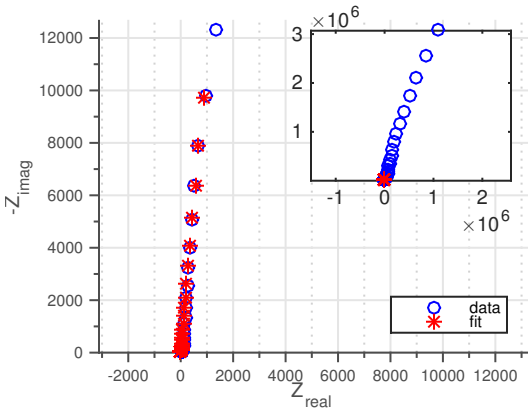

(c) Parallel plates at −0.534 V

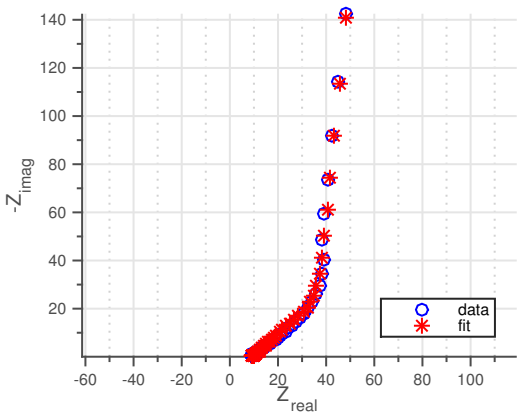

(d) Porous electrode at −0.532 V

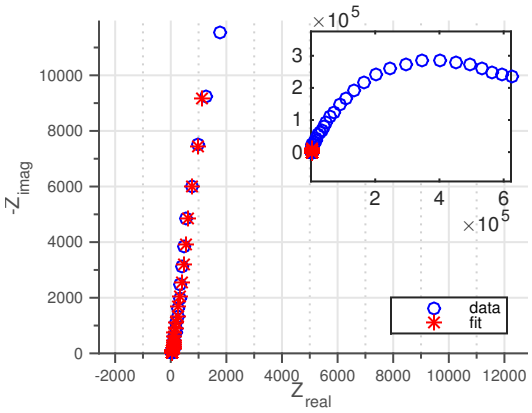

(e) Parallel plates at −1.034 V

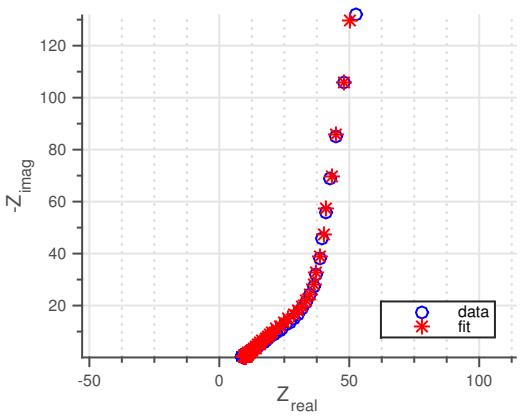

(f) Porous electrode at −1.032 V

Figure 4-16: [emim][Tf_2N] impedance data for parallel plate and porous electrodes at similar negative polarizations. The fitting parameters from the high frequency (> 100 Hz) portion of the parallel plate data were used to generate the porous electrode fits. Insets show the full Nyquist plot.

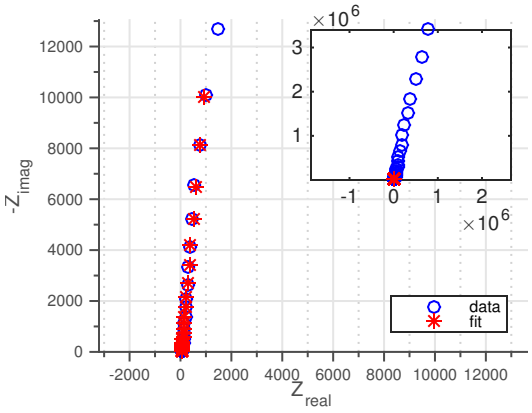

(a) Parallel plates at 0.063 V

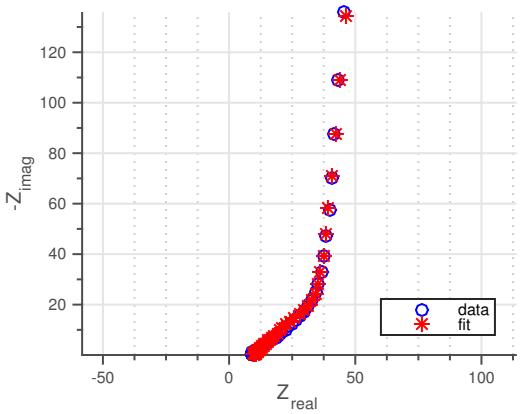

(b) Porous electrode at 0.049 V

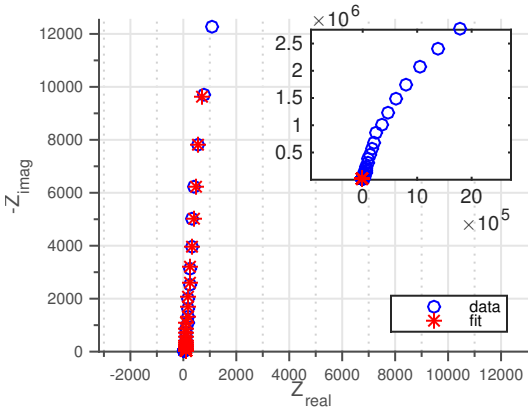

(c) Parallel plates at 0.613 V

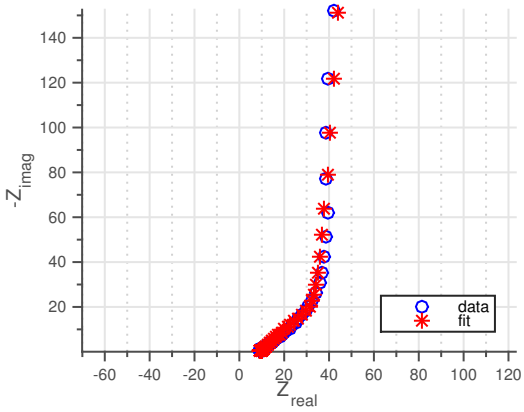

(d) Porous electrode at 0.599 V

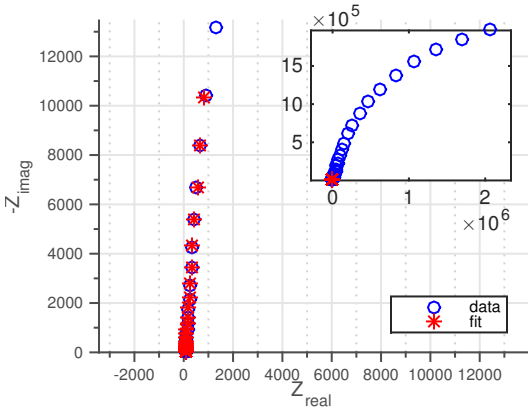

(e) Parallel plates at 1.163 V

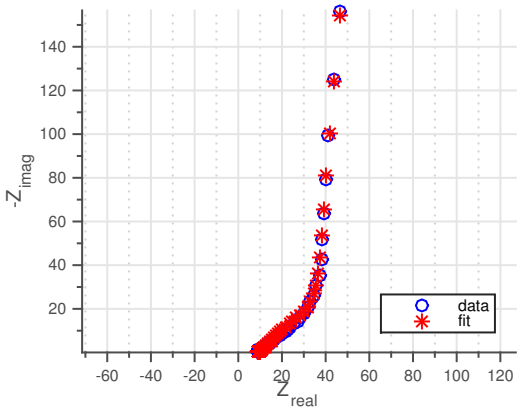

(f) Porous electrode at 1.149 V

Figure 4-17: [emim][Tf_2N] impedance data for parallel plate and porous electrodes at similar positive polarizations. The fitting parameters from the high frequency (> 100 Hz) portion of the parallel plate data were used to generate the porous electrode fits. Insets show the full Nyquist plot.

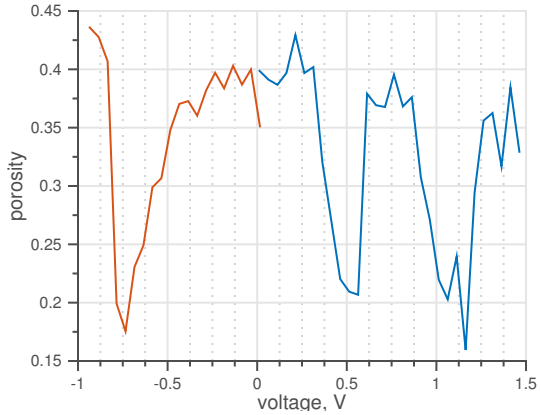

(a) Porosity calculated from [emim][BF_4] fitting parameters

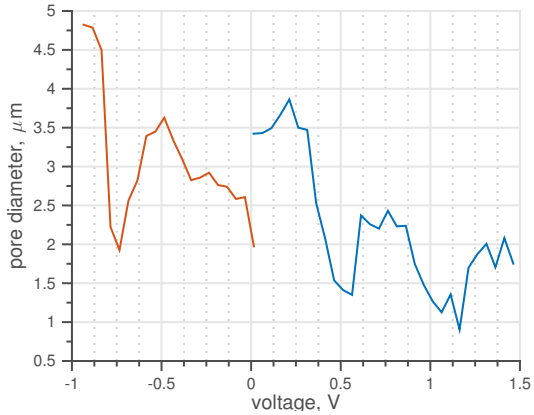

(b) Characteristic pore size calculated for [emim][BF_4]

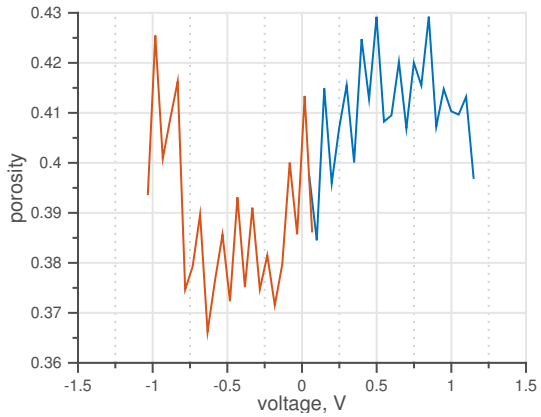

(c) Porosity calculated from [emim][Tf_2N] fitting parameters

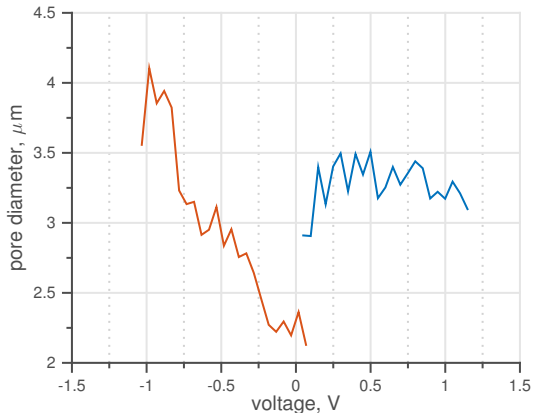

(d) Characteristic pore size calculated for [emim][Tf_2N]

Figure 4-18: Porous structure characteristics calculated from Nyquist plot fitting parameters at various bias potentials.

The values of porosity ϵ_p and pore size r_p are shown in Fig. 4-18. These parameters are not dependent on voltage, but were calculated from the impedance spectra fits taken at each indicated polarization. Since the same electrode is used across all experiments, these values are expected to remain constant. The values in fact stay within a factor of two. Furthermore, without any constraint on the fitting process, the values for ϵ_p were in the correct range $0 < \epsilon_p < 1$, as required by definition.

Pore size statistics were also estimated from a scanning electron microscope (SEM) image, using a MATLAB script to identify lines of sharp contrast to identify pores as in Fig. 4-19. Assuming this 2D section to be representative of the entire bulk, a pore

size distribution is calculated as well as a pore area fraction ${}^{A_{pore}}/_{A_{total}}$, which can be interpreted as a 2D projection of porosity. The mean pore diameter was found to be 2.59 µm, with a standard deviation of 3.68 µm. The pore area fraction $\epsilon_{p,2D}$ was 0.40, which corresponds to a 3D porosity of $\epsilon_p = \epsilon_{p,2D}^{3/2} = .25$. This number multiplied by the total electrode volume gives the total pore volume, $\epsilon_p A_{cs} L$. This volume can then be divided by a characteristic pore section area πr_p^2, calculated from the mean pore diameter, to find a "total length" $n_p l_p$ of pores, assuming cylindrical pores. With the assumption of cylindrical pores, an estimation of the total wall area $2\pi r_p n_p l_p$ and scaling by mass gives $9269.8\,\mathrm{cm^2\,g^{-1}}$. Resorcinol formaldehyde has been known to have specific surface areas on the order of $100\,\mathrm{m^2\,g^{-1}}$, but this porosity can change drastically by small changes in chemical composition during synthesis.

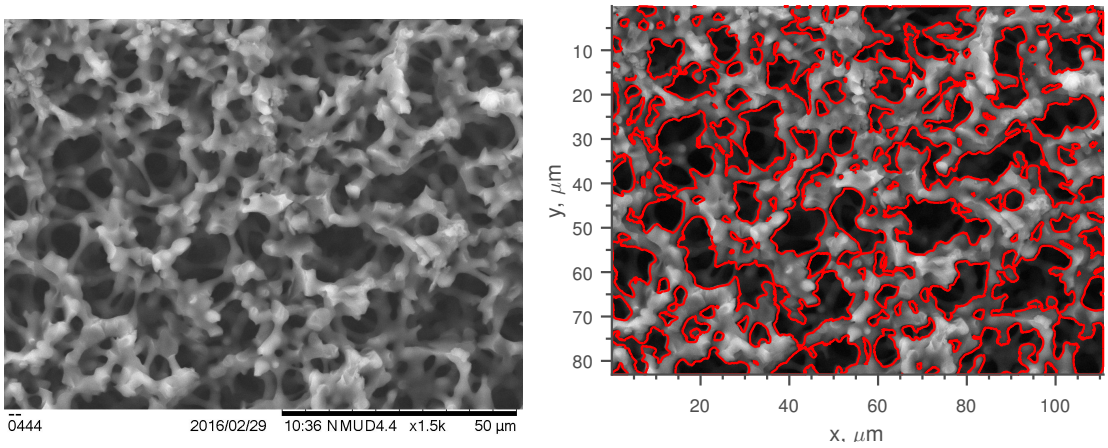

Figure 4-19: Raw and processed SEM images for characterizing carbon xerogel porosity. The pore size was determined to have a mean diameter of 2.5913 µm with standard deviation 3.6807 µm.

Comparing the results from the SEM image statistics to the values calculated from the impedance fitting parameters shows that the numbers are quite close, with especially the mean pore diameter found on the SEM being in the middle of the range calculated from impedance. This suggests that the initial assumption of $\tau \approx 1$ was good.

4.3 Conclusions

In the first set of experiments at flat electrodes, two new capacitance curves were produced for RTILs previously unavailable in literature. These curves are of the "camel"-shaped variety as described by Kornyshev [68]. This shape indicates that the double layer does indeed go through the two structural regimes for charge screening as captured by the BSK model, overscreening and crowding. More sophisticated models to be developed in the future with accommodation for different ion sizes and shapes should use experimentally obtained curves like these for tuning and parametrization.

The major finding of the second experiment was the confirmation that the porous electrode wall behaves similarly to flat electrodes locally. Although the Nyquist plots look qualitatively different, this is explained by the additional diffusion time scale imposed by the transport-limitation in porous matrices. The high frequency portion of the flat electrode Nyquist plot captures the capacitive behavior of the interface, whereas it is the lower frequency region of the porous electrode Nyquist plot that shows the same. By using impedance spectra taken at similar DC bias potentials, the two electrodes' capacitive behaviors were compared and found to be described by the same constant phase element parameters, scaled appropriately by area. This analogous local behavior is expected to hold for cases when $r_p \gg \delta$ where δ is the double layer thickness. Future studies may attempt similar analyses for electrodes prepared at a range of porosities extending down to $r_p < 1\,\mathrm{nm}$ in order to confirm this and to study how the behavior changes at nanoporous electrodes.

Chapter 5

Double Layer Charging

In this chapter, the behaviors of electrospray systems will be studied with consideration of the findings from the fundamental studies in Ch. 4. Whereas the capacitance studies were for static, equilibrium double layers, the dynamical tests described in this chapter are for nonequilibrium double layers under charging conditions. First, the porous electrode charging behavior under constant current is studied in a simple case using the same cell described in section 3.2.1 using chronopotentiometry. Then, actual electrospray systems are studied under approximately constant current conditions. Although electrosprays may take on many distinct geometries, the focus here is on two particular cases. The first is an externally wetted solid needle electrospray emitter. This configuration is useful for testing new RTILs, new emitter materials, new distal electrodes, and such components in a relatively simple system. The Space Propulsion Laboratory has used similar setups in many previous works [1, 144], and there exist a good amount of prior knowledge and experience in the operation of these systems. In this study, the emitter is fired in two configurations utilizing different distal electrodes - a stainless steel cylinder and a porous carbon electrode. The second case is a full working S-iEPS thruster, the same as was developed for the NASA Game Changing Development Program. This thruster utilizes a 480-tip emitter array and is the first electrospray thruster to be operated in orbit. The potential in this system is applied between an extractor plate with 480 apertures each mated to an emitter tip and a large carbon xerogel electrode. By looking at the charging behavior

in these tests, it is possible to gauge the predictive capabilities of the fundamental properties probed in more simple experiments and models.

5.1 Chronopotentiometry

The method for chronopotentiometry (CP) was described in section 3.2.3. The potentiostat applies a step current across the cell, and the potential at the WE with respect to the QRE is traced over time. As current passes through the system, an excess of ions builds up in the WE. For flat electrodes, ions have immediate access to any portion of the electrode. For a porous electrode however, the first ions can build up in a double layer right at the surface but subsequent ions cannot keep building up at the external surface. There are internal surface areas within the porous structure, and the concentration gradient of excess ions leads to a diffusion of the charge into the pores. The dynamics of potential growth must then reflect both the local growth of the double layer as well as the diffusion into and throughout the pores.

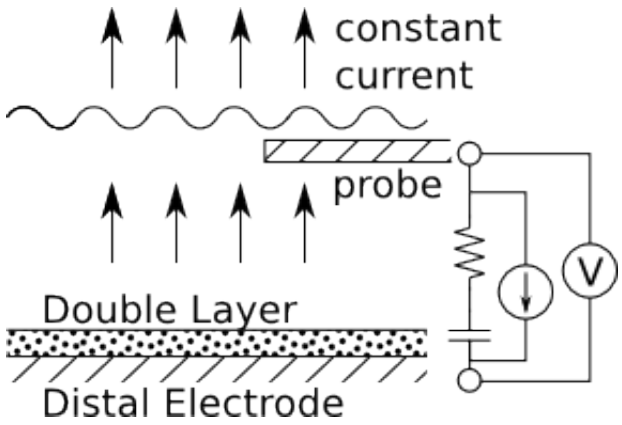

Figure 5-1: Cartoon of porous "distal" electrode and equivalent electrical circuit, neglecting diffusion dynamics.

If the diffusion is fast compared to double layer growth, then the system can be modeled by an equivalent circuit shown in Fig. 5-1. In this case, the potential evolution can be modeled by rearranging Eq. 1.2,

$$dv = \frac{d\sigma_q}{c_d} = \frac{I dt}{c_d} \tag{5.1}$$

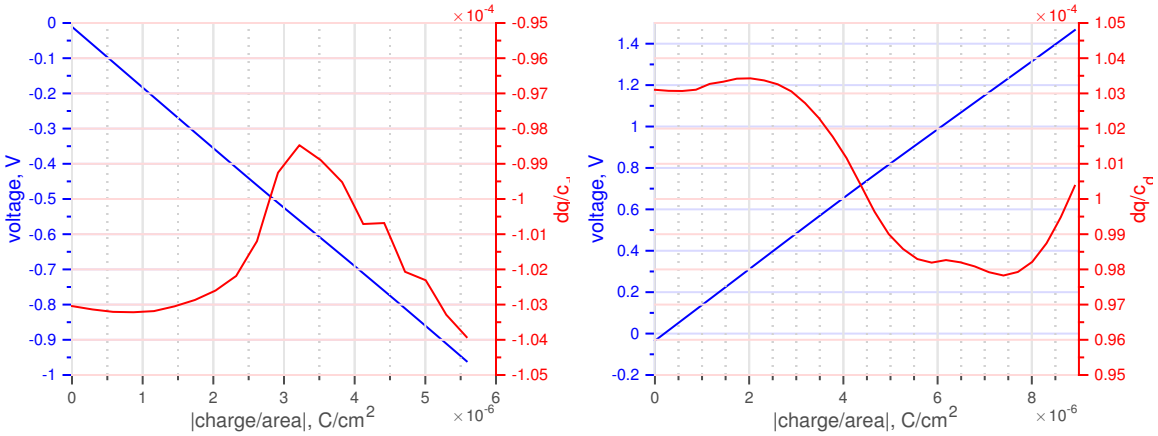

(a) [emim][BF_4] under negative current.

(b) [emim][BF_4] under positive current.

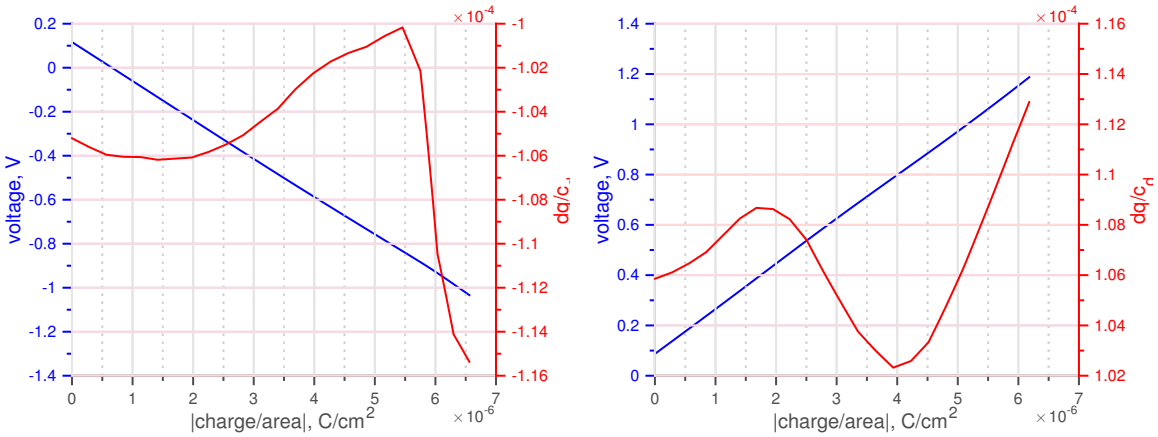

(c) [emim][Tf_2N] under negative current.

(d) [emim][Tf_2N] under positive current.

Figure 5-2: Simulated potential growth governed only by differential capacitance. Diffusion dynamics are neglected, and ions are assumed to have full access to all available surface area.

where for small enough time steps dt, the differential capacitance can be assumed constant at each step and read from the capacitance curves presented in Fig. 4-7 and 4-8. For ideal capacitors of constant capacitance, it is trivial to conclude that the potential growth should be linear under constant current conditions. For the nonconstant capacitance curves obtained for RTILs, the potential no longer can be expected to grow linearly. Fig. 5-2 shows the simulated potential growths under positive and negative current for [emim][BF_4] and [emim][Tf_2N]. Also plotted is dv at each time step; notice that the shape corresponds exactly to the capacitance curves, with the numerical values determined by selected current and available surface area. Instead of plotting potential vs time, the x-axis has been rescaled to show charge/area.

For constant current, this is a linear rescaling; integration of the current to get the double layer charge smooths any noise in the current. This furthermore allows for more meaningful comparison between trials with different current levels, whether by design or by experimental error.

The potential curves look very close to linear. Although the curve is not a perfect line due to the changing capacitance, notice that the difference between the maximum and minimum values of capacitance within the tested voltage range is only 5-15%, depending on RTIL. This means the slope only changes by that amount, Also as the capacitance curve is continuous, the slope changes gradually and do not form sharp corners.

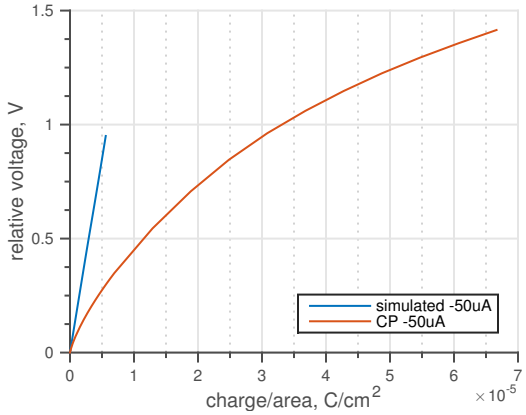

(a) [emim][BF_4] under negative current.

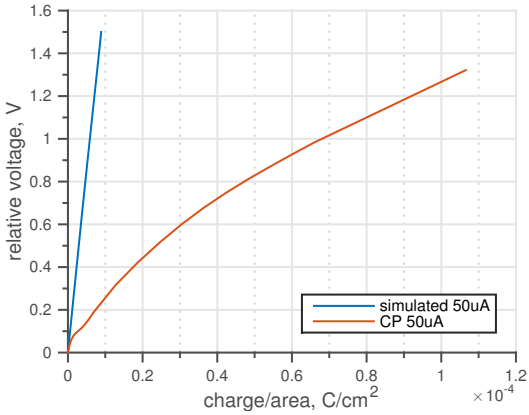

(b) [emim][BF_4] under positive current.

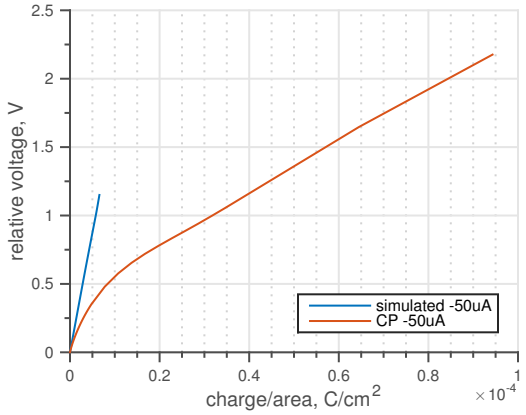

(c) [emim][Tf_2N] under negative current.

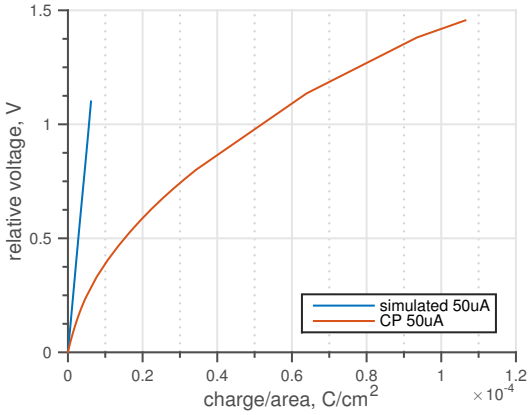

(d) [emim][Tf_2N] under positive current.

Figure 5-3: Comparison of simulated potential growth with no diffusion and voltage evolution in response to CP tests.

The actual data is expected to show slower potential growth than pure RC charging, due to delays in ion transport. As discussed in Appendix B with the chronoamperometry tests, some parts of the dynamical response may be diffusion-limited. The current decay time scale also suggested effects much slower than pure RC charging. This is confirmed by the data, shown side-by-side for each case in Fig. 5-3.

The initial slope of the experimental results is similar to the simulated line, and this is due to there being enough counterions near the electrode surface to create the initial charge inbalance. However, as larger counterion concentrations are required at the surface with the continuing flow of current, the counterion concentration in the vicinity is depleted and must be replenished by diffusion from the bulk. As the concentration profile changes over time, the ion diffusivity within this region may also change. Due to the finite diffusivity introducing a characteristic time larger than the RC time constant, the double layer voltage evolution is slower than the simulated system.

In Fig. 5-4, electrode charging under three current magnitudes are compared. The sharp corners seen in the [emim][Tf_2N] scans are due to the data acquisition automatically adjusting its rate. For all four cases, the initial electrode charging behavior is similar among the different currents. This suggests that if the above hypothesis of a slower transport-imposed characteristic time scale is true, then the proportion of the total current that goes into charging the double layer is similar regardless of current magnitude, at least within the $\pm$50–150 µA range tested.

5.2 Externally-Wetted Solid Emitter

In many electrospray systems, the emitter serves three major purposes: liquid transport from the reservoir to the emission site, amplification of the electric field with its sharp geometry, and creation of the electric field by acting as an electrode. This final purpose was leading to electrochemical degradation, in response to which the distal electrode was implemented [144]. In order for the distal electrode to fulfill its purpose, it is necessary to ensure that all current to balance electrospray emission flows

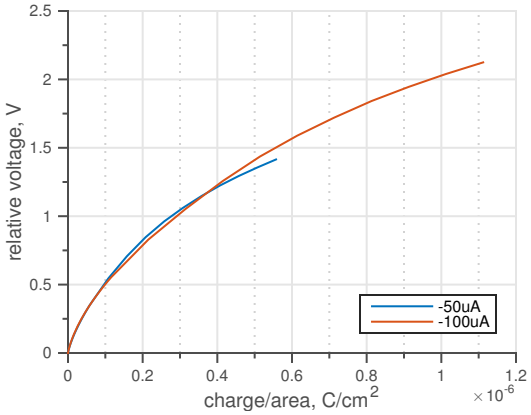

(a) [emim][BF_4] under negative current.

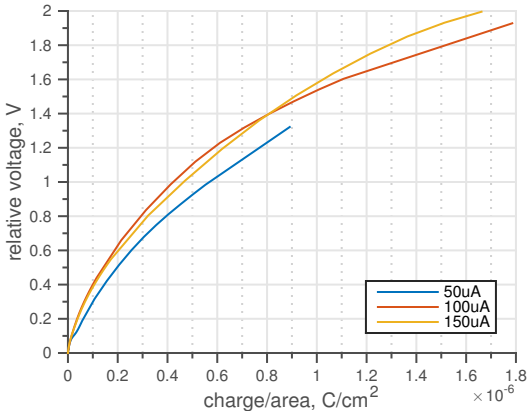

(b) [emim][BF_4] under positive current.

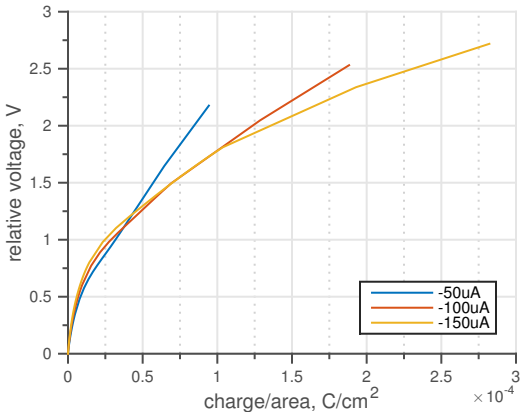

(c) [emim][Tf_2N] under negative current.

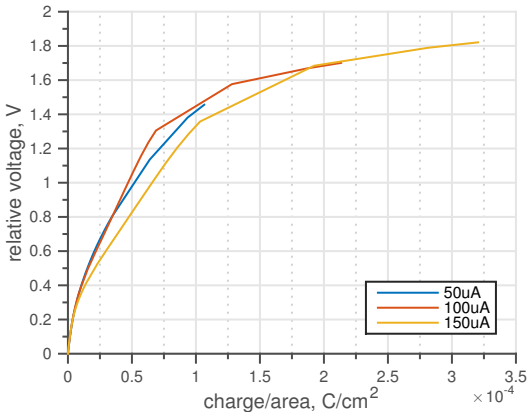

(d) [emim][Tf_2N] under positive current.

Figure 5-4: Comparison of CP electrode charging under different current magnitudes.

through it and not through the emitter. In practical systems this can be ensured by leaving the emitter electrically isolated; however, for purposes of this experiment, the emitter acts as a quasi-reference electrode and must be electrically connected to the electrometer. The electrometer has over 200 TΩ of impedance and is expected to allow for measurement of the probe potential without allowing current flow. In order to check this assumption, the charging behavior of the setup was compared to Brikner's results [144]. Specifically, in order to compare the most similar setups, Brikner's result with a 2 mm separation from tip to distal electrode is plotted along the current setup with 2.54 mm separation in Fig. 5-5. The current setup data presented here is the first 1 s of a 15 s data set (30 s period voltage alternation). The emission currents were set similarly, with Brikner's reported as 60–70 nA and the present setup running

at an average 75 nA. The voltage evolution is very similar, suggesting that the setup is working as expected.

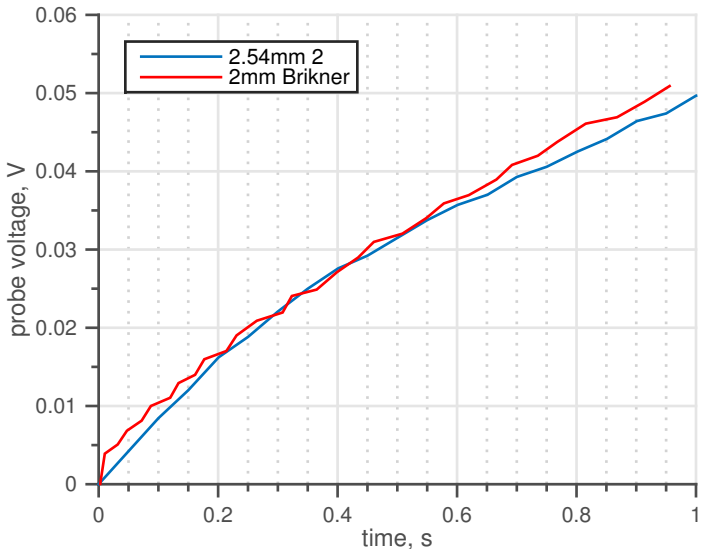

Figure 5-5: Comparison of current setup charging behavior to Brikner results [144].

The potential growth in the double layer is related to the amount of charge in the double layer. With the assumption of no Faradaic reactions at low double layer potentials as before, the excess charge to be adsorbed in the double layer can be obtained by integrating the response current. The physics in this system are different from the previously presented work in that current is no longer flowing between two electrodes connected by RTIL. Rather, the emission of the ion beam in the electrospray draws a current from the RTIL bulk, which must be equalized somehow. The RTIL has two interfaces at which this may occur - the needle surface and the ring electrode surface. The needle is at a floating potential that varies with the RTIL, offset by some approximately constant double layer potential. As such, the amount of charge in this double layer must remain constant, and with no current flowing across this interface, there is zero flux. This leaves the ring electrode surface, which is grounded. This interface also has zero Faradaic current, but the double layer potential is free to vary as the grounded electrode can draw or expel electrons as necessary to balance the charge. This allows a current into the double layer; as this is the only available path for current aside from the ion beam, the double layer charging

current must then be equal in magnitude to the emitted beam current.

The double layer potential and charge are related through capacitance as in Eq. 1.1. The double layer charge q can be obtained by integrating the measured emission current,

$$q + q_0 = \int_0^t I(\tau) d\tau \tag{5.2}$$

where some initial charge q_0 is allowed at time $t = 0$. Using ideal circuit models like that in Fig. 5-1, the double layer capacitor responds instantly. In such case, if the x-axis of Fig. 5-5 is rescaled from time to the double layer charge, then the slope of the plot will represent the inverse of the double layer capacitance,

$$\frac{d\Phi}{dq} = \frac{1}{c_d} \tag{5.3}$$

which is the inverse of Eq. 1.1. The double layer charge here is the total charge distributed across the available surface area of the distal electrode. The voltage on the other hand, as can be seen intuitively from the 1D double layer models presented in Ch. 1, is defined by the ion concentration, or in a per-area description, an effective thickness of the double layer. This is the reason capacitance is often given in per-area terms. In order to make comparisons across different test setups easier, including the RF distal electrode configuration, it is then preferable to further scale the x-axis to charge per area.

In reality, as will be seen in the results presented below, a real electrochemical system's bulk resistance element induces a time delay due to ion transport. This may be ions diffusing through the stagnant diffusion layer [45], double layer diffusion into porous matrices, or some combination thereof. These dynamical effects cause deviation from the ideal RC charging behavior, and will be discussed towards the end of this chapter after the experimental data have been presented.

Although the tests were conducted to simulate a "constant current" condition, the power supply voltage and thus the emitted beam current had some oscillation. There was additional noise due to the MHV cables used to connect the power supply to the vacuum chamber acting as an antenna. In order to negate these effects, particularly

to allow differentiation for an estimation of capacitance, the current and potential data were smoothed. To perform the smoothing operation, the curve-fitting toolbox in MATLAB was used. A weighted least-squares local regression with a second degree polynomial (Loess method [160]) was performed using a span of 10%. For the current, a second "smoothing operation" of simply using the mean value was also tried and used. Fig. 5-6 shows the raw data and the smoothed data; note that the noise has been removed without losing the overall shape of the potential evolution over time. The data presented shows a mean current of about $-120\,\mathrm{nA}$; this was for a targeted $-125\,\mathrm{nA}$ operation. However, due to the rescaling of the x-axis to be the integral of this current, the error in current should not affect the conclusions drawn from this work.

Comparing the two current smoothing methods, it was noted that the desired plot of probe potential evolution as a function of double layer charge did not change significantly. The only distinguishable portion is at the beginning, when the current has not quite reached its full value and the integration overestimates the charge for the mean case as seen in Fig. 5-7. The two methods quickly converge as the integration smoothens the oscillations in the curve processed by the robust Loess method. This example was made with the same data as Fig. 5-6, and similar results were seen with other data sets. Given this similar result, the mean current was used for all axis scalings.

Due to the current levels not being exactly equal in positive and negative polarity, there was a shifting of the overall potential range over time, on the order of $10\,\mathrm{mV}$ per cycle. As discussed above, the exact value of the probe potential is not as interesting as its derivative, which can be related to capacitance. The probe potential is offset by unknown constants, and so in order to make comparisons of the probe potential evolution over time easier, each data set has been shifted to represent "relative voltage," or the potential change from the initial value for each specific firing half-cycle.

Figure 5-8 shows the repeatability of the electrode charging. Each plot shows three trials under the same conditions, with the positive and negative currents run in alternating order for three cycles. In practice, it was seen that the first half-

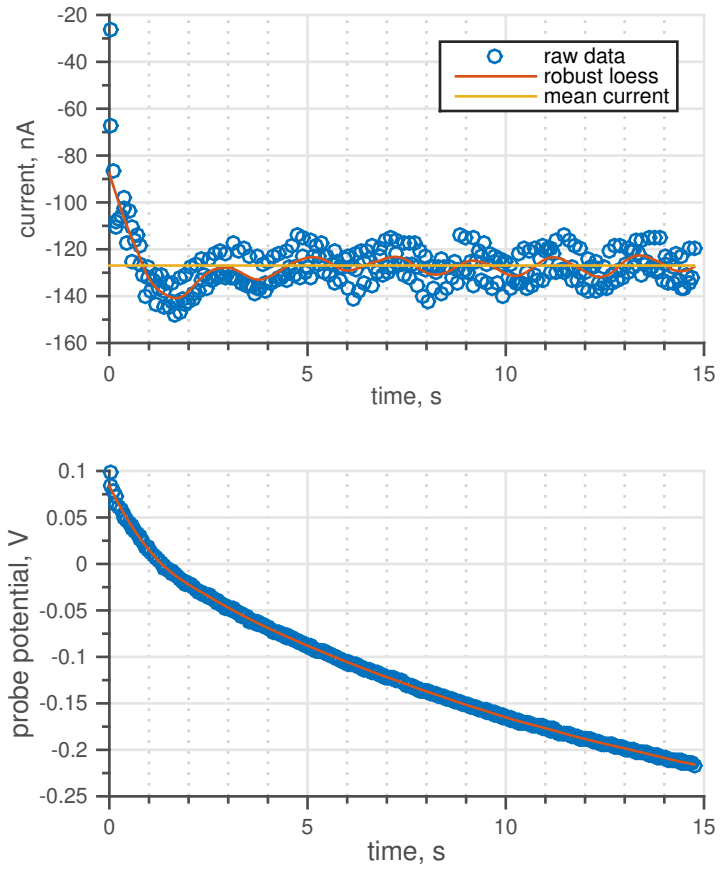

Figure 5-6: Raw and smoothed data for beam current and probe potential. A robust Loess method using a second-degree polynomial was applied to current and potential, and also a simple mean was used for just the current.

cycle of each test produced different shapes which then stabilized into the presented repeating patterns in subsequent cycles. This is believed to be due to the initial voltage V_0 being drastically different - for the first firing, the initial voltage would be open circuit, near zero. For all subsequent cycles, the alternating polarity currents were seen to vary the probe potential between $\approx \pm 0.2\,\mathrm{V}$ for [emim][BF_4] and $\approx -0.25\,\mathrm{V}$ and $0.35\,\mathrm{V}$ for [emim][Tf_2N]. In this cyclical operation, each half-cycle fills the electrode with the appropriate counterion. As the polarity flips, there is an almost instantaneous potential drop corresponding to internal resistance [45], followed by potential "growth" in the opposite sign. This begins as a desorption of the previous counterions (now coions) and after passing PZC, an adsorption of the new counterions.

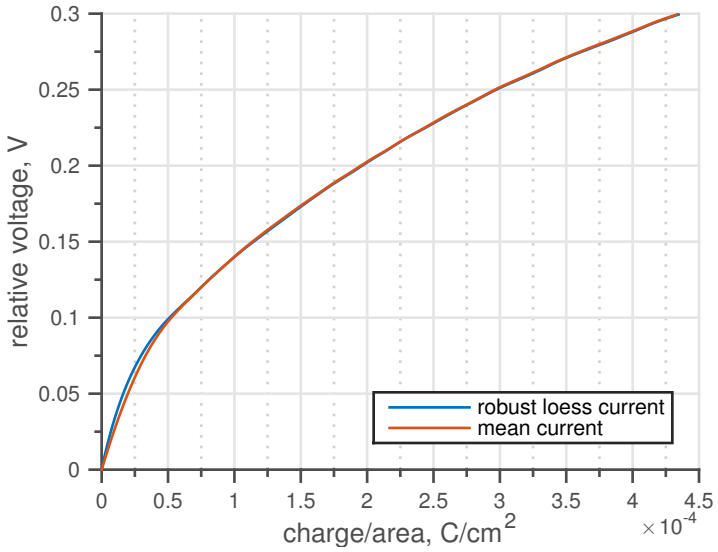

Figure 5-7: Comparison of voltage evolution vs. double layer charge plots using two smoothing schemes.

The first half-cycle in the startup sequence does not have this desorption step, leading to the different potential curve.

In each case, the plot slope is seen to decrease as charge accumulates. Tests for longer firing durations showed this trend to continue, meaning the potential growth continued to slow, seemingly indicating an ever-increasing capacitance. This conflicts with the expectation for capacitance to decrease at larger potentials from theory and experimentally obtained capacitance curves. This is however explained by the dynamics of ion transport. As the counterions cannot immediately get from bulk to double layer, the double layer does not charge as quickly as in an ideal RC system.

The positive and negative currents give different shapes for the same RTIL. For [emim][BF_4], the initial slope is about twice as large in the positive current as it is for negative current. However, the positive case also has a greater overall reduction in the slope, so that the curve is flatter by the end of the 15 s firing duration. Applying the above interpretation with capacitance directly, this suggests that the anion-dominated double layer in the positive emission case has larger capacitance than the cation-dominated negative case. Given the much smaller dimensions of $[BF_4]^-$ compared to $[emim]^+$, this agrees qualitatively with first-order approximations. The difference in

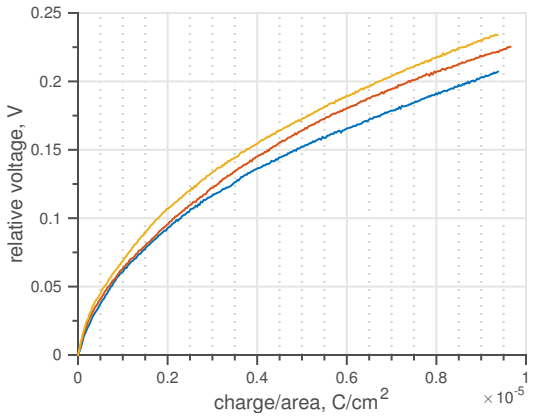

(a) [emim][BF_4] at −115 nA beam current

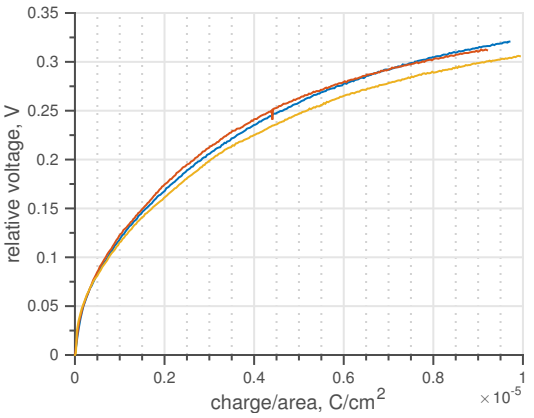

(b) [emim][BF_4] at 115 nA beam current

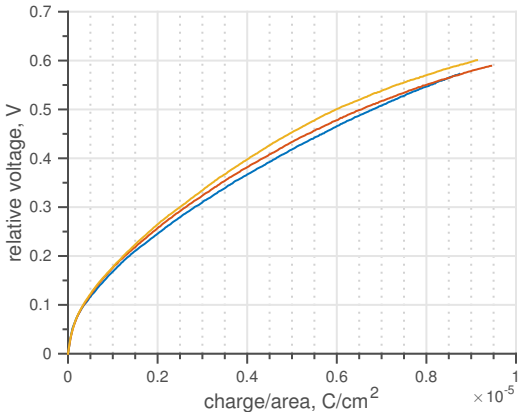

(c) [emim][Tf_2N] at −115 nA beam current

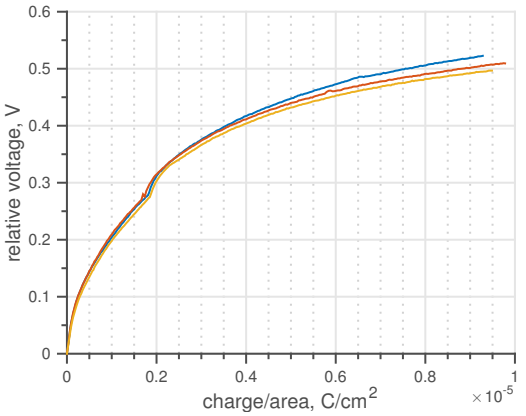

(d) [emim][Tf_2N] at 115 nA beam current

Figure 5-8: Solid needle emitter with SS distal electrode separated by 2.54 mm from the tip was fired with a target current of ±115 nA for durations of 15 s. The relative voltage is $|V(t) - V_0|$ where V_0 is the initial probe potential when each applied voltage step reaches its steady value.

shape is more clear for [emim][Tf_2N], which shows a bump in the positive current. Looking at the actual value of probe potential, this bump begins at approximately 0.13 V. This bump then may be due to the double layer counterion changing from cation to anion (PZC). Referring back to the capacitance curve of Fig. 4-8, there is a slight bump around 0.1 V that may correspond to this feature as well. The final slopes of the positive and negative cases for [emim][Tf_2N] are closer to each other than the [emim][BF_4] data, which in the context of capacitance agrees with the much closer sizes of the constituent ions.

The next comparison is between setups with different needle tip to distal electrode

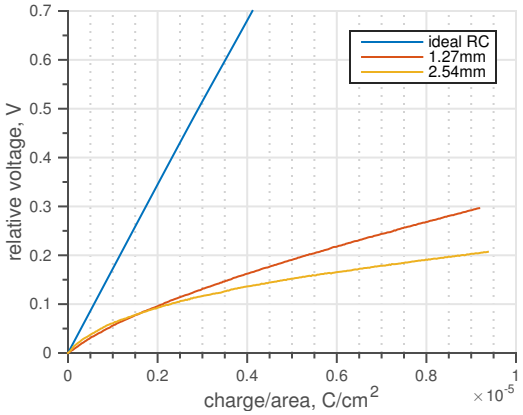

(a) [emim][BF_4] at −115 nA beam current

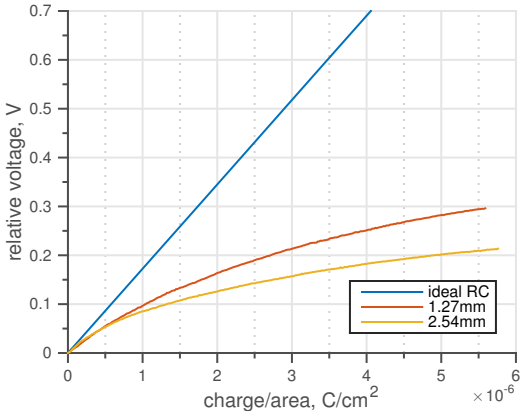

(b) [emim][BF_4] at 75 nA beam current

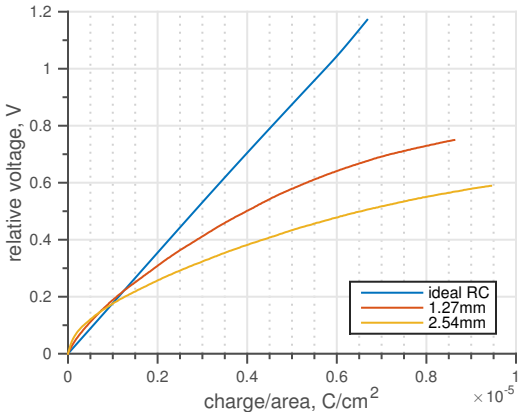

(c) [emim][Tf_2N] at −115 nA beam current

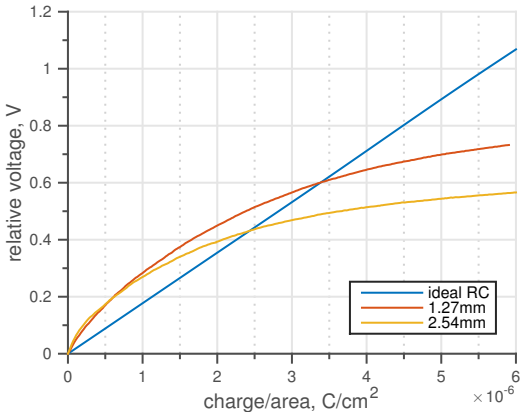

(d) [emim][Tf_2N] at 75 nA beam current

Figure 5-9: Solid needle emitter with SS distal electrode separated by 1.27 mm or 2.54 mm from the tip was fired for durations of 15 s.

separation distances. Fig. 5-9 shows the SS distal electrode needle emitter firing with the two RTILs at two separation distances, 1.27 and 2.54 mm. For clarity, only one line for each separation distance is shown; however, as shown above, each case showed good repeatability and thus the trends revealed here do not differ for other data sets. Also plotted are the ideal *RC* charging behaviors, using capacitance values from a lookup table populated with the curves from Ch. 4, and starting from a V_0 similar to the experimental data sets. For both RTILs in either polarity, the smaller separation distance allows for a larger overall voltage rise at a given charge density (or analogously, time). Also for all four cases, initial behavior is very similar but then diverge after some charging. This divergent behavior suggests that the liquid

path length from the needle tip to the distal electrode is an important factor in the double layer charging dynamics. The most likely culprit is the diffusion time for ion transport from the reservoir at the distal electrode to the emission site at the needle tip. The smaller separation distance does not require as much time for the ions to reach the emission site, and for the counterions to reach the distal electrode surface, thus allowing for faster growth of the double layer, closer to the pure capacitive charging. The initial charging of [emim][Tf_2N] faster than pure capacitive, especially under positive current, can be explained by diffusion of the double layer across the distal electrode surface. Although the SS electrode is not porous, there is still a finite size that is large compared to other characteristic lengths of the experiment. Thus, it is possible that some limited portion of the electrode initially charges, effectively decreasing the area used for scaling the x-axis. This will result in the experimental curves stretching rightward, so that the voltage growth locally is aligned with the simulated curve.

Next, the effect of different emission current values was observed as in Fig. 5-10. For [emim][BF_4], increasing current magnitude was seen to result in an increased overall potential. The higher negative current case shows an initial region of almost constant slope, followed by a sudden decrease in slope to run nearly parallel to the lower current curve. The positive case shows a more gradual divergence. Note that due to the current levels achieved during testing, the magnitudes of the negative and positive cases are not equal. Unlike previous comparisons, [emim][Tf_2N] shows the opposite behavior from that of [emim][BF_4], in that higher current magnitudes led to slower voltage growth. Despite the larger current case providing much larger charge, the total voltage rise over 15 s is about 20% less than that achieved by the lower current levels. It is worth noting that the initial voltage for the higher current case was about 0.1 V higher than in the lower current mode, with the first half-cycle being negative current. Due to the smaller change in voltage for this first half-cycle, the positive half-cycle led to the higher current mode reaching absolute voltage values over 0.1 V higher than in the lower current mode.

In order to observe significant potential rise with the porous distal electrode con-

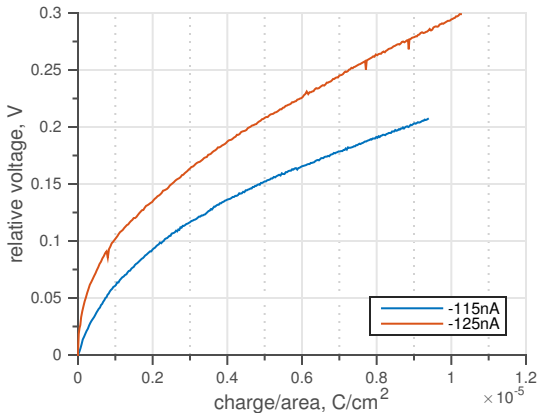

(a) [emim][BF_4] at two negative beam currents

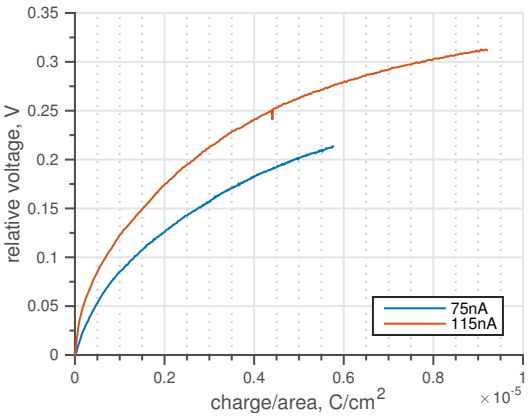

(b) [emim][BF_4] at two positive beam currents

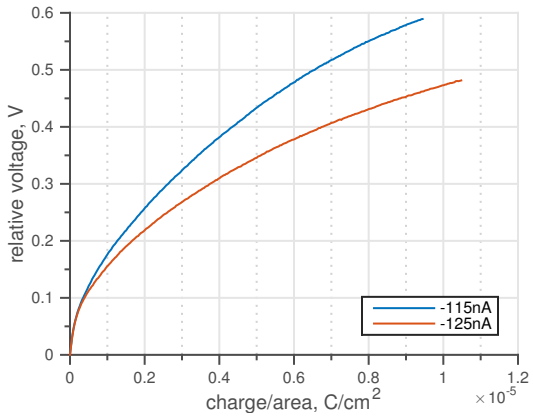

(c) [emim][Tf_2N] at two negative beam currents

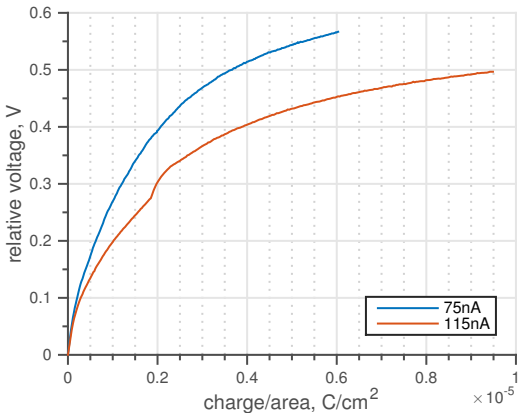

(d) [emim][Tf_2N] at two positive beam currents

Figure 5-10: Solid needle emitter with SS distal electrode separated by 2.54 mm from the tip was fired for durations of 15 s.

figuration, a much larger firing time was necessary. This is of course the purpose of using the porous electrode, and by comparing the results of this configuration to the earlier data from the SS distal electrode, it is possible to quantify the benefit of the porous electrode. It is possible to estimate how much longer emission must continue in each polarity to observe a similar voltage change by linearly scaling by total surface area. Using the specific surface area estimate from pore size statistics given in Ch. 4, multiplied by the carbon distal electrode mass of 0.0304 g gives a total surface area of 281.8 cm^2. The SS distal electrode had an inner surface area of 0.18 cm^2, so the RF has over 1500 times the surface area. If all of the available surface area were

active, then it can be expected to require emission for over 6.5 h in order to see the same amount of voltage growth. In practice, it was observed that firing for 90 min gave the same order of magnitude voltage change. From porous electrode studies, it has been shown that the double layer does not charge evenly but rather charges preferentially at the pore entrance and diffuses inward. Comparing the amount of time taken to cause a similar change in relative voltage between the RF and SS configurations, it was estimated how much of the RF distal electrode is "active." For example using [emim][BF_4], Fig. 5-10 shows that at -125 nA the SS configuration experienced $\Delta V \approx 0.3$ V in 15 s whereas Fig. 5-11 shows that the RF configuration had the same ΔV in about two thirds of the 90 min, or 3600 s. This gives a time ratio of 240, for an estimated active area fraction $A* = {}^{\text{time ratio}}/_{\text{area ratio}} \approx {}^{240}/_{1500} = 0.16$. Similar estimates for the two RTILs and two polarities give 0.16, 0.91, 0.06, and 0.40 for [emim][BF_4] negative and positive, and [emim][TF_2N] negative and positive, respectively.

Due to the much larger time scale and slower change in potential, the gathered data had significantly more noise than for the SS distal electrode. The current also tended to be less stable, with large oscillations often on the order of 20 nA. As such, the probe voltage and current data were smoothed using the 10% span robust Loess method. Fig. 5-11 shows the smoothed current and probe potential data for [emim][BF_4] in positive and negative current, as well as the relative voltage vs. charge/area plot as presented with the SS distal electrode tests. Fig. 5-12 presents the same plots for [emim][Tf_2N], using the same experimental setup.

Looking at the probe potential evolution, it seems that the current variation tends to get averaged out in most cases and do not correspond to any distinct features except for one case. For the [emim][BF_4] under negative current, the large shift from -120 nA to -200 nA does seem to correspond to the hump seen in the probe voltage, which can also be seen in the relative voltage vs charge/area plot. This current jump occurred despite the applied potential being nearly constant; one possible explanation is the formation of a second emission site near the needle tip, adding to the current emission without requiring a change in applied extraction voltage. Due to the limited number

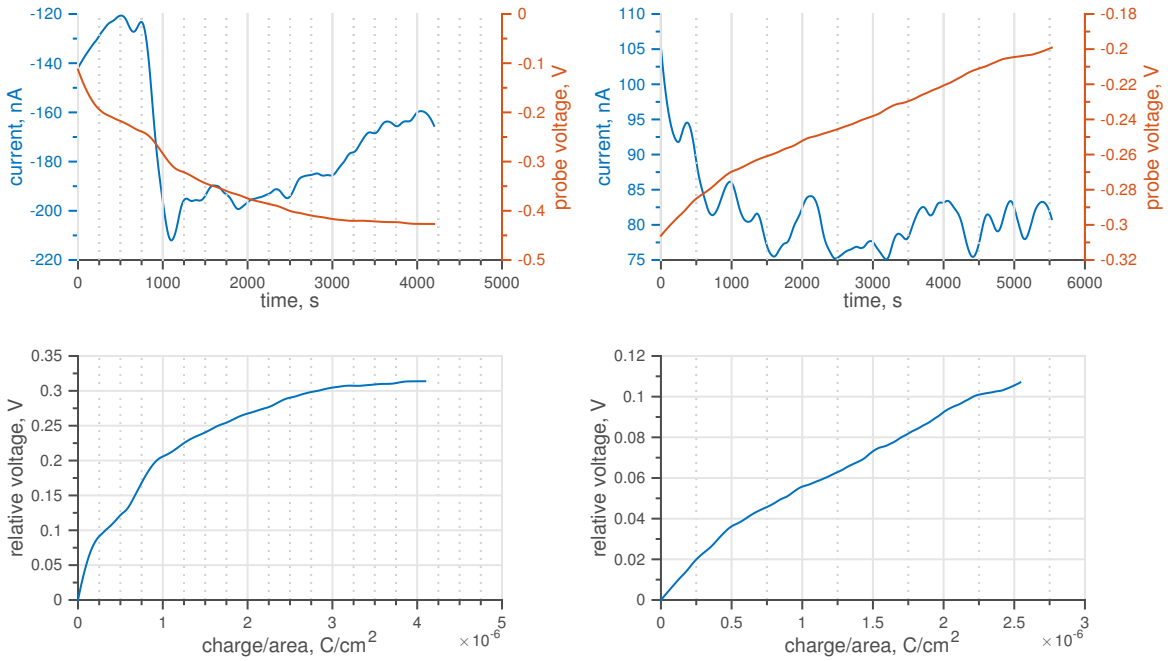

(a) Mean beam current −150 nA

(b) Mean beam current 80 nA

Figure 5-11: Solid needle emitter with RF distal electrode separated by 2.54 mm from the tip was fired with [emim][BF_4] for durations of 90 min. Charge density calculated using total wall area.

of trials that the setup successfully fired consistently for the 90 min duration, this was the best available data set for this set of conditions. The x-scaling for calculating charge/area assumed the entire available wall surface area of the porous matrix was "active," which can be assumed from the time disparity to be inaccurate and will be addressed next.

The results of Ch. 4 show that the porous carbon xerogel electrode behaves, at low frequency ($\sim$ 10 Hz or slower), similar to a flat electrode. Specifically, this means that the variation of capacitance per area with voltage, as shown in Fig. 4-7 and 4-8, remains the same. The RF distal electrode configuration emitter is fired in one polarity for 90 min, meaning its frequency is no higher than 0.19 mHz and well below the threshold separating Warburg behavior and local impedance behavior. If the electrode charging behavior is governed by the double layer capacitance and the dynamics between the emission site and internal face of the distal electrode, then the

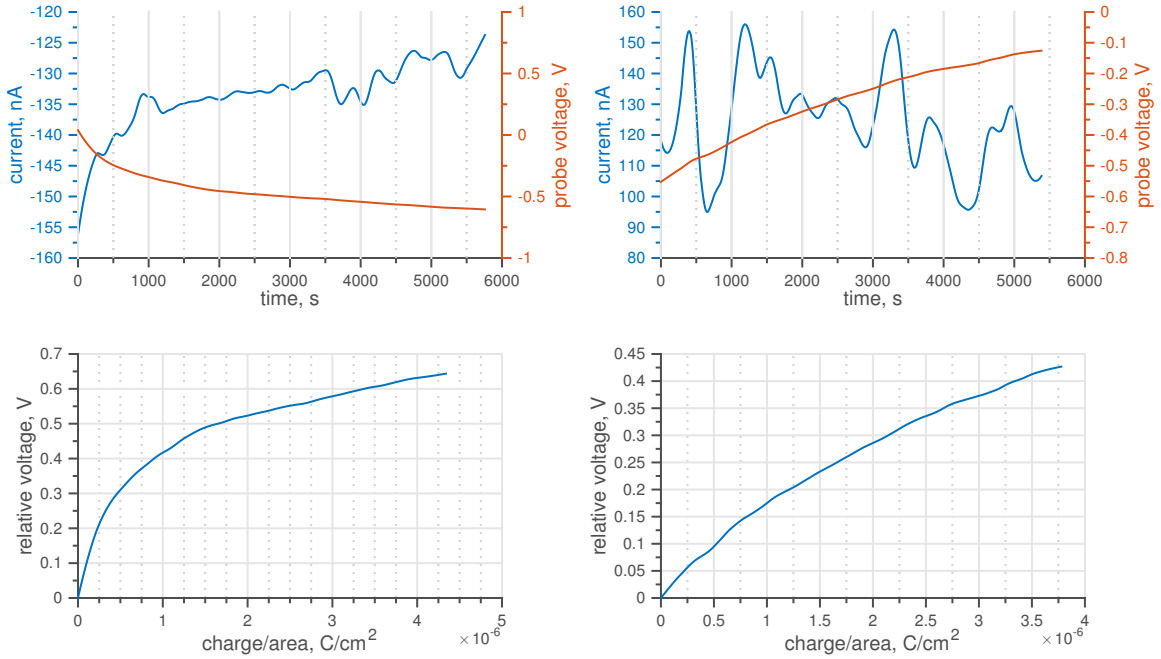

(a) Mean beam current −135 nA

(b) Mean beam current 135 nA

Figure 5-12: Solid needle emitter with RF distal electrode separated by 2.54 mm from the tip was fired with [emim][Tf_2N] for durations of 90 min. Charge density calculated using total wall area.

only factors differentiating the two configurations are current and electrode area and with a properly scaled x-axis the curves should collapse together. The x-axis in the above plots were scaled using the total wall area as calculated from pore statistics. However, by allowing the wall area for the porous case to vary so that the curves for the SS and RF configurations align with each other, it is possible to characterize how much of the available wall area is "active" for each RTIL and beam polarity.

Figure 5-13 shows the voltage evolutions of the two RTILs and two beam current polarities with the limited RF active area. In the label under each plot, $A*$ is the multiplicative factor applied to the total available RF wall area that allowed for the two curves to lie on top of each other, with particular focus in the initial voltage growth. For [emim][BF_4], the positive current curves align closely to each other and the negative current case aligns well until the large hump in the RF data. This hump, as discussed above, was caused by a large shift in current and can be

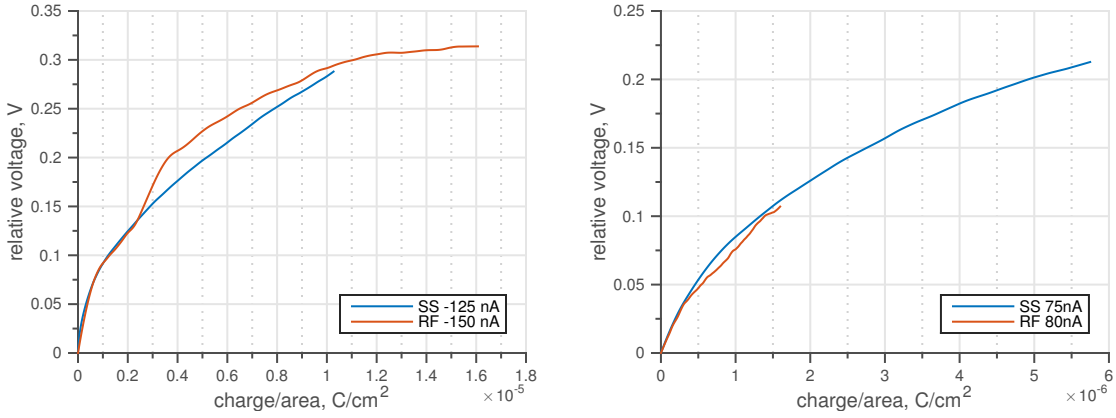

(a) [emim][BF_4], $A* = 0.160$

(b) [emim][BF_4], $A* = 1.000$

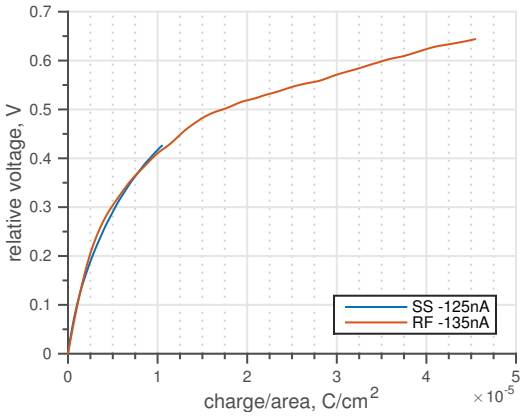

(c) [emim][Tf_2N], $A* = 0.060$

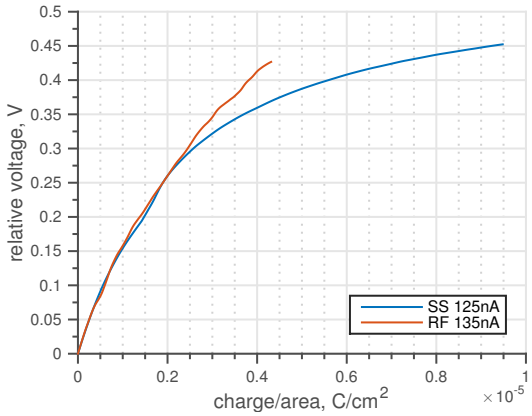

(d) [emim][Tf_2N], $A* = 0.550$

Figure 5-13: Solid needle emitter voltage evolution comparison between SS and RF distal electrodes. $A*$ indicates fitting parameter characterizing the "active" fraction of total wall surface area.

expected to distort subsequent data. The two curves for [emim][Tf_2N] align as well, although the positive case RF does not turn down as sharply as the SS case after $2\,\mu C\,cm^{-2}$. The similar curve shapes confirm the above hypothesis that the charging behavior is governed by the same capacitance curves and macroscopic dynamics, or in other words, the porous electrode behaves as an electrode of much larger surface area without being significantly distorted by diffusion dynamics through the porous matrix. To quantify this assertion, the similarity of the SS and RF curves beyond just the initial slope suggests

$$\tau_{D,bulk} \gg \tau_{D,pore} \tag{5.4}$$

where the bulk diffusion time $\tau_{D,bulk} = \frac{L^2}{D}$ is for salt transport and the pore diffusion time [44] $\tau_{D,pore} = \frac{\lambda_D L^2}{h_p D}$ is for porous electrode double layer charging. The pore "thickness" h_p is on the order of pore size, i.e. $\sim 1 \times 10^{-6}$ m, and the debye length λ_D is on the order of $\sim 1 \times 10^{-10}$ m as given in Tb. 3.1. As Eq. 5.4 is true, the charging dynamics are dominated by bulk diffusion and porous effects are relatively fast.

Using the total wall area and $A*$ values, the actual "active" areas are 45.1, 281.8, 16.9, and 155.0 cm^2, for [emim][BF_4] in negative and positive, and [emim][Tf_2N] in negative and positive beam current, respectively. The negative beam current active area for each RTIL is about one eighth of the positive beam current active area in both liquids. The $A*$ values are quite close to the estimates from the simple time comparison presented above.

5.3 Thruster with Emitter Array

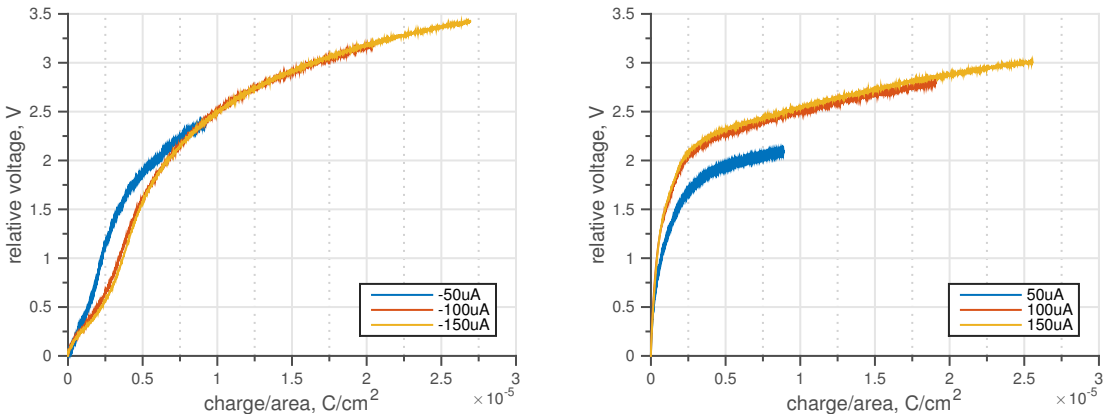

(a) Negative currents (b) Positive currents

Figure 5-14: S-iEPS distal electrode charging measured at three different magnitude currents.

In Fig. 5-14, the S-iEPS thruster array operating at different current levels, $\pm 50, 100, \text{and} 150\,\mu$A are compared. Notice that the shapes of the three curves are very similar for each polarity. This collapsing of curves at different currents was seen in CP, but was not present in the single-needle emitter test. All tests involve

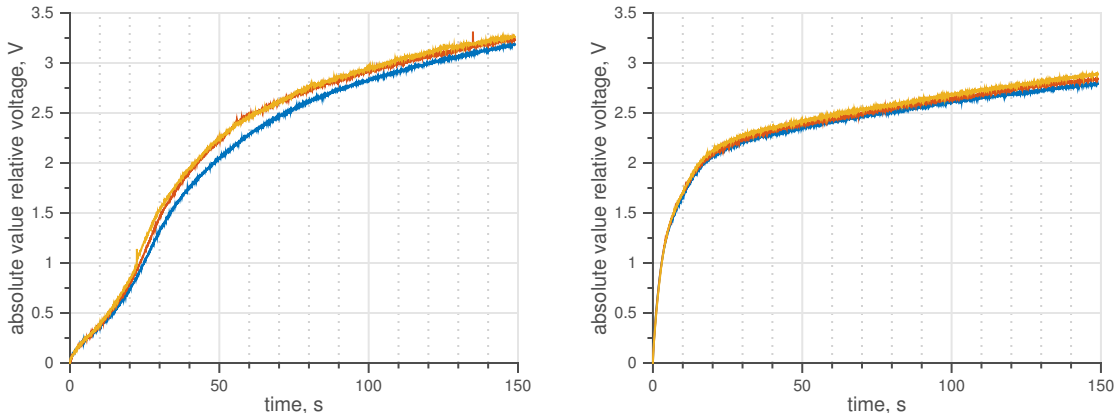

(a) Repeat tests at −100 µA (b) Repeat tests at 100 µA

Figure 5-15: The voltage evolution was very consistent across all cycles in each polarity. This was true at all three tested currents.

an approximately constant current being passed through the WE or distal electrode with a non-participatory platinum wire probe; the commonality between CP and this current test is the current level. In terms of the physics of the entire system, the needle emitter should be closer to this current test compared to CP, as CP does not involve field-emission of ions. However, the needle emitter currents are three orders of magnitude smaller. Another factor to consider is the impedance of the liquid path connecting the current source (CE for CP, emission site for electrosprays) and the WE. For the needle emitter, the RTIL layer coating the needle is on the order of 5 µm thickness, with the length varying from 1.27 to 2.54 mm. For CP, the entire well was filled with RTIL and so the liquid path would have been approximately the frontal area of the WE, 1.14 cm^2, with a length on the order of 100 µm. Determination of the impedance for the S-iEPS setup is more difficult as the liquid passes through a series of porous materials, starting with the distal electrode, then the wick, and finally the glass substrate of the emitter. Once on the far end of the emitter substrate, there is liquid transport through the porous tip as well as along the external walls. The tests also demonstrated excellent consistency across multiple cycles, as shown in Fig. 5-15. Recall that the plotted potential is "relative voltage," set so that the potential at the beginning of the emission half-cycle is zero. The actual potential variation is within ±2 V vs Pt. The voltage range of almost 4 V is then approaching the expected width

of the electrochemical window, given in Tb. 4.1.

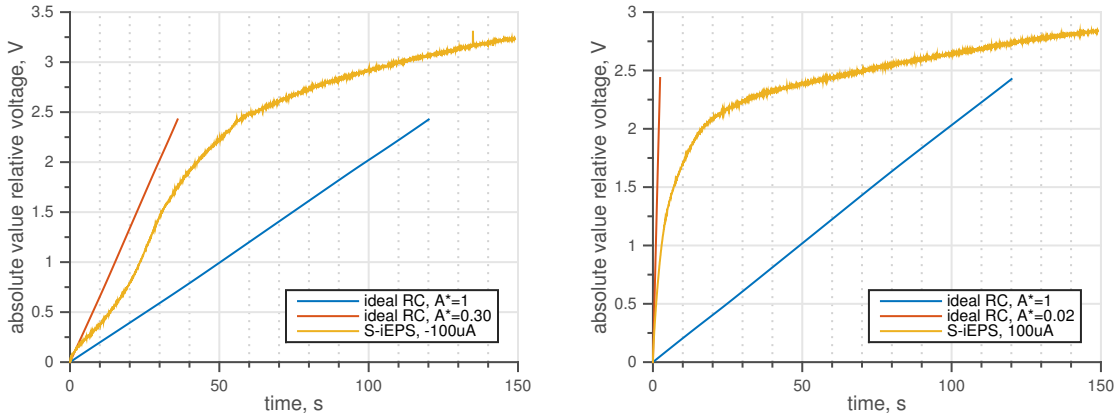

(a) Negative currents (b) Positive currents

Figure 5-16: Comparison of electrode charging under simulated pure capacitive behavior and S-iEPS at ±100 µA. Pure capacitive charging is shown for the cases of total area and a reduced $A*$ value that matches the initial slope.

The S-iEPS electrode charging shown in Fig. 5-14 is faster than the simulated charging at the same current, using only the capacitive behavior as discussed in Ch. 4. This suggests that only a part of the electrode is active, as was the case in the needle emitter with RF distal electrode. Fig. 5-16 shows the charging behavior observed experimentally, bracketed by two ideal capacitive charging curves simulated for the initial active area $A*A_{tot}$ and for total wall area A_{tot}. $A*$ for the limited active area case was selected so that the initial slope is similar to that of the simulation, i.e. the initial charging is purely capacitive.

Comparison of the thruster and CP reveals interesting relations, due to the use of the same electrode at the same current magnitudes. The electrode charging shown in Fig. 5-14 is much faster than their counterparts from CP tests, Fig. 5-4; in fact, the initial charging slope for the CP matched the simulations using the total wall surface area. This reveals an important distinction in the initial charging dynamics of the two experiments, as it relates to the cause-and-effect relationship of double layer growth. As discussed before, the double layer grows in response to electrospray emission as excess charge created at the emission site is transported to the electrode and adsorbs into the double layer. This adsorption process is then governed from

the beginning by diffusion of the double layer into the pores and across the surface. As charge accumulates locally at the interface, electrons are driven into or from the external circuit to accommodate. CP on the other hand forces a current through the external circuit, driving electrons from one porous electrode to the other. In this case, assuming electrons can travel in the electrode much faster than the ions through the bulk, all available wall surfaces of the electrode begin to charge simultaneously, and the double layer grows in response to the built up charge on the electrode side. At first, when all pores are filled with neutral bulk electrolyte, the total surface area charges capacitively. However, as more countercharge is drawn into the double layer, the quasineutral bulk in the center of the pores must replenish its ion concentration by mixing with the bulk outside of the porous matrix. This then is governed by the same diffusion dynamics as in the thruster. With this hypothesis, the voltage growth curves may start under different initial behavior but over enough time their slopes should approach similar values. The S-iEPS and CP potential curves are plotted together versus time in Fig. 5-17, and the positive current does seem to show such a trend. The negative current case seems to be taking a longer time than tested to develop completely, but it does not display contradictory behavior.

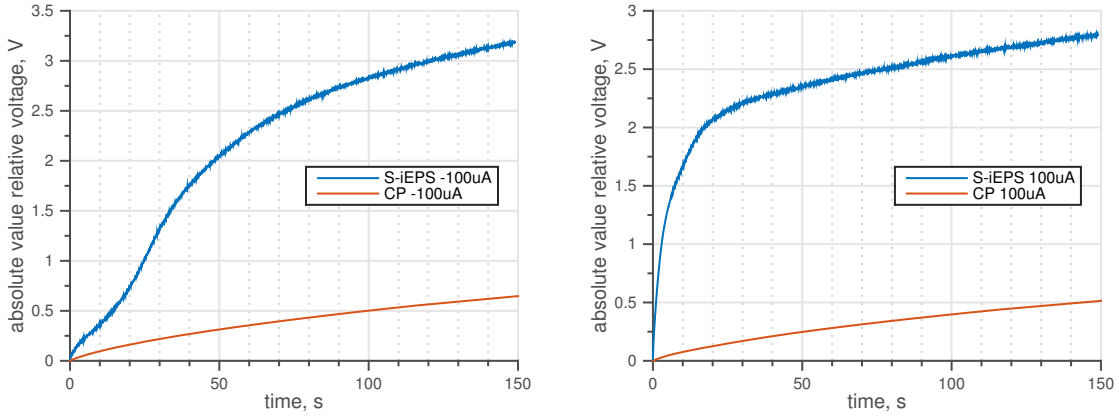

(a) $-100\,\mu A$ (b) $100\,\mu A$

Figure 5-17: S-iEPS and CP charging behavior at $\pm 100\,\mu A$. Although the initial charging dynamics are different, the two curves approach a similar slope as diffusion dynamics become dominant.

5.4 Double Layer Charging Dynamics

As discussed in the preceding sections, the electrode charging dynamics are governed not only by capacitive charging but also by ion transport dynamics. RTILs are concentrated electrolytes with high viscosity [18, 161], which indicates ion transport may be slow. In general, ion transport is considered in three mechanisms: convection due to bulk fluid flow, diffusion due to concentration gradients, and migration due to interactions with electric field. None of the experiments included stirring of the RTIL, so the bulk is not expected to have significant convection. Also, due to electric field screening and resulting quasineutrality, migration is expected to only be important in the EDL. This leaves diffusion as the primary candidate for consideration.

To qualitatively determine how well a simple diffusion model could capture the charging behavior of electrosprays, a simple one dimensional diffusion scaling model was formulated. Using scaling from Fick's second law,

$$\frac{\partial c}{\partial t} = D\frac{\partial^2 c}{\partial x^2} \rightarrow \frac{\Delta c}{t} \sim D\frac{\Delta c}{\delta_D^2} \tag{5.5}$$

which gives the diffusion length scale $\delta_D = \sqrt{Dt}$. Using a similar scaling for Fick's first law and the definition of electric current as the product of electric charge and flux,

$$I \sim zFA\left(D\frac{\Delta c}{\delta_D}\right) = zFA\Delta c\sqrt{\frac{D}{t}} \tag{5.6}$$

where the terms in parentheses is flux. Rearranging and relating concentration to potential by the scaling $\Phi \sim \Delta c F \delta \frac{1}{C}$ where δ includes geometric factors with dimension of m and C is capacitance gives

$$\Phi(t) = \frac{I\delta}{AC}\sqrt{\frac{t}{D}} \tag{5.7}$$

where D can be estimated as the ambipolar diffusivity calculated in Appendix B. This model is not meant to capture exact quantities, as the relations are based on scaling and geometric factors are unaccounted for. Fig. 5-18 shows the SS configuration

needle emitter charging with [emim][BF_4] at $-115\,\mathrm{nA}$ plotted against the diffusion model where a constant capacitance $C = 5.8\,\mu\mathrm{F\,cm^{-2}}$ and $\delta = 7 \times 10^{-13}\,\mathrm{m}$ were used. The broad similarities in the curves suggests that diffusion is a good candidate to explain the dynamics.

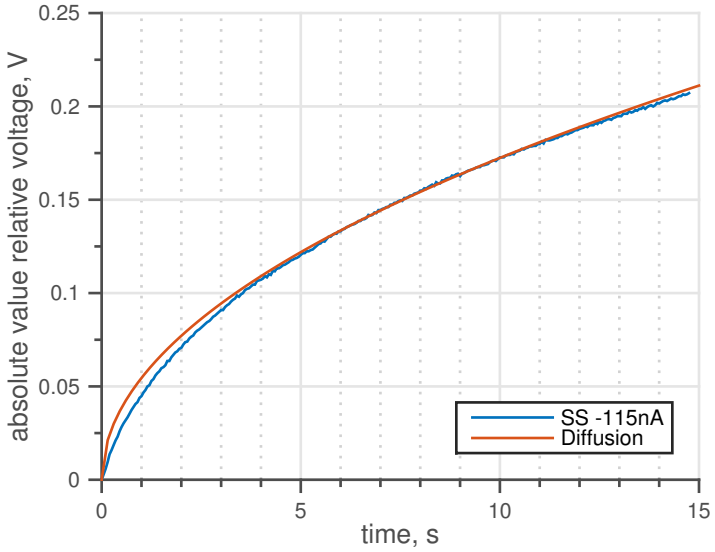

Figure 5-18: Comparison of voltage evolution between 1D galvanostatic diffusion and SS emitter result with [emim][BF_4] at 115 nA.

Diffusion has been discussed in analysis of both the dynamics experiments and the porous electrode results. However, it is important to note that the traditional notion of diffusion relies on the presence of neutral solvents, i.e. water. Diffusion is the result of concentration gradients, which requires local depletion (or concentration) of ions. As ions move, the opposite charge ion must move as well, so as to retain quasineutrality. The vacancies left in the depleted region must be filled by solvent. This cannot be fulfilled in a fully dissociated RTIL, as a neutral group consisting of a cation-anion pair will be the exact same thing that moved away to create the vacancy. Compressibility of the RTIL may allow some concentration gradients, but another possible interpretation is a low level of dissociation in bulk RTIL [162]. This view has been somewhat controversial [155, 163–166], claiming that the multilayered EDL does not fully screen the field and that there are longer-range effects that must also be considered. Gebbie et al. claim that less than 0.1% of the bulk RTIL is dissociated

and free, while the remaining ions are in a complex network that behaves as a sort of neutral solvent [167]. Some evidence for this was obtained from chronoamperometry tests conducted on the flat electrode electrochemical cell, presented in Appendix B.

Another possible contribution to the slow potential growth is due to steric effects. As the double layer builds up, classical models such as the PNP equations assume point ions which can build up quickly while coions and counterions move past each other effortlessly. However, with RTILs there is no solvent and the transport is much more complex. Jiang et al., using MD and an application of the BSK model, studied the response of a model RTIL to a step current, much like a chronopotentiometry experiment [104]. The Nernst-Planck equation (Eq. 1.14) was modified to account for steric effects to give

$$\frac{\partial c_\pm}{\partial t} - D_\pm \nabla \cdot \left(\nabla c_\pm \pm \frac{e c_\pm}{k_B T} \nabla \Phi + \frac{\gamma c_\pm \nabla (c_+ + c_-)}{1 - \gamma (c_+ + c_-)} \right) = 0 \tag{5.8}$$

and used in conjunction with the fourth-order modified Poisson equation accounting for electrostatic correlations, Eq. 2.3. They found that under certain conditions, the potential drop rises quickly as the first layer of counterions dominates the capacitive behavior, but then as subsequent layers begin to have larger effect the potential evolution slows greatly. They attribute this to "dynamic overscreening," an analogous process to the overscreening in quasi-equilibrium double layers but observed under non-equilibrium charging. Specifically, under a $400\,\mathrm{kA\,cm^{-2}}$ charging current the potential curve rose quickly to about 3 V at a surface charge density of $1 \times 10^{-6}\,\mathrm{C\,cm^{-2}}$, after which the slope decreased by $\approx 80\%$. Although the specific value of potential is expected to change with current due to IR drop, the slope change at some critical charge density is remarkably similar to the data shown in Fig. 5-14 for S-iEPS as well as some of the curves in Fig. 5-13 for the solid needle emitter.

The primary concern with voltage growth is the onset of Faradaic reactions. The S-iEPS voltages are beginning to approach values where electrochemistry is a concern. Needle emitters operating at 100 nA levels have not shown potential values to raise any concern, but the assumption that the needle is completely inert should be further

explored. The needle surface double layer was assumed to be constant as it is effectively floating and no current can flow into or out of it without Faradaic reactions. However, due to the large surface area in contact with the liquid, non-equilibrium effects such as redistribution of the surface charges may be possible. If this causes a potential gradient, then along a long enough surface there could be a potential drop on the order of the electrochemical window. Furthermore, this will introduce greater uncertainty in the measured distal electrode double layer potential. A possible way to study this will be to introduce another electrode into the setup. Using a micro-electrode will reduce uncertainties regarding surface charge density gradients across its surface, and also allow for the needle to be completely isolated.

5.5 Conclusions

This chapter included experimental results on electrode charging for several configurations:

- Porous electrode in an electrochemical cell,
- Externally wetted solid emitter with flat distal electrode,
- Externally wetted solid emitter with porous distal electrode,
- 480-tip porous emitter array with porous distal electrode.

Between the single emitter and emitter array, electrode charging at current differences of three orders of magnitude could be studied.

Charging behavior was seen to be fairly repeatable and consistent, including comparisons to independent tests from other researchers in the group. The charging curves changed not just with the selected RTIL but also with polarity - this can be explained by the active ion species. Despite the two tested liquids sharing the same $[emim]^+$ cation, the corresponding charging curves were not the same. This can be explained by the overall liquid properties being different due to the anion. Also, a larger distance from the emission site (i.e. needle tip) to the reservoir and probe gave

rise to slower voltage growth. Although the distal electrode itself is not porous in this case, there is another diffusion timescale imposed by ion transport from the bulk to the emission site.

Changing current levels with the solid needle emitter led to opposite behaviors between the two tested RTILs. This is further complicated by the results from the thruster array, which showed no significant differences in charging at larger differences in current. Although no clear explanation for the different behavior at the needle emitter has been found, it may be that for the much larger currents in the S-iEPS test, any differences effected by changes in current had saturated and other dynamics were dominant.

Combined with the findings of the porous electrode's local behavior in Ch. 4, it is confirmed that the charging behavior of porous electrodes and flat electrodes are effectively the same, and scaled by an active electrode surface area. This active area is a fraction of the total available surface area in the porous matrix which varies with RTIL, polarity, and time. Beyond the initial capacitive charging behavior, the electrode charging slows down as diffusional expansion of the double layer allows for increased accommodation of surface charge without build-up of the double layer potential. Future work should further analyze this behavior, both experimentally and with improving numerical methods, in order to develop tools for proper sizing of electrodes in future designs.

With the data obtained in this thesis, it is possible to give some guidelines for electrode design. For practical thrusters, current will be in the 100 µA range or larger to generate useful thrust. In such cases, the current-dependent dynamics seem to be negligible. Transport dynamics will then be controlled via geometric choices.

A guideline for voltage alternation frequency can be obtained from Fig. 5-16. Although the simulated capacitive charging curve was limited by the potential range of the capacitance curves, extrapolating to where it crosses the experimental data curve gives the time at which the double layer has diffused across the entire surface. Based on the data obtained in this work, the potential range will then cover a total of less than 3.5 V which allows some margin from the electrochemical window.

Summarizing the recommendations then,

- Make the cross-sectional area of the porous electrode as large as possible. The volume of the electrode determines the total surface area, but transport will be improved by having more of the area closer to the pore entrance.
- For a given voltage alternation frequency, use a volume of electrode that can handle all of the excess charge generated at the operating current. For the electrode described in this work for S-iEPS, that gives a maximum half-cycle duration of 140–160 s.

Chapter 6

Conclusions

Electrospray propulsion technology represents an exciting path forward in efficient, versatile micropropulsion for spacecraft. With the demonstration of the S-iEPS thrusters and more recently the flight of ionic liquid-propelled colloid micro-Newton thrusters with the LISA Pathfinder mission [4–6], electrosprays are approaching technology readiness levels where durability and reliability become important factors. Electric propulsion devices are designed to take advantage of their high specific impulse, with operating times as high as 40 000 h for the ion thruster system of the JAXA Hayabusa spacecraft [168].

For the S-iEPS thrusters based on ionic liquid ion sources, a major factor in determining thruster life was observed to be electrochemistry. Electrochemial reactions cause several issues in thruster operation, including propellant contamination leading to polydispersive efficiency loss, inefficiency in electrical power use due to energy going into the redox reactions, and electrochemical degradation of the emitter or distal electrode. Voltage alternation had proven to be an effective countermeasure for preventing electrochemistry, but the frequency of alternation was decided by trial-and-error. In this thesis work, a series of experiments were conducted to better understand the fundamental nature of electrochemistry in room temperature ionic liquids and to observe how this knowledge could be applied to understanding electrode charging in practical electrospray systems.

Electrochemistry in RTILs is a relatively new topic in itself, with researchers from

various fields interested in the novel materials for its myriad of unique properties. Continuum models for RTIL double layers are a work in progress, with the latest advancements being incorporation of electrostatic correlation terms in the governing equation and lattice subdivision for ion size asymmetry. These models are beginning to capture qualitative features seen in capacitance curves achieved via experiment or simulation; however, more experimental results for other RTILs are necessary for validation and tuning.

The first part of this work, in Ch. 4, produced capacitance curves for two RTILs which are not available in literature to the author's knowledge. The curves were generated from electrochemical impedance spectroscopy, which has been the standard method for such purposes. EIS is a well-understood technique, but has a major weakness in its slow execution. Due to the millions of possible ion combinations comprising RTILs, potential methods for faster experimental acquisition of capacitance curves were explored. Voltammetry, PITT, and chronoamperometry tests were conducted in voltage ranges within the electrochemical window with the hypothesis that response currents would be governed by double layer capacitance. None of the methods were able to reproduce the capacitance curves obtained by EIS, at least with the current methods of analysis. The two curves generated by EIS are valuable, and are currently being used by collaborators in Professor Bazant's group for tuning new continuum models of RTIL double layers.

Two interesting applications that are actively researching RTILs are electrosprays and supercapacitors. In both technologies, RTILs are used in systems utilizing not perfectly flat electrodes like that used in most electrochemical tests, but rather porous electrodes which have far greater surface areas. Porosity greatly affects electrochemical behavior, as the double layer no longer develops equally at all points on the surface but must instead diffuse throughout the porous structure over time.

It was important to see how the capacitive behavior of one such porous electrode, porous carbon made from a resorcinol-formaldehyde xerogel, might be related to the results obtained on flat electrodes. In the second half of Ch. 4, the impedance of two RTILs at flat and porous electrodes were compared. The diffusive behavior was

captured by a bounded Warburg impedance model at high frequency, as often used for 1D linear diffusion. Furthermore, the impedance due to double layer capacitance was seen at lower frequencies and it was shown that it could be captured by the same fitting parameters as obtained from flat electrodes. This suggests that for pores of this size, the local double layer charging is the same as for a flat electrode.

With capacitance curves for the two leading candidate liquids for electrospray propulsion obtained, and their charging behaviors at porous electrodes understood, it became possible to see how effectively that might model the charging behavior in electrospray systems. First, a simpler test was conducted using chronopotentiometry with the porous electrode. This test effectively replaced the field emission of ions with a potentiostat-controlled current source. This showed that there is a brief initial charging period that is dominated by the double layer capacitance. However, the voltage growth quickly slows relative to simulated pure capacitive behavior based on the flat electrode capacitance curves. The testing method ensures that the same amount of current is still running, and so the current must be divided into other components. Because the voltage does not grow to the electrochemical window, it is unlikely that a large proportion of the current goes into Faradaic reactions. New findings of dissociation reactions of RTIL ion pairs are one possible component of the "missing" current. Slower ion transport dynamics, in particular ion diffusion, accounts for much of the decay in voltage evolution.

Further tests were conducted with single-needle emitters in two configurations, using either a flat or porous distal electrode. The charging dynamics showed decaying voltage growth rate similar to the chronopotentiometry, suggesting similar division of current components. Because the geometry and operating parameters of the system were kept consistent between the two configurations, it can be assumed that ion transport between the emission site and distal electrode are similar. As such, the voltage evolution should be similar per available surface area of distal electrode. The voltage evolution curves were shown to be similar shapes for each RTIL and polarity, supporting this hypothesis. However, it was found that the actual total surface area of the porous electrode was not the appropriate scaling to compare charging dynamics

with the flat electrode - rather, there is a much smaller and time-dependent "active region" of the electrode on the order of 1% that initially charges with similar behavior to the flat electrode. However, the charging of the porous electrode was seen to flatten after some time, with additional current not leading to voltage growth. This indicates that in this regime, further charges are diffusing further into the pores and expanding the charged region, rather than building up more charge in the same initially defined "active" region. At the tested parameters, this stop in voltage growth occurred at potentials smaller than the electrochemical window, and so Faradaic reactions are believed to not yet be occurring significantly. This is supported by the fact that the RTIL did not undergo noticeable changes in color, as is seen when Faradaic reactions take place. A much longer duration test will be required to test this hypothesis.

Tests conducted with the full S-iEPS thruster, an array of 480 individual emitter tips, also suggested a fast-charging "active" region. It is unclear why this happens in the thruster tests but not in the chronopotentiometry; one possibility is the higher impedance against ion transport in electrospray systems compared to the chronopotentiometry test setup. Long duration tests with the thruster also showed a stop in voltage growth after some time, although at a larger voltage closer to the electrochemical window limit. This might be due to the much larger current used in this test as compared to the single-needle emitters. With this view of the charging behavior of porous electrodes in electrospray systems, it can be concluded that the current design of the distal electrode is oversized. It is possible to decrease the size of the electrode until the entirety is "active," without changing the voltage growth behavior. Making the electrode larger allows for more charge to build up, but the potential growth rate is no longer slowed down under the same operating current. Future designs of thruster distal electrodes should balance the weight and volume of larger electrodes against the electronic components required for alternating the current polarity at faster frequencies.

These findings, ranging from fundamental capacitance curves of two RTILs to new insights in electrospray behavior, will help not just future electrospray applications but also supercapacitors and other ionic liquid-based technologies. The knowledge

gained will help design the next generation of electrospray thrusters, both in geometry and operational parameters. In the long term, it is the author's hope that this work contributes to making robust micropropulsion systems that enable small-satellite constellations, space-based gravitational wave detectors, and other, as-of-yet unimagined possibilities in space exploration.

Appendix A

Additional Results from Parallel Plate Experiments

A.1 Other Methods for Obtaining Capacitance

Capacitance is often unable to be measured directly, but instead require fitting to some model. The first attempted method in Ch. 4 was to select an arbitrary frequency, in this case 0.1 Hz, and use Eq. 4.6. Similar methods had been used in literature, although it is not discussed in much detail how their frequencies were selected. This is critical for quantitative analysis, as the calculated value of capacitance changes greatly as shown for three example frequencies, 0.1, 1, and 10 Hz in descending order, in Fig. A-1. This method, regardless of its numerical accuracy, produced consistent results when tested on three data points taken on the same day.

However, repeat tests under the same conditions several weeks later gave qualitatively different results. The three results shown in Fig. A-2 were run using the exact same methods as in Fig. 4-3, and although the positive peak is roughly at the same potential and capacitance, the negative potential side of the curve is significantly increased in capacitance. The measurements were made using the exact same cell and the exact same RTIL using the exact same methodology (the frequency for calculating capacitance was changed to 0.2 Hz due to unstable behavior of the potentiostat at 0.1 Hz), and thus the differences were attributed to environmental factors. The

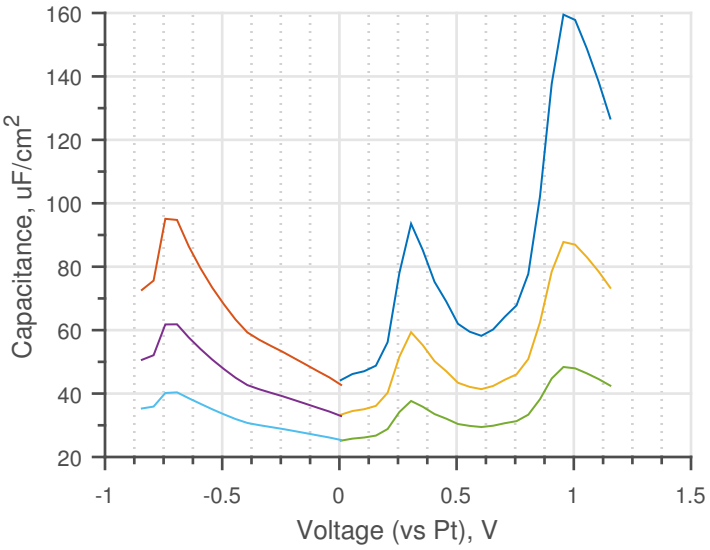

Figure A-1: Capacitance measured with Eq. 4.6 varies significantly with frequency. The same dataset is processed at 0.1, 1, and 10 Hz here, in descending order.

temperature in the laboratory does not vary significantly, but humidity was expected to have changed greatly due to heavy rains in the intervening time.

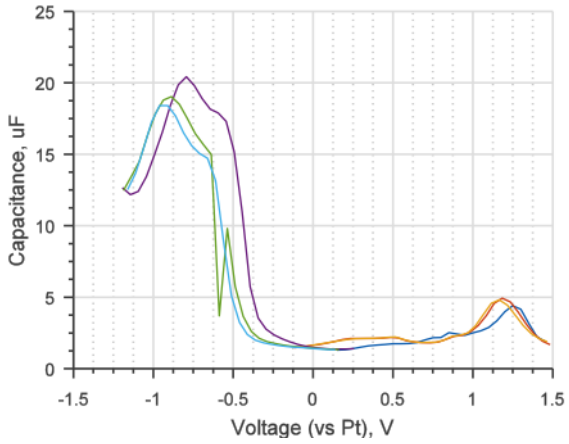

Figure A-2: Capacitance plot calculated with Eq. 4.6 at the arbitrary frequency ω =0.1 Hz on a humid day. The curves changed qualitatively from that taken on a drier day, with the negative peak growing much larger relative to the positive peak.

In order to test this, the exact same test was repeated with one additional step in the RTIL drying phase. A voltage of 1.235 V was applied for 30 min during the pump down sequence in an attempt to electrolyze any remaining traces of water absorbed in the RTIL. Fig. A-3 shows positive peaks that are relatively unchanged,

but a reduction in the negative side by over 5 µF.

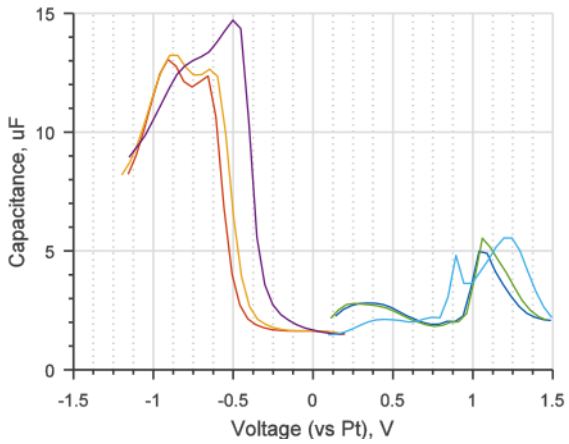

Figure A-3: Capacitance plot calculated with Eq. 4.6 at the arbitrary frequency ω =0.1 Hz on a humid day. Adding the electrolysis step in the preparation led to a slight reduction of the negative peak.

Aside from environmental factors, another issue that needed to be addressed was the arbitrary selection of frequency. In addition to qualitative changes to the curve shape from the lowest to highest frequencies, the magnitude of the calculated capacitance also changed by several orders of magnitude corresponding to the frequency, as can be seen in Eq. 4.6. In an attempt to remove any dependence on frequency, expressions for effective capacitance which depend on equivalent circuit fitting parameters [169] were used. Specifically, for Nyquist plots fitted with a Randles circuit,

$$C_{eff} = Y_0^{\frac{1}{\alpha}} \left(\frac{1}{R_{bulk}} + \frac{1}{R_F} \right)^{\frac{\alpha-1}{\alpha}} \tag{A.1}$$

where R_{bulk} is the Ohmic resistance and R_F is the Faradaic transfer resistance. For the blocking electrode model consisting of a resistor in series with a CPE, R_F goes to infinity and the equation simplifies to

$$C_{eff} = Y_0^{\frac{1}{\alpha}} R_{bulk}^{\frac{1-\alpha}{\alpha}} \tag{A.2}$$

depending only on the CPE and Ohmic resistor parameters.

These effective capacitance curves are shown in Fig. A-4. The locations of the

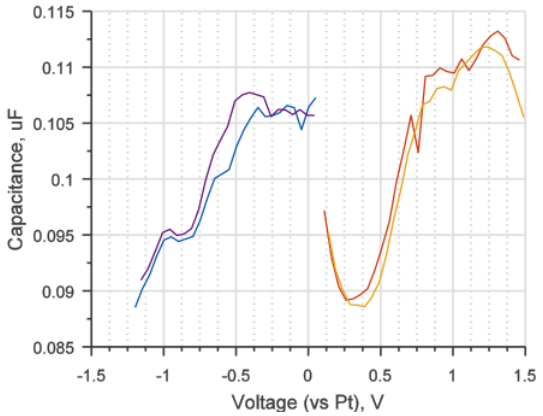

(a) [emim][BF_4] with Randles circuit.

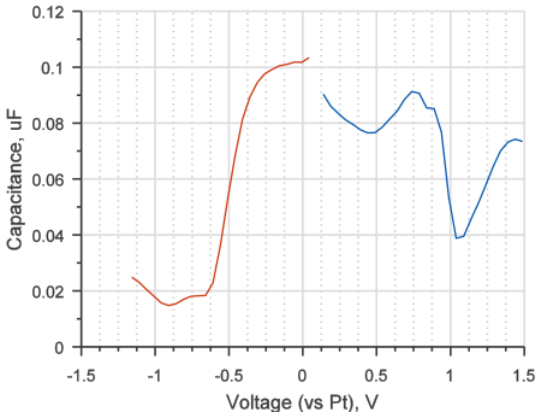

(b) [emim][BF_4] with blocking elecrode.

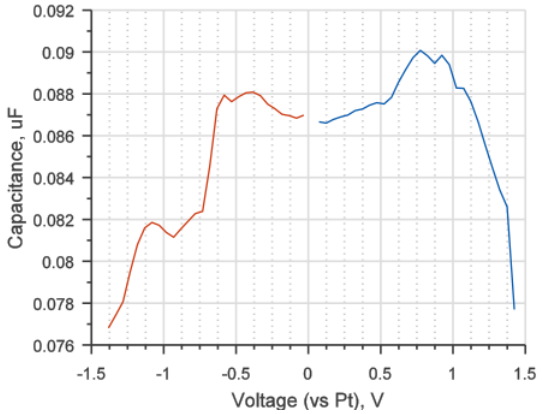

(c) [emim][Tf_2N] with Randles circuit.

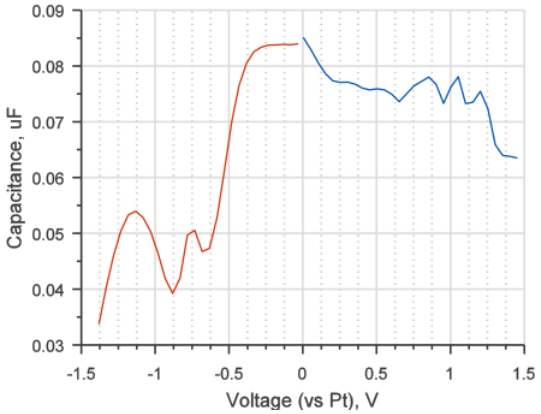

(d) [emim][Tf_2N] with blocking electrode.

Figure A-4: Effective capacitance vs voltage for two RTILs.

peaks generally agree with the previous attempts, but the peaks are wider and thus the central region about the local minimum is thinner. The curve shapes are beginning to resemble those found in literature for RTILs. However, as can be seen by studying the dimensions of the two expressions above, it is difficult to understand how exactly the "effective" capacitance relates to real capacitance. Finally, I settled on the method presented in Ch. 4 as a final method, which was robust for tests conducted on different days and did not suffer from confusions due to dimensionality. The repeatability of the final method are shown in Fig. A-5.

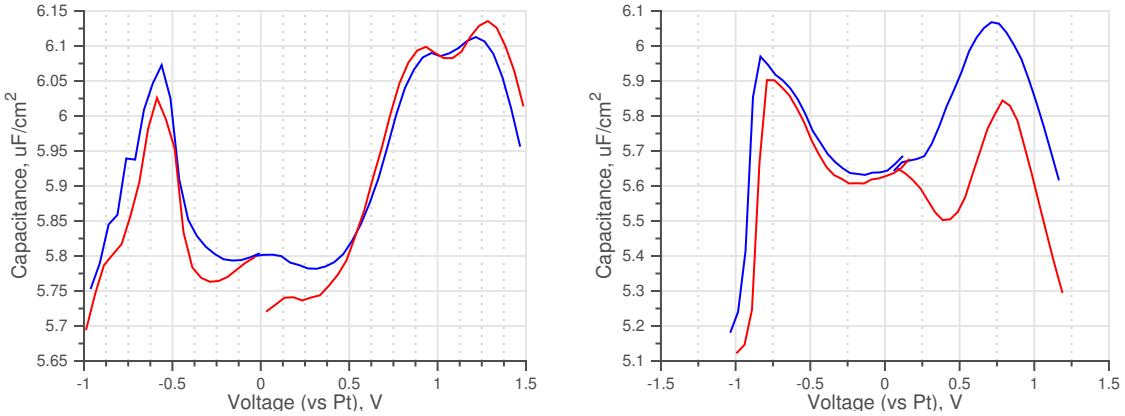

(a) [emim][BF_4] capacitance curves. (b) [emim][Tf_2N] capacitance curves.

Figure A-5: Repeatability of capacitance curves calculated from the 45° intersection frequency.

A.2 Highpass Filter Justification

For the double layer capacitance vs. applied potential plots presented in Fig. 4-7 and 4-8, the capacitance was calculated from the intersection point of the data and the 45° line through the origin. This typically occurred at very high frequencies, as shown in Fig. A-6.

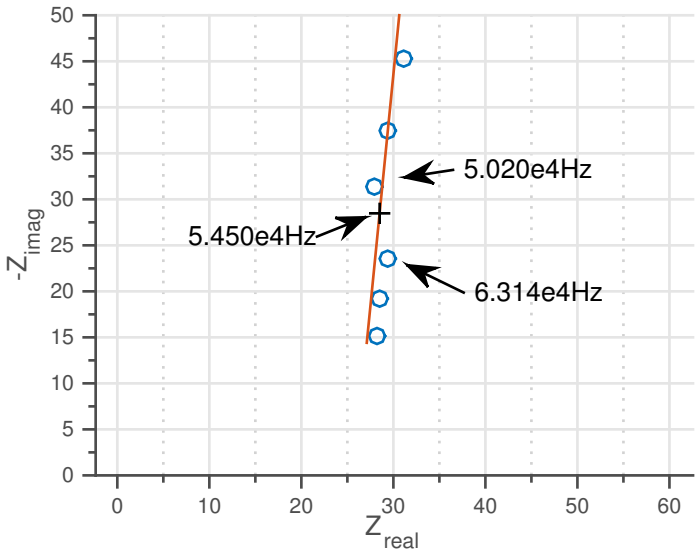

Figure A-6: Frequencies around the 45° intersection point on a representative Nyquist plot.

A high pass filter was applied in the comparison between the parallel plate data

Table A.1: Simulated Randle's circuit electrical element parameters.

Element	R_{bulk}	C_{dl}	R_F	R'	C'
Value	$20\,\Omega$	$25\,\mu F$	$100\,\Omega$	$0.05\,\Omega\,m^{-1}$	$0.5\,\mu F\,m^{-1}$

and the porous electrode data in Ch. 4 as well. The high frequency region of the parallel plate data was fit with an equivalent circuit consisting of a bulk resistance and a CPE, with the threshold frequency being set to 100 Hz, a value much smaller than the RC frequency at the 45° intersection. These two methods are effectively the same, in that they estimate the double layer capacitance by disregarding the lower frequency behavior and using only the high frequency behavior. This section seeks to justify this method.

In order to validate such a method, a test case was conducted with a simulated Randle's circuit. In order to better account for all features seen in the various Nyquist plots, the full circuit included an ideal capacitance in parallel with a series Faradaic resistance and Warburg element, all in series with a bulk resistance. This is a commonly accepted model of double layers in aqueous solvents. The impedance for this circuit was calculated with the parameters shown in Table A.1.

The full Nyquist plot for this test circuit includes a semicircular region accounting for the parallel RC circuit and a low frequency tail at 45° owing to the Warburg element. Fig. A-7 shows a zoomed in view of this Nyquist plot, where data points for frequencies greater than 5 kHz were fitted with a series resistance and CPE. The full frequency range is shown in the inset. Although the fitted range is concentrated in a small region compared to the full Nyquist plot, due to the way the data points are distributed, more than one third of all data points are accounted for. Specifically, 385 of the 1000 data points that were generated were used for the CPE fit, which gave fitting parameters of $Y_0 = 26.156 \times 10^{-6}$ and $\alpha = 0.9958$. As the original circuit element is an ideal capacitance, a perfect result would give $Y_0 = C = 25 \times 10^{-6}$ and $\alpha = 1$; the errors are 4.62% and 0.42%, respectively.

The ability for the high frequency region of the Nyquist plot to allow for an accurate approximation of the capacitive element without consideration of the low

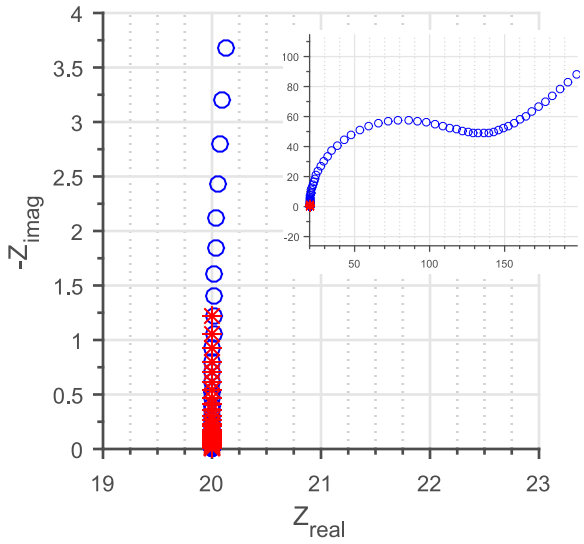

Figure A-7: Simulated Randle's circuit impedance. Red stars were generated by fitting a series resistance and CPE to all data points below 5 kHz. For both datasets, every fifth data point is shown for clarity.

frequency data makes sense qualitatively. Looking at the parallel portion of the circuit, the capacitance acts as an open circuit at low frequency and the behavior then is dominated by the Faradaic reaction branch. At high frequencies, the capacitor becomes a short circuit and current passes much easier through this branch. The threshold frequency is determined by the relative quantities of the various circuit parameters.

Given the ability of similar Randle's circuits to capture the parallel plate experiment behaviors as discussed in Ch. 4 and the widespread acceptance of such circuits in analyzing electrochemical systems, these results are expected to be applicable for the system under study.

Appendix B

Alternative Methods for Measuring Capacitance

Electrochemical impedance spectroscopy was used to obtain capacitance curves for the two RTILs in this thesis. The method is well-established, with examples in literature for both traditional electrolytes and RTILs. However, as described in Ch. 3, it can be a slow test. With the potential for countless distinct RTILs to be synthesized, it is desirable to have faster methods for generating capacitance curves. In this appendix, three such methods are attempted. The methods, namely voltammetry, potentiostatic intermittent titration technique, and chronoamperometry, are all preexisting tests; however, they are generally applied to study Faradaic reactions. In this thesis, the point was to avoid Faradaic reactions and instead study the double layer charging behavior. As such, the tests were applied in a novel manner at potentials well below the electrochemical window. The hope was to produce comparable capacitance curves to those obtained by EIS. However, these transient methods gave qualitatively and quantitatively different results, and thus were not further pursued in the scope of this thesis.

B.1 Voltammetry

Voltammetry is a common electrochemical test which applies a potential ramp and studies the current response. This technique is often used to find the electrochemical window, defined as the range between the oxidation and reduction potentials within which no significant Faradaic reactions occur. The current stays close to zero within the window, rising sharply at the limits upon the onset of reactions. Although close to zero, the current is not exactly zero—there is a small current associated with charging of the double layer at the electrode|electrolyte interface. Assuming no reactions, the double layer acts as a capacitor storing charge. This charging current is the point of interest in this study, as it gives the amount of charge entering the double layer; this is in turn related to the applied potential at that instant through capacitance, as indicated by Eq. 1.1.

B.1.1 Experimental Methods

Voltammetry tests were conducted with the Gamry Reference 3000 potentiostat and the Princeton Applied Research VersaSTAT 3 potentiostat. As with EIS, all voltammetry scans were started from OCV, although in the case of cyclic voltammetry (CV) there is no relaxation period between positive and negative scans. CV applies a sequence of potential ramps at constant sweep rates, selected here as $S = 5$ and $10\,\mathrm{mV\,s^{-1}}$. Starting from OCV, the potential is scanned to the upper limit at $\approx 1.2\,\mathrm{V}$ and then in the opposite direction to the lower limit at $\approx -1\,\mathrm{V}$. These scans are repeated 3 times each to test for hysteresis and repeatability, and ends finally at OCV.

B.1.2 Capacitance Modeling

An ideal linear capacitor has constant capacitance C per area A defined by permittivity $\epsilon_r\epsilon_0$ and separation distance δ,

$$C = \frac{q}{\Phi} = \frac{\epsilon_r\epsilon_0}{\delta}A \tag{B.1}$$

as discussed in Ch. 1. Rearranging and differentiating with respect to time,

$$\frac{d}{dt}C\Phi = C\frac{d\Phi}{dt} = CS = \frac{dq}{dt} = I \tag{B.2}$$

suggests that for constant C and S, a constant current I is the response. Ideal linear capacitance would thus produce rectangular plots of I vs Φ, and any increase in current due to Faradaic reactions would manifest as peaks at their associated potentials. An ideal voltammogram for an electrode with 0.106 µF capacitance at a scan rate of $S = 5\,\mathrm{mV\,s^{-1}}$ is shown in Fig. B-1.

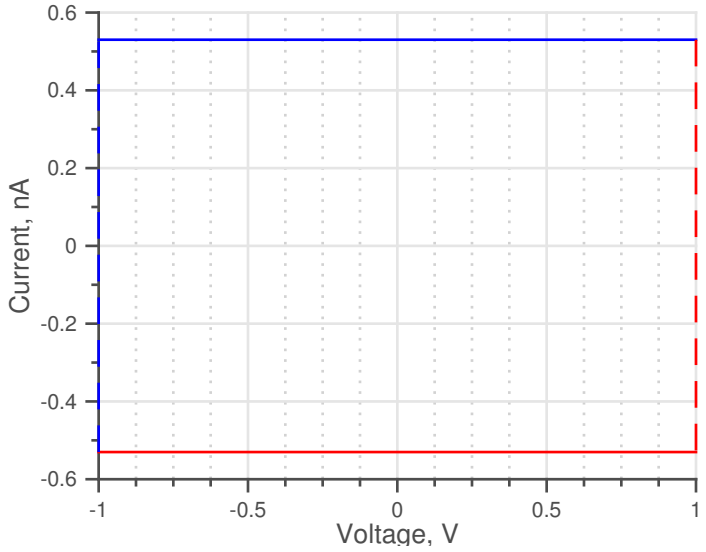

Figure B-1: Ideal cyclic voltammogram for a system with 0.106 µF capacitance at $S = 5\,\mathrm{mV\,s^{-1}}$

.

In an electrochemical system with RTILs, the capacitance is not expected to be constant. However, the dimensions of response current scaled by scan rate $^{I}/_{S}$ are nonetheless consistent with capacitance, specifically $\mathrm{nA\,s\,mV^{-1}}$=µF. One concern is that given the constantly varying potential, if the sweep rate is sufficiently high the double layer structure may not be able to keep up with the applied potential. This may lead to inaccuracies in interpreting the instantaneous current response as the differential capacitance corresponding to the applied instantaneous potential. The first order RC time on the order of 0.1 ms calculated above suggests a fairly quick

response. This effect, if present, should result in the shape of the response changing qualitatively; namely, the curve would shift rightward during the positive scan and leftward during the negative scan. However, data at different sweep rates were compared to each other and showed consistent patterns, suggesting that the sweep rates were sufficiently slow for allowing the double layer development to keep up with the potential.

B.1.3 Data Interpretation

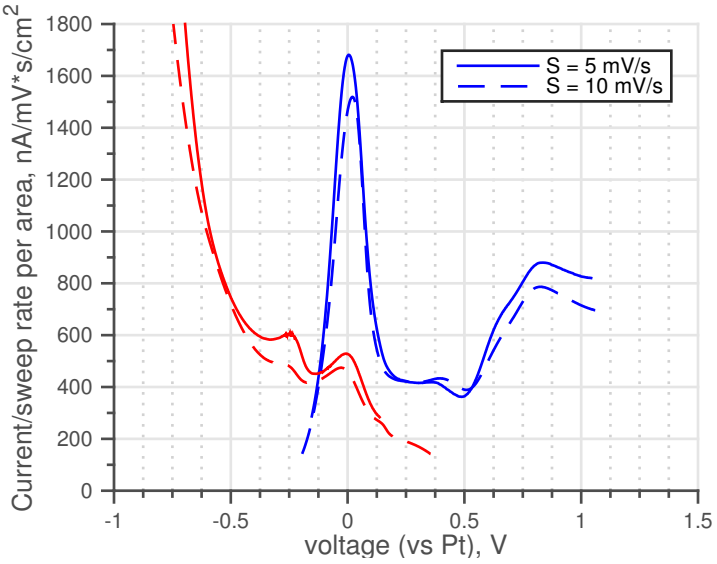

Figure B-2: Cyclic voltammogram for [emim][BF_4] at $S = 5$ and $10\,\mathrm{mV\,s^{-1}}$.

Scaling the response current by the sweep rate was shown to produce consistent results, as shown in Fig. B-2 for [emim][BF_4] and in Fig. B-3 for [emim][Tf_2N]. This suggests that the scan rates were not too fast and that the double layer evolution was able to keep up with the potential scan. The data is scaled by $+S$ in the positive scan and by $-S$ in the negative scan so that all results are shown in the positive plane.

The linear capacitor model presented above gives a rectangular response as shown in Fig. B-1. As the sweep switches from $+S$ to $-S$, the resulting current instantaneously jumps from positive to negative. The model neglected any resistance in the system, and real systems with finite resistance will take a finite time characterized

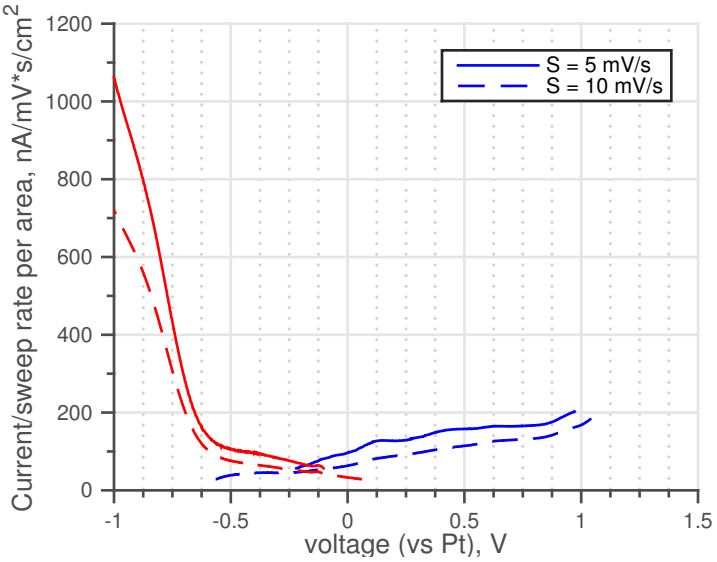

Figure B-3: Cyclic voltammogram for [emim][Tf_2N] at $S = 5$ and $10\,\mathrm{mV\,s^{-1}}$.

by the RC scale to adjust from positive to negative current. This time lag results in data points that show positive current at a negative scan rate or negative current at a positive scan rate - these points would then suggest a negative capacitance, which is clearly nonphysical. Such points have been removed from the plots for clarity. This explains the different potential regions covered by the positive and negative scans.

The [emim][BF_4] result shows a prominent peak in the positive scan at $\Phi = 0\,\mathrm{V}$. This was seen in all cycles at both scan rates, although the magnitude of the peak decreased by about 50% over three cycles. This is a feature not predicted by any capacitance model and also not seen in Fig. 4-7 as given by impedance spectroscopy. The peak is not seen at the same applied voltage during the negative scan, and thus it is believed not to be due to capacitance. There may have been trace reactants that gave rise to a small current; this would explain the decreasing magnitude in subsequent cycles as the reactant concentration decreases. The positive scan also shows a peak at $V \approx 0.8\,\mathrm{V}$. This is close to the location of the positive peak seen in the impedance-generated curve. The negative scan shows slight oscillations between $V = 0$ and -0.25, and then a sharply rising wing. This wing did not peak and start to decrease within the tested potential range, as is expected from theory and impedance results. Finally, the magnitude of the curve is different from the

impedance results. Ignoring the large central peak, the "capacitance" around $\Phi = 0\,\mathrm{V}$ is between 400 and 600 $\mu\mathrm{F\,cm^{-2}}$, which is two orders of magnitude greater than in the impedance-generated curve. Furthermore, the positive peak is $\approx 800\,\mu\mathrm{F\,cm^{-2}}$, so that the capacitance has almost doubled compared to the local minimum. In comparison, the impedance result showed a positive peak only about 5% larger than the central minimum.

The [emim][Tf_2N] result does not show the anomalous peak at $\Phi = 0\,\mathrm{V}$. However, no discernible peak is seen anywhere within the tested potential range, with a slowly rising positive wing and a sharply rising negative wing. The onset of the negative wing rise is very similar to that seen in [emim][BF_4], which makes sense as the cation should be the dominant factor in the double layer behavior at potentials negative of the PZC, seen here to be at $\approx -0.2\,\mathrm{V}$. There is also a slight local minimum in the impedance result at this potential. The CV-generated curve again has a much larger magnitude compared to the impedance-generated curve for this RTIL, at about $50\,\mu\mathrm{F\,cm^{-2}}$ at the minimum. This is an order of magnitude larger than the impedance result.

In conclusion, cyclic voltammetry does not capture the same double layer charging behavior that impedance spectroscopy reveals. Although the dimensionality suggests that the current scaled by sweep rate should give information on the double layer capacitance, the data does not resemble what the best available models lead us to expect for capacitance variation with potential.

B.2 Potentiostatic Intermittent Titration Technique

Potentiostatic Intermittent Titration Technique (PITT) is a sequence of small voltage steps (smaller than thermal voltage $\frac{k_B T}{e}$, where k_B is Boltzmann constant, T is temperature, and e is elementary charge), in which the resulting transient currents are analyzed. It is a common electroanalytical technique for probing the diffusivities of reactants in electrochemical systems, and several analytical models exist relating the transient currents to diffusion coefficients [170, 171]. Within the electrochemical

window however, we can again use this technique to probe the charging current of the double layer. By using small voltage perturbations, we linearize the response and assume each step is governed by an approximately constant capacitance. Then, fitting an exponential decay to the RC response should give us the local value of capacitance at each offset voltage.

B.2.1 Experimental Methods

PITT was conducted using a Gamry Reference 3000 potentiostat. Although the Gamry Framework software does not include PITT as a pre-programmed sequence, it can be made as a series of chronoamperometry steps using small potential steps. As with EIS, all scans were started from OCV with 1 h relaxation before each positive and negative scan. Potential steps were selected as 10 mV, with each step held for 5 s. The step size was selected to be smaller than the thermal voltage of ≈ 25 mV at room temperature. The data acquisition rate must be able to resolve the current decay, expected to behave as an RC circuit following the same argument as before. In such a circuit, the current decays from its initial value of order $I_0 \sim \frac{V_{step}}{R}$ to zero over several RC time scales. The RC time scale as calculated before is on the order of 10 ms, suggesting a minimum data acquisition frequency of 100 Hz, which is the value implemented.

B.2.2 Capacitance Modeling

Within the electrochemical window, assuming no Faradaic reaction current, the entire current response to each step voltage should act to charge the double layer capacitor. This then can be modeled as a simple RC circuit, similar to the ideally polarizable electrode in Fig. 4-1. The current response of this model to a step voltage is

$$I = I_0 e^{-(t-t_0)/RC} + \text{const.} \tag{B.3}$$

where the constant offset is any extra current beyond capacitive charging.

Fig. B-4 shows the current response to several step voltages. The general shape

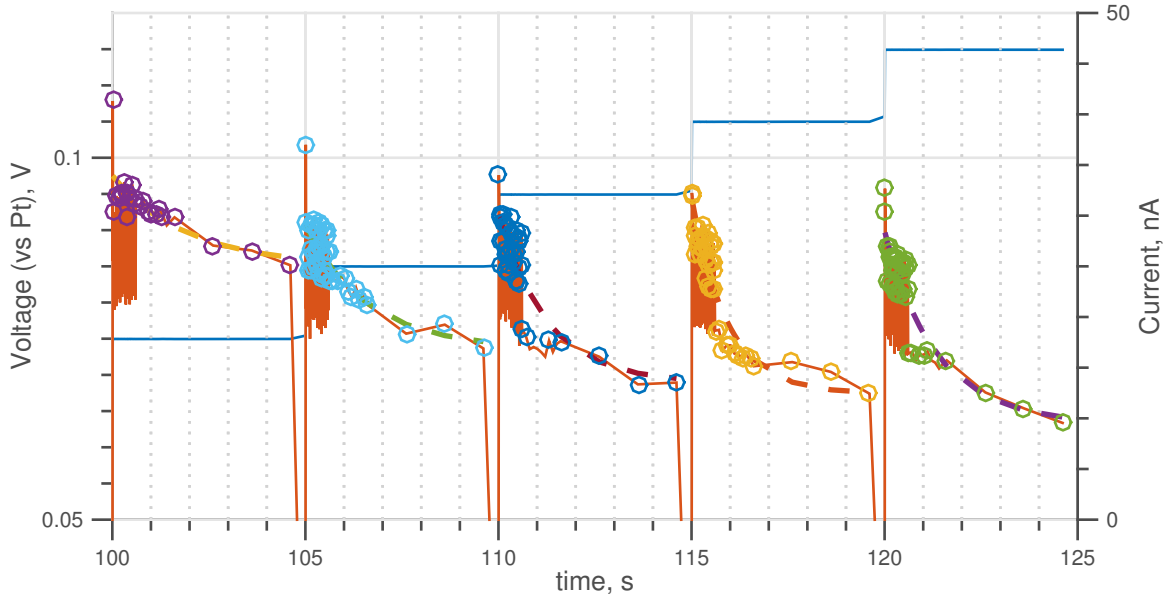

Figure B-4: Voltage steps and current response during PITT experiment. Solid line shows raw data, circles indicate filtered data used for fitting, and dotted line is the exponential fit.

of the curves matches the RC decay well, as indicated by the dotted fit lines. However, there is a nonzero offset current on the order of 10 nA. At small potentials, the offset stays small and can be neglected; however, at larger voltages $\approx \pm 1$ V, the constant offset became significantly larger, ≈ 50 nA. This suggests a larger contribution from processes other than pure RC charging which will need to be included in the model to fully characterize the system response. The impedance test also indicated noncapacitive current, perhaps owing to Faradaic responses to contaminants or dissociation reactions of cation-anion pairs. The offset current seen in PITT may be further evidence of the same anomalous current.

A second method of calculating capacitance from the PITT data exists. Using the definition of capacitance given by Eq. 1.2, we can approximate this at each step as

$$C_d = \frac{\Delta q}{\Delta \Phi} \tag{B.4}$$

where $\Delta\Phi$ is the voltage step of 10 mV and the total charge transferred in each step

can be calculated by integrating the current response over time,

$$\Delta q = \int_{t_0}^{t} I(\tau) d\tau \tag{B.5}$$

In order to apply this method, it is important to isolate the RC charging process from any other contributions to current. As discussed before, any constant offset in Eq. B.3 is inconsistent with RC charging of the double layer capacitor. To properly attempt this method, it will be necessary to understand the cause of this extra current, and to perhaps extend the time allowed at each voltage step so that the two components of current can be properly identified and separated.

B.2.3 Data Fitting

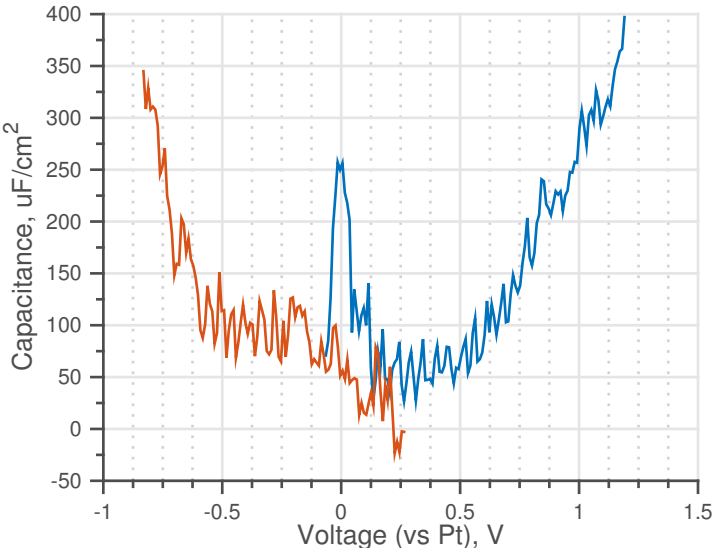

Figure B-5: Capacitance curve for [emim][BF_4] generated by exponential fits onto current responses to small voltage steps.

Figures B-5 and B-6 show the capacitances calculated using the above method for [emim][BF_4] and [emim][Tf_2N], respectively. Similar to the voltammetry results for [emim][BF_4], a large peak is seen in the positive scan at zero polarization, this time for both RTILs. Both liquids show monotonically rising wings, without peaking as expected from theory and as seen in the impedance results. The magnitude is between

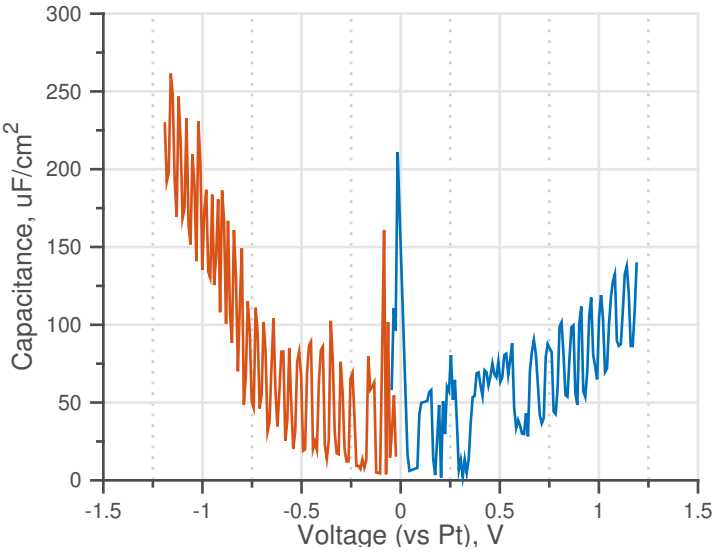

Figure B-6: Capacitance curve for [emim][Tf_2N] generated by exponential fits onto current responses to small voltage steps.

those seen in impedance and voltammetry, and an order of magnitude larger than expected. Furthermore, the capacitance curve is much noisier than in the other tests, with oscillations on the order of 50 µF cm^{-2} which are larger than the signal variation from EIS that this test was intended to recreate. As currently implemented, PITT does not capture the double layer charging behavior as desired. However, it should be noted that PITT is a new method for investigating RTIL double layer capacitance and further improvements may be possible. One way to decrease noise and allow for better exponential curve fitting is to increase the surface area of the electrode, perhaps by using porous materials. The measured currents with this setup were on the order of nA, and this is approaching the lower end of the available resolution on most potentiostats. Although this is not pursued within the scope of this work, the dynamical behavior of porous electrodes discussed in Ch. 4 and Ch. 5 will help with extensions of the model presented above to be made applicable for PITT analysis.

B.3 Chronoamperometry

Chronoamperometry is a technique in which a large step voltage is applied to an electrochemical system and the transient current behavior is observed. Unlike the voltage steps in PITT $\Delta V < \frac{k_B T}{e}$, the chronoamperometry perturbation is $\Delta V \gg \frac{k_B T}{e}$. It is traditionally used to study diffusion-limited redox reactions at an electrode. Diffusion limited current decays according to the Cottrell equation [172],

$$I = \frac{nFA\Delta c_i \sqrt{D_i}}{\sqrt{\pi t}} \tag{B.6}$$

in which n is the number of electrons transferred per molecule and D_i is the diffusivity of the reducible species i. This equation results from the concentration profile given by Fick's second law via Laplace transformation and current density from Fick's first law [28], but has since been derived for particular cases using more intuitive methods based on a Green's function approach as well [173]. Due to the inverse square root relation between current I and time t, plots of I vs $t^{-1/2}$ are known as Cottrell plots. In typical electrochemical systems, Faradaic current decays much slower than double layer charging current and is the object of study. However in the case of RTILs, the bulk electrolyte has significant resistance and Faradaic current would no longer behave strictly according to Cottrell equation [174]. In our case, we select a step voltage larger than thermal voltage but still within the electrochemical window, thereby not allowing Faradaic reactions. We can then ignore Faradaic current and expect that all observed current goes to charging the double layer. Specifically, voltage steps were selected at $\pm 1\,\mathrm{V}$ for both RTILs of study. If the Cottrell plot is linear, it would indicate that the charging current is limited by ion diffusion, and the diffusion characteristics can be calculated from the slope.

As discussed in the PITT section, under small perturbation or for systems with constant capacitance, the charging current is expected to be an exponential instead of $\propto t^{-1/2}$. The characteristic time for exponential decay is given by $\tau = RC$. To see if this behavior may explain the chronoamperometry results, we can make a separate plot of the natural logarithm of current $\ln|I|$ vs time t. A linear capacitance system

will give a constant line with negative slope $^{-1}/_{RC}$.

B.3.1 Data Analysis

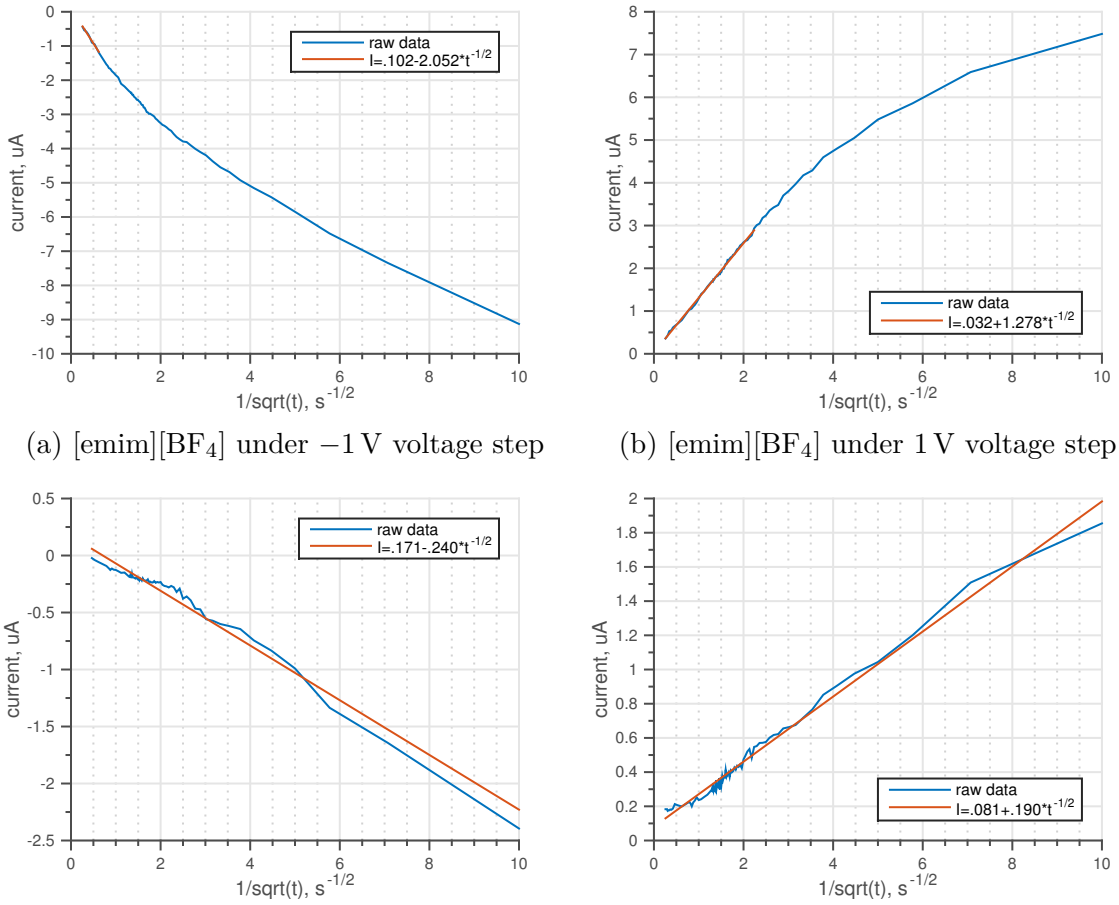

(a) [emim][BF_4] under -1 V voltage step

(b) [emim][BF_4] under 1 V voltage step

(c) [emim][Tf_2N] under -1 V voltage step

(d) [emim][Tf_2N] under 1 V voltage step

Figure B-7: Cottrell plots for [emim][BF_4] and [emim][Tf_2N] under ± 1 V voltage steps. Blue is experimental data, red is fitted values.

The Cottrell plots for the two RTILs under positive and negative voltage steps are shown in Fig. B-7. The curves for [emim][Tf_2N] look quite linear, with slopes of -0.240 and $0.190\,\mu As^{1/2}$. The curves for [emim][BF_4] are not entirely linear. Experiments and simulations of electrolytes with significant bulk resistance exhibit an initial non-Cottrell regime of gradually decreasing current followed by Cottrell behavior in the time domain [175]. As such, linear behavior should materialize on the left side of the Cottrell plot, corresponding to large times. Trying linear regression on $t^{-1/2} <$

Table B.1: Concentration change required to drive observed current via diffusion.

RTIL	ΔV, V	D_{ap}, $\mathrm{m^2\,s^{-1}}$	Δc, $\mathrm{mol\,m^{-3}}$	$\frac{\Delta c}{c_0}$
[emim][BF_4]	+1	2.13×10^{-11}	2.88	4.46×10^{-4}
	-1		4.63	7.15×10^{-4}
[emim][Tf_2N]	+1	1.99×10^{-11}	0.443	1.14×10^{-4}
	-1		0.559	1.44×10^{-4}

$0.75\,\mathrm{s}^{-1/2}$ and $t^{-1/2} < 3\,\mathrm{s}^{-1/2}$ for negative and positive voltage steps, respectively, gives slopes of -2.052 and $1.278\,\mu\mathrm{As}^{1/2}$.

Typically, the concentration term in the Cottrell equation is the bulk concentration of the species under study, $\Delta c_i = c_{i0}$. This is due to the assumption that Faradaic reactions consume all reactants at the surface and so the concentration goes to zero. In the system under present study, Faradaic reactions do not take place and so the surface concentration is not zero. In fact, it is a subject of significant controversy whether significant concentration gradients can even develop in RTILs, where no solvent exists to fill in the remaining space after an ion moves. See the discussion in Ch. 5 on transport dynamics for more details. Here, instead of assigning a value to Δc_i and calculating for diffusivity, it is more useful to assign an estimated value for diffusivity to calculate for the concentration gradient. The estimated diffusivity can be calculated as the ambipolar diffusivity, or the harmonic mean of the cation and anion diffusivities calculated from the Stokes-Einstein relation

$$D_{i,SE} = \frac{k_B T}{3\pi\eta a_i} \tag{B.7}$$

where η is the liquid viscosity. Viscosity values were taken from summarized tables by Zhang, et al. [18], and ion radii values were calculated in Tb. 3.1. The ambipolar diffusivity and resulting concentration changes, both as an absolute value and as a percentage of the bulk concentration, are given in Tb. B.1.

The concentration depletion was less than 0.1% in all cases. This agrees with the abundance of "free ions" estimated by the aforementioned controversial work of Gebbie et al. [167]. In this view, the remaining ions are locked in a net-neutral network, which may act as the neutral solvent to fill spaces and thereby allow for traditional

concepts of diffusion. Using this free ion concentration to estimate conductivity, by relating diffusivity to mobility with Einstein relationship then taking conductivity as the product of mobility, concentration, and Faraday constant $\sigma = \kappa_{free} c_{free} F$, gives $4 \times 10^{-4}\,\mathrm{S\,m^{-1}}$ for [emim][BF_4]. This is four orders of magnitude less than experimental values [18]. A similar magnitude of error using this method was noted in the original Gebbie et al. discussion [162], where kinetic effects were believed to cause the discrepancy.

Continuing with this picture of RTIL behavior, it is then possible to estimate an average capacitance. The ion concentration depletion necessary to drive diffusion in the bulk is balanced by increased ion surface concentration at the electrode, namely inside the double layer. The surface charge density is estimated by the relation

$$\sigma_q = \Delta c F \frac{V_{bulk}}{A_{WE}} \tag{B.8}$$

where V_{bulk} is the volume given by the product of electrode area A_{WE} and the separation distance between WE and CE. This surface charge density is then related via Eq. 1.1 to capacitance, where the potential change has magnitude 1 V. Using the values from Tb. B.1, the resulting capacitances range from 500 to 5000 $\mu\mathrm{F\,cm^{-2}}$. Note that this value is averaged over the entire potential range, and that it also assumes full depletion by the indicated amount across the entire volume. In fact, for the depletion to cause diffusion, there must be some distribution that creates a gradient; thus the calculated values here may be thought of as maximum estimates, perhaps off by a factor on the order of 2. Compared to EIS results presented in Ch. 4, this is over two orders of magnitude too large. However, recent works [176, 177] have noted larger capacitances in DC (or zero-frequency) tests compared to AC methods. In particular Chu et al.'s results from X-ray scattering methods indicated capacitances on the order of 200 $\mu\mathrm{F\,cm^{-2}}$. Note also that the transient methods presented in this Appendix, all zero-frequency methods, also gave capacitances on that order. The reason for this discrepancy is not yet well established; however, these results suggest that the transient methods may be useful with further refinement.

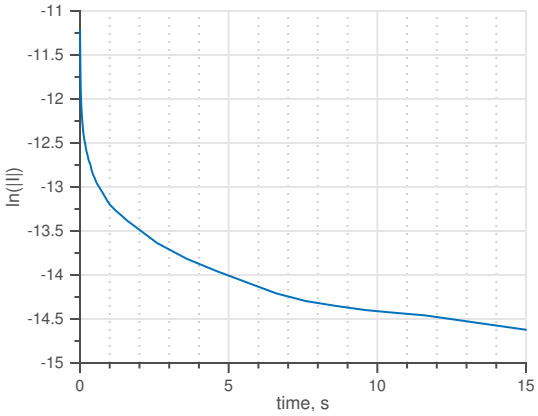

(a) [emim][BF_4] under -1 V voltage step

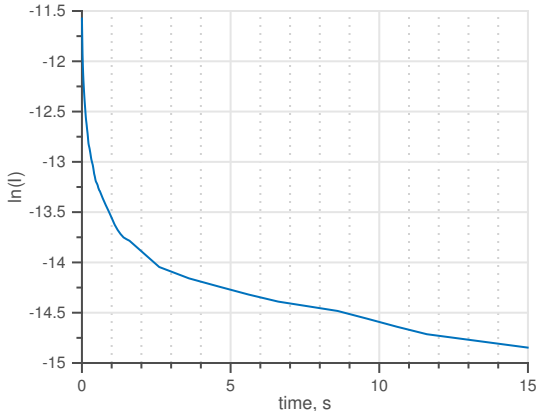

(b) [emim][BF_4] under 1 V voltage step

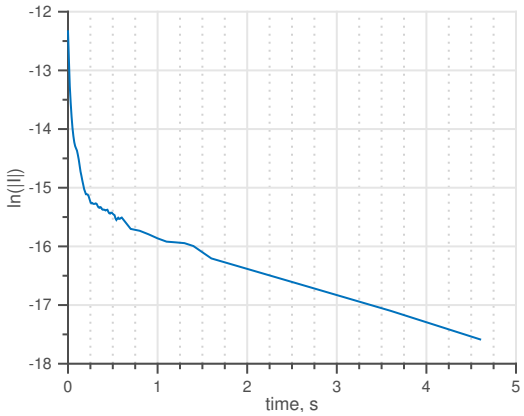

(c) [emim][Tf_2N] under -1 V voltage step

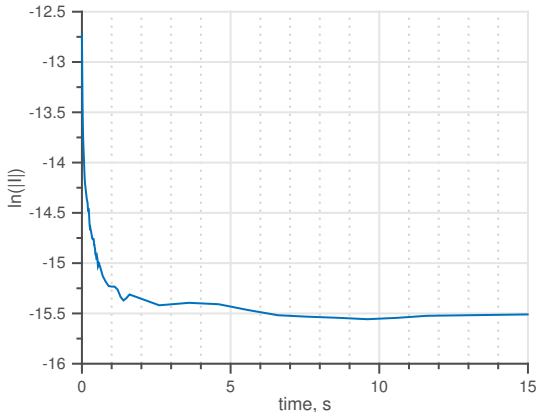

(d) [emim][Tf_2N] under 1 V voltage step

Figure B-8: Chronoamperometry results under ± 1 V step voltage.

The plot of $\ln|I|$ versus t should show a straight line for a system with constant capacitance. We know RTILs do not have constant capacitance; however for the [emim][Tf_2N] results, the tail does seem close to linear. This suggests exponential behavior rather than the inverse square root relation to time tried in the analysis above. Actually using this result to try calculating capacitance results in several problems. First, the double layer potential is unknown. Second, the slopes are not steep enough at any part of the curve. In all four plots of Fig. B-8, the slope is sharpest at the very beginning. Calculating the capacitance per area using the appropriate value of R calculated by Eq. 3.1 and scaling by WE area, all four plots give values on the order of $1 \times 10^5\,\mu F/cm^2$. At larger times when the slope decreases further, the calculated capacitance value increases and deviates further from the correct magnitude. Recall

from earlier that the *RC* time scale from theoretical values was on the order of tens of microseconds; this chronoamperometry current does not decay fast enough to be modeled by such methods.

B.4 Conclusions

In this appendix, three electrochemical methods were used to analyze RTILs using a specially designed parallel-plate electrochemical cell under vacuum. EIS is the traditional method by which capacitance curves are generated, however it suffers from long test times. For studying a particular RTIL this may not be an issue, but for tests requiring large numbers of candidate liquids be studied, such as identifying potential new propellants for electrospray systems, a faster method is preferable. EIS was used in Ch. 4 with two RTILs, [emim][BF_4] and [emim][Tf_2N], to serve as validation of these techniques and to add to the literature of RTIL capacitance curves. CV is a method typically used to locate the electrochemical window, and to study Faradaic reactions beyond the window. It was hypothesized that at slow enough scans within the electrochemical window, voltammetry could capture charging dynamics of the double layer. Our tests gave repeatable results which scaled with scan rate in a manner consistent with our expectations. However, the signal was three orders of magnitude too large, indicating that our model was not appropriate for getting capacitance from CV current. Two chronoamperometric techniques were also attempted. The first, the potentiostatic intermittent titration technique, used small perturbations over which we could assume the capacitance was approximately constant. The *RC* current decay was fitted with exponential models at each voltage step. This method also overestimated the capacitance by orders of magnitude and also proved to be extremely noisy. The second was a single step chronoamperometry using a large 1 V perturbation. The current in this case could not decay fast enough to be governed by simple *RC* charging.

Due to the inconsistent capacitance magnitude compared to EIS, these methods were not pursued further within this thesis. However, recent reports of zero-frequency

methods for calculating capacitance [176, 177] have also seen increased capacitance over AC methods. In fact, the curve shapes reported by Nishi et al. show qualitative features that were observed in the CV and PITT results presented in this Appendix, including the hump near zero which disagreed with AC results and mean field models. Also the magnitude of the capacitance estimated by Chu et al. are on the same order of magnitude as those obtained with the transient methods here. This suggests that it may be of practical interest for future work to focus on improving the methods presented here. The first immediate improvements may come from achieving a WE that better approximates a blocking electrode.

The cell was seen to allow reactions, despite the tested voltages being well within the electrochemical window. This could be inferred from the Nyquist plots taking on curvature in the EIS results. Voltammetry also showed rising current levels especially on the negative end. The faster scans used for locating the electrochemical window did not show this behavior, but faster scans will not allow for accurate association of differential capacitance and double layer potential values. Each step in PITT, for pure capacitor charging should asymptote to zero current. In practice, within the time allowed for each step, the current at larger polarizations seemed to asymptote to a nonzero value indicating the presence of other components of current, possibly including Faradaic current. This may be due to the presence of contaminants or due to dissociation of solvated ion pairs [154, 155]. These ion pair dissociations are a new field of study and further analysis of the data collected in this work may reveal new information about those reactions. If a new cell can be designed to discourage the noncharging current, perhaps by using a less reactive metal, it is possible that these or other electrochemical methods will allow for accurate and faster generation of capacitance data.

Appendix C

Derivation of Bounded Warburg Impedance

The Nyquist plots generated from electrochemical impedance spectroscopy at porous carbon xerogel electrodes were fitted with a bounded Warburg impedance model in Ch. 4. The equation is derived here, following discussions with Juhyun Song [178].

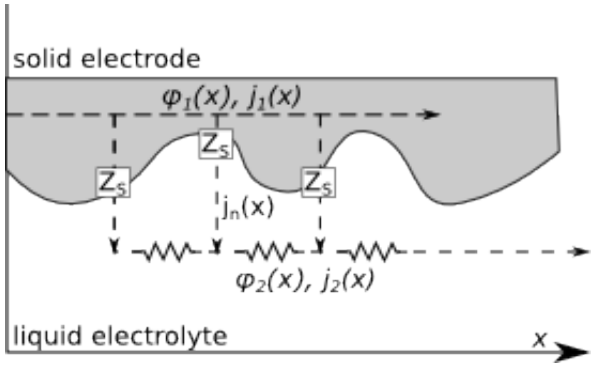

Figure C-1: Current distribution along a pore and an equivalent circuit transmission line model.

Over each parallel branch of local impedance $z_s = Z_s A_{pp}$ in a finite transmission line as in Fig. C-1 and 4-12, the current exchange from solid (1) to electrolyte (2) can be expressed as

$$j_n = \frac{\phi_1 - \phi_2}{z_s} \tag{C.1}$$

where A_{pp} is the area of the parallel-plate flat electrode at which Z_s was obtained.

The potential gradient and current in each phase are related through Ohm's law,

$$\sigma_1' \nabla \phi_1 = -(j_t - j_2) \tag{C.2}$$

$$\sigma_2' \nabla \phi_2 = -j_2 \tag{C.3}$$

where $\sigma_1' = {}^{(1-\epsilon_p)\sigma_1}/_{\tau}$ and $\sigma_2' = {}^{\epsilon_p \sigma_2}/_{\tau}$ are apparent conductivities dependent on porosity ϵ_p and tortuosity τ, and j_t is the total current density across both phases. Combining the two equations,

$$\nabla (\phi_1 - \phi_2) = -\frac{j_t}{\sigma_1'} + \left(\frac{1}{\sigma_1'} + \frac{1}{\sigma_2'} \right) j_2 \tag{C.4}$$

$$\nabla^2 (\phi_1 - \phi_2) = \left(\frac{1}{\sigma_1'} + \frac{1}{\sigma_2'} \right) \nabla j_2 \tag{C.5}$$

with the first term on the right being dropped due to j_t being constant. We can express current conservation in the electrolyte phase as

$$\begin{aligned} \nabla j_2 &= \bar{a} j_n \\ &= \bar{a} \frac{\phi_1 - \phi_2}{z_s} \end{aligned} \tag{C.6}$$

where $\bar{a}$ is the specific wall area, or wall area per unit volume of porous material. Combining Eq. C.5 and C.6, defining zero potential in the solid phase $\phi_1 = 0$, and using $\sigma_1' \gg \sigma_2'$, we get the governing equation

$$\nabla^2 \phi = \frac{\bar{a}}{\sigma' z_s} \phi \tag{C.7}$$

where the subscripts have been dropped, $\phi_2 = \phi$ and $\sigma_2' = \sigma'$. The boundary conditions for this system are:

$$\begin{aligned} \mathbf{n} \cdot \nabla \phi &= 0 \quad &&, \text{at current collector} \\ \phi &= -V \quad &&, \text{at bulk electrolyte} \end{aligned} \tag{C.8}$$

which is a blocking boundary condition at the current collector and a Dirichlet bound-

ary condition at the electrolyte bulk interface.

Based on the geometry of the electrode, shown in Fig. 3-4, we use a 1D solution for simplicity,

$$\frac{d^2\phi}{dx^2} = \Lambda^2\phi \tag{C.9}$$

for the governing equation with $\Lambda^2 = {}^{\bar{a}}/_{\sigma' z_s}$ and

$$\left.\frac{d\phi}{dx}\right|_{x=0} = 0 \tag{C.10}$$

$$\phi|_{x=L} = -V \tag{C.11}$$

for the boundary conditions. This can be solved analytically as

$$\phi(x) = c_1 \sinh \Lambda x + c_2 \cosh \Lambda x \tag{C.12}$$

with constants imposed by the boundary conditions as

$$\begin{aligned} c_1 &= 0 \\ c_2 &= \frac{-V}{\cosh \Lambda L} \end{aligned} \tag{C.13}$$

from Eq. C.10 and C.11, respectively.

Defining the cross sectional area A_{cs} for the bulk electrolyte interface, the total impedance is defined as

$$Z = \frac{V}{A_{cs} j_t} \tag{C.14}$$

where $j_t = j_2\,(x = L) = -\sigma' \left.\frac{d\phi}{dx}\right|_{x=L}$. Using the solution Eq. C.12, we get

$$\begin{aligned} Z &= \frac{V}{A_{cs}\sigma'\,(-c_2 \Lambda \sinh \Lambda L)} \\ &= \frac{\coth \Lambda L}{A_{cs}\sigma' \Lambda} \end{aligned} \tag{C.15}$$

Finally, replacing all of the temporary variables, we get the porous electrode impedance

as

$$Z(\omega) = \frac{1}{A_{cs}} \sqrt{\frac{Z_s\left(\omega\right) A_{pp}}{\bar{a}\sigma'}} \coth\left(\sqrt{\frac{\bar{a}L^2}{\sigma' Z_s\left(\omega\right) A_{pp}}}\right) \tag{C.16}$$

where $Z_s = Z_{CPE} = {}^{1}/_{Y_0(j\omega)^{\alpha}}$ with Y_0 and α taken from parallel plate data fits.

Appendix D

Electrochemical Decomposition of Ionic Liquids

The content here was originally published by the American Institute of Aeronautics and Astronautics in the Proceedings of the 49th Joint Propulsion Conference [2].

The focus of this thesis was the study of RTIL capacitance and charging dynamics in order to avoid electrochemistry. However, it is important to have some understanding of what happens when it cannot be completely avoided. Electrochemical degradation is known to be a life-limiting factor for many electrospray systems. Metal emitters will have their geometry modified, with sharp features being dulled so that eventually the electric field can no longer be amplified to support Taylor cone-type deformed menisci. The liquid will undergo reduction and oxidation reactions, the products of which act as impurities which change the physical properties.

In order to start to understand the reactions which lead to consumption of the electrode material and electrochemical decomposition of the RTIL, a series of experiments were conducted to identify the electrolytic gas products from [emim][BF_4] and [emim][Tf_2N]. The electrolysis cell is shown in figure D-1. Measurements were taken inside a vacuum chamber with an Extorr residual gas analyzer (RGA).

The electrolysis cell was designed to operate in vacuum conditions. Although pure ionic liquid has negligible vapor pressure and thus will not boil off in vacuum, the liquids we used were of 99% purity. Also, exposure to ambient air during preparation

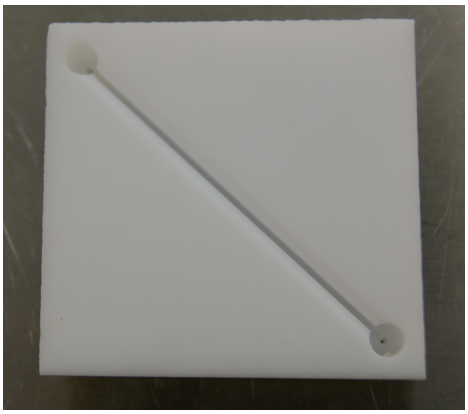

Figure D-1: Vacuum electrolysis cell with two 0.5 mm Pt electrodes. Power was supplied by a VersaSTAT 3 potentiostat.

allowed absorption of water. As pressure was decreased, water and other impurities would boil out, forming bubbles in the ionic liquid. It was necessary to allow these gases to escape and to allow the ionic liquid to refill the voids left by the bubbles. Another requirement was to minimize the amount of ionic liquid necessary for each experiment. The final design of the electrolysis cell had two cyclindrical wells 6 mm in diameter and 7 mm in depth, placed 56.6 mm apart. The two wells were connected by a channel 1.016 mm in width and 7 mm in depth. The cell was constructed of Teflon PTFE. Two platinum rods 0.5 mm in diameter were placed in the center of each well as electrodes, with length 2 mm exposed to the ionic liquid. A Princeton Applied Research VersaSTAT 3 potentiostat was connected across the two electrodes.

The Extorr RGA uses a quadrupole mass spectrometer to measure the partial pressure of species at specific charge-to-mass ratios. Our RGA was set to scan through the mass range 1 to 210 amu. The RGA requires a total pressure below 10^{-3} torr; the experiments were conducted at pressures on the order of 10^{-7} to 10^{-6} torr.

D.1 Gas Identification

The potentiostat was set to operate in a single staircase linear scan voltammetry mode, with voltages from 0 to 8 V at 200 mV increments. The duration of each step was set to 3 minutes so as to give time for the electrochemistry to adjust to each new

voltage as well as allow for gases generated at the previous voltage to be removed. The RGA made a scan of the full mass range at the end of each voltage step.

Select partial pressure measurements are shown in figure D-2. The data from other voltages were removed for clarity. Background species have been removed from the data by subtracting the partial pressures at 0 V for each mass. A high-pass filter at 250 ppm (using the total pressure recorded with each RGA scan) has been applied to suppress noise. The mass range presented is cut off at 120 amu, as no strong signals were recorded at higher masses.

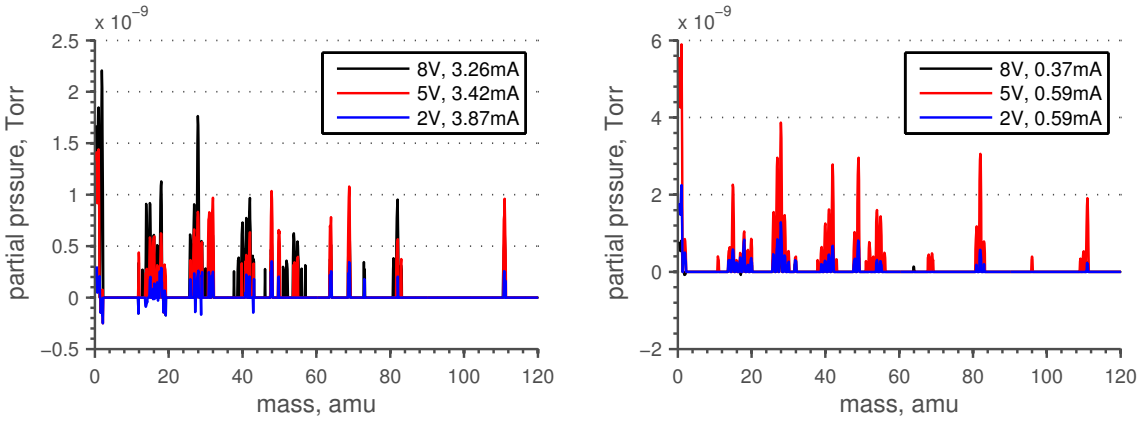

Figure D-2: Partial pressures recorded at various voltages. Background species and signals below 250 ppm have been removed. The current drawn at each voltage is indicated in the legend. Results for [emim][Tf_2N] on left, [emim][bf_4] on right.

In order to identify the species making up each mass signal, possible fragments of the ionic liquid cation and anion, as well as species in air, were studied. No further reactions, in which fragments may have reacted with each other, were considered. A more detailed study of the electrochemical reactions will be able to verify these products. An example of such a study was conducted for the gas evolution from propylene carbonate [179]. Table D.1 lists the mass peaks observed for each ionic liquid at 5 V, its relative abundance (partial pressure at the mass divided by the total pressure), and the associated species.

Although the rga measurement for the background case 0 V is not shown, a few interesting observations were made. The strongest signals were at masses of 1, 18, 28, 14, 16, 17, 2, and 32 amu, respectively. These correspond to species in air, i.e. H, H_2O,

Table D.1: List of mass peaks observed for both [emim][Tf_2N] and [emim][BF_4] electrolysis at 5 V. For each mass peak (amu), the corresponding abundance and possible species are listed. Blue text indicates species associated with air.

[emim][Tf_2N]			[emim][BF_4]		
amu	abundance	species	amu	abundance	species
1	0.1020	H	1	0.1367	H
18	0.0887	H_2O	28	0.0829	N_2, CH_2N, C_2H_4
28	0.0744	N_2, CH_2N, C_2H_4	82	0.0580	$C_4H_6N_2$, C_5H_8N
32	0.0555	O_2, S	49	0.0579	BF_2
69	0.0483	CF_3, $C_3H_5N_2$, C_4H_7N	27	0.0561	CHN, C_2H_3
16	0.0480	O	42	0.0527	C_2H_4N
48	0.0464	SO	15	0.0444	CH_3
111	0.0430	$C_6H_{11}N_2$([emim])	111	0.0362	$C_6H_{11}N_2$([emim])
14	0.0429	N, CH_2	41	0.0307	CHN_2, C_2H_3N
31	0.0371	CF	54	0.0304	$C_2H_2N_2$, C_3H_4N
64	0.0371	SO_2, C_3N_2, C_4H_2N	26	0.0293	CN, C_2H_2
17	0.0319	OH	18	0.0293	H_2O
27	0.0296	CHN, C_2H_3	29	0.0278	C_2H_5
50	0.0293	CF_2, C_3N	55	0.0273	$C_2H_3N_2$, C_3H_5N
42	0.0284	C_2H_4N	2	0.0252	H_2
19	0.0279	F	40	0.0237	Ar, CN_2, C_2H_2N
15	0.0262	CH_3	81	0.0224	$C_4H_5N_2$, C_5H_7N
29	0.0241	C_2H_5	48	0.0195	
82	0.0238	CF_2S, $C_4H_6N_2$, C_5H_8N	20	0.0162	Ne
41	0.0228	CHN_2, C_2H_3N	19	0.0156	F
12	0.0196	C	83	0.0149	$C_4H_7N_2$
2	0.0183	H_2	14	0.0147	N, CH_2
55	0.0178	$C_2H_3N_2$, C_3H_5N	52	0.0146	C_2N_2, C_3H_2N
83	0.0168	$C_4H_7N_2$	39	0.0122	C_2HN
26	0.0163	CN, C_2H_2	17	0.0114	OH
40	0.0149	Ar, CN_2, C_2H_2N	30	0.0102	BF
43	0.0148	C_2H_5N	110	0.0101	$C_6H_{10}N_2$
54	0.0142	$C_2H_2N_2$, C_3H_4N	56	0.0094	$C_2H_4N_2$, C_3H_6N
			69	0.0091	$C_3H_5N_2$, C_4H_7N
			68	0.0085	BF_3, $C_3H_4N_2$, C_4H_6N
			16	0.0084	O
			32	0.0078	O_2
			11	0.0076	B
			53	0.0075	C_2HN_2, C_3H_3N
			96	0.0075	$C_5H_8N_2$
			109	0.0065	$C_6H_9N_2$
			43	0.0062	C_2H_5N
			38	0.0057	C_2N
			51	0.0053	C_3HN

N_2, N, O, OH, H_2, and O_2, where O and OH are fragments of water. However, smaller peaks above the 250 ppm threshold were also found in the [emim][Tf_2N] case at 19, 27, 41, 29, 48, 12, 15, and 64 amu. These masses correspond to the possible species F; HCN and C_2H_3; C_2H_3N (acetonitrile) and CHN_2; C_2H_5 (ethyl group); SO; C; CH_3 (methyl group); and SO_2, C_3N_2, and C_4H_2N. In the [emim][BF_4] case, the extra peaks were at 19, 27, 29, and 15 amu, corresponding to F; CHN and C_2H_3; C_2H_5; and CH_3. Although these peaks were minor (the largest species, F in both cases, contributed 3.7% in [emim][Tf_2N] and 6.7% in [emim][BF_4] of the total pressure), it shows that the ionic liquids have a degree of instability and that small amounts of fragments may be escaping without any applied voltage.

D.2 Pressure Buildup

Another set of experiments was conducted to characterize the pressure buildup due to electrolysis of the ionic liquid [emim][Tf_2N]. A pressure vessel was constructed with PEEK, as shown in figure D-3. Pressure measurements were taken with an Omega PX409USB pressure transducer, rated from 0 to 50 psia.

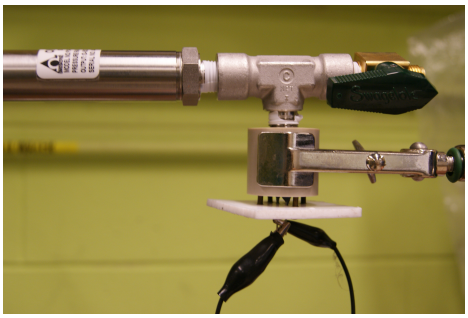

Figure D-3: Pressure vessel electrolysis cell with two 0.5 mm Pt electrodes. Power supplied by Keithley 2410 SourceMeter.

The pressure vessel walls were sized to hold over 100 atm of pressure, calculated from the ultimate stress of PEEK. A 11.11 mm diameter cylindrical well was milled into a 31.75 mm diameter PEEK cylinder. The well was 25.4 mm deep. Two platinum electrodes of the same dimensions as in the vacuum cell were placed 7.94 mm apart inside the well. The top portion of the well was tapped for a 1/4 inch NPT connection

and connected to a tee. One side of the tee connected to the pressure transducer, and the other to a roughing pump through a valve. The chamber was tested to hold positive pressure by pressurization with air to beyond the pressure transducer's 50 psia limit. Negative pressure was tested using a roughing pump, which could pump the cell down to approximately 0.5 psia. Despite sealing all connections with PTFE tape, leaking was observed. Positive pressures from 40 psia decayed in ≈ 15 min to an asymptote at 16.52 psia. Negative pressures from 0.5 psia increased in ≈ 13 min to an asymptote at 12.90 psia. Pressures between these two could be held without significant changes.

The cell, when filled with [emim][Tf_2N] and no voltage applied, showed a resistance of 3 MΩ across the electrode leads. Current through the cell was measured across a 1 kΩ resistor in series, recorded with a Keithley 6517 Electrometer. Voltage was applied using a Keithley 2410 SourceMeter.

D.2.1 Under moderate vacuum

A series of tests were run to characterize pressure buildup due to electrolysis starting from moderate vacuum. For each test, the tee was disconnected from the chamber, 0.8 mL of [emim][Tf_2N] was introduced, then the tee reconnected with new PTFE sealant. The valve was then opened and the chamber pumped down; the valve was kept open for 1 h to allow for outgassing of the water, as previously discussed. As the vacuum could not be properly maintained in the chamber, pressure measurements were taken before each test to characterize the leak with no voltage applied. After the leak measurements, the valve was reopened to reestablish vacuum, and then shut again when the voltage was applied.

Results

The pressure buildup, calculated as the leak pressure measurement subtracted from the pressure measurement under voltage, is shown in figure D-4. 1000 data points were taken at 1 s intervals. No significant pressure buildup could be seen with 5 or 8 V

applied. Current and voltage (adjusted for the drop across the measurement resistor) are also shown. For the 5 V case, the voltage and current seem to be approaching an asymptote near the end of the test, and a longer duration test was conducted to observe its development. For the longer tests, a vacuum was no longer applied as the leak would negate its effects. The negative pressure changes seen in the 8 V case is also seen in the longer duration tests.

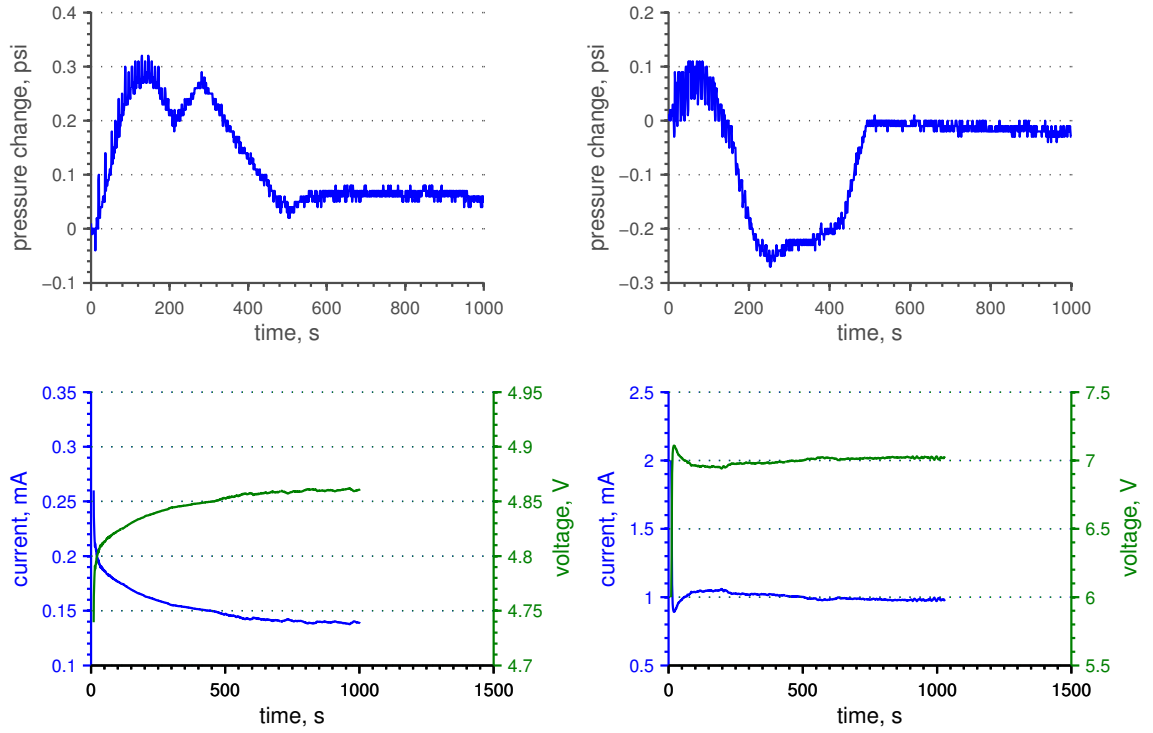

Figure D-4: Pressure buildup calculated as pressure measurement under voltage minus leak pressure. No significant pressure buildup was observed in 1000 s. The plots on left are at 5 V, and those on right are at 8 V.

D.2.2 From atmospheric pressure

The same PEEK cell was used for long-duration tests. The valve was sealed after the introduction of 1.6 mL of ionic liquid into the chamber, and voltage applied. 1000 measurements were taken at 30 s intervals, for a total duration of 8 hours and 20 minutes. In these tests, the roughing pump was not used as the moderate vacuum was seen to leak, returning to close to atmospheric values in the timescale of the

vacuum tests, 16 minutes and 40 seconds.

Results

Tests were conducted at voltages of 5 V and 15 V. The pressure is shown as a function of time in figure D-5, along with the corresponding current and voltage across the Pt electrodes. The pressures throughout this test remained within the leak boundaries and are determined to be accurate.

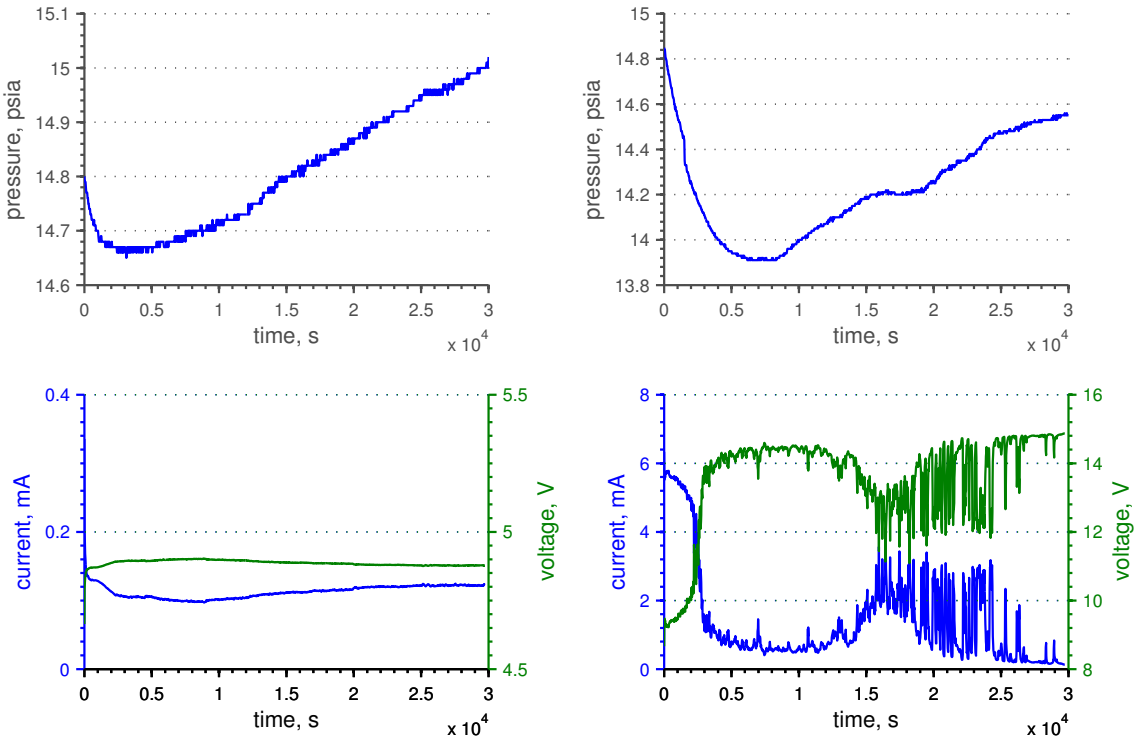

Figure D-5: Long duration pressure buildup due to electrolysis of [emim][Tf_2N]. The case of 5 V (left) shows a steadying of the voltage and pressure rise. However, the 15 V case (right) shows significant oscillations in voltage, suggesting fluctuations in the conductivity of the ionic liquid.

The 5 V case, which was seen to be approaching a voltage asymptote in the shorter-duration test, is observed in the longer timescale to exhibit a steadily decreasing voltage after its initial rise. This can be explained by a steady increase in the conductivity of the liquid as electrochemical reactions take place. Another piece of evidence for physical changes in the ionic liquid can be seen in figure D-6. The image shows the ionic liquid before and after the long-duration test. The liquid turned orange.

Figure D-6: [emim][Tf_2N] before and after the long-duration electrolysis test. The clear liquid is [emim][Tf_2N] before it has been electrolyzed. The orange liquid is the result of the 5 V test. The darkest liquid is the result of the 15 V test.

Although no quantitiave measurements were made, the viscosity of the liquid seemed to increase as well. The volume of liquid decreased by less than 0.1 mL.

The 15 V case shows no steady performance; it is characterized by large fluctuations in voltage and current. This test often drew currents an order of magnitude larger than in the 5 V case; this suggests a drastic reduction of resistivity in the ionic liquid. The liquid at the end of the test had a very dark orange color and was more viscous than that after the 5 V test.

Both tests show the pressure to decrease initially, before reaching a trough and a subsequent pressure rise. In the 5 V case, the pressure increases beyond the original atmospheric pressure; in the 15 V case, the pressure did not return to atmospheric within the timescale of the experiment. In order to test if the pressure drop was due to reactions with the chamber itself, an electrolysis test with water was conducted in the same conditions. The pressure was seen to rise linearly with no initial drop. [emim][Tf_2N] is known to absorb water from exposure to air. A possible explanation for the reduction in pressure is an electrical activation of that absorption mechanism. Initially, the ionic liquid withdraws more water molecules from the air than the number of decomposed gases. As voltage rises, the electrochemical decomposition process becomes dominant and the pressure begins to rise. This is consistent with the results of section D.2.1, as those tests were started in vacuum; there would have been fewer water molecules available to be absorbed and thus the smaller dip in pressure for 8 V, and no negative pressure for 5 V. A future experiment in which the initial air is flushed with N_2 or Ar will show if the pressure drop is a result of reactions with air. Another possibility is to design a chamber to better hold a vacuum, and to start the long duration tests from vacuum conditions. If the initial condition is already under vacuum, negative pressure cannot be created; however, as seen in section D.2.1, no

significant positive pressure may be created in the short-term.

Bibliography

[1] D. G. Courtney, H. Li, P. Diaz Gomez Maqueo, T. P. Fedkiw, and P. C. Lozano, "On the validation of porous nickel as substrate material for electrospray ion propulsion," in *46th AIAA/ASME/SAE/ASEE Joint Propulsion Conference & Exhibit*, (Nashville, TN), 2010.

[2] K. Masuyama and P. C. Lozano, "Bimodal propulsion system using ionic liquid propellant for pico- and nano-satellite applications," in *49th AIAA/ASME/SAE/ASEE Joint Propulsion Conference*, (San Jose, CA), 2013.

[3] D. Krejci, F. Mier-Hicks, C. Fucetola, P. Lozano, A. H. Schouten, and F. Martel, "Design and characterization of a scalable ion electrospray propulsion system," in *Joint Conference of 30th ISTS, 34th IEPC and 6th NSAT*, (Hyogo-Kobe, Japan), 2015.

[4] J. K. Ziemer, T. M. Randolph, G. W. Franklin, V. Hruby, D. Spence, N. Demmons, T. Roy, E. Ehrbar, J. Zwahlen, R. Martin, and W. Connolly, "Delivery of colloid micro-newton thrusters for the space technology 7 mission," in *44th AIAA/ASME/SAE/ASEE Joint Propulsion Conference & Exhibit*, (Hartford, CT), 2008.

[5] V. Hruby, D. Spence, N. Demmons, T. Roy, E. Ehrbar, J. Zwahlen, R. Martin, J. Ziemer, T. Randolph, W. Connolly, S. Rhodes, and W. Tolman, "ST7-DRS colloid thruster system development and performance summary," in *44th AIAA/ASME/SAE/ASEE Joint Propulsion Conference & Exhibit*, (Hartford, CT), 2008.

[6] N. Demmons, V. Hruby, D. Spence, T. Roy, E. Ehrbar, J. Zwahlen, R. Martin, J. Ziemer, and T. Randolph, "ST7-DRS mission colloid thruster development," in *44th AIAA/ASME/SAE/ASEE Joint Propulsion Conference & Exhibit*, (Hartford, CT), 2008.

[7] P. C. Lozano, B. L. Wardle, P. Moloney, and S. Rawal, "Nanoengineered thrusters for the next giant leap in space exploration," *MRS Bulletin*, vol. 40, no. 10, pp. 842–849, 2015.

[8] T. Sato, G. Masuda, and K. Takagi, "Electrochemical properties of novel ionic liquids for electric double layer capacitor applications," *Electrochimica Acta*, vol. 49, no. 21, pp. 3603–3611, 2004.

[9] A. Balducci, R. Dugas, P. Taberna, P. Simon, D. Plée, M. Mastragostino, and S. Passerini, "High temperature carbon-carbon supercapacitor using ionic liquid as electrolyte," *Journal of Power Sources*, vol. 165, no. 2, pp. 922–927, 2007.

[10] E. Frackowiak, "Carbon materials for supercapacitor application," *Physical Chemistry Chemical Physics*, vol. 9, pp. 1774–1785, 2007.

[11] M. Galiński, A. Lewandowski, and I. Stępniak, "Ionic liquids as electrolytes," *Electrochimica Acta*, vol. 51, no. 26, pp. 5567–5580, 2006.

[12] C. Perez-Martinez, S. Guilet, N. Gogneau, P. Jegou, J. Gierak, and P. Lozano, "Development of ion sources from ionic liquids for microfabrication," *Journal of Vacuum Science & Technology B*, vol. 28, no. 3, 2010.

[13] Y. Su, Y. Fu, Y. Wei, J. Yan, and B. Mao, "The electrode/ionic liquid interface: Electric double layer and metal electrodeposition," *ChemPhysChem*, vol. 11, no. 13, pp. 2764–2778, 2010.

[14] N. Fietkau, A. D. Clegg, R. G. Evans, C. Villagr/'an, C. Hardacre, and R. G. Compton, "Electrochemical rate constants in room temperature ionic liquids: The oxidation of a series of ferrocene derivatives," *ChemPhysChem*, vol. 7, no. 5, pp. 1041–1045, 2006.

[15] D. S. Silvester and R. G. Compton, "Electrochemistry in room temperature ionic liquids: A review and some possible applications," *Zeitschrift für Physikalische Chemie*, vol. 220, no. 10, pp. 1247–1274, 2006.

[16] T. Welton, "Room-temperature ionic liquids. solvents for synthesis and catalysis," *Chemical Reviews*, vol. 99, no. 8, pp. 2071–2084, 1999.

[17] S. Perkin, T. Albrecht, and J. Klein, "Layering and shear properties of an ionic liquid, 1-ethyl-3-methylimidazolium ethylsulfate, confined to nano-films between mica surfaces," *Physical Chemistry Chemical Physics*, vol. 12, no. 6, pp. 1243–1247, 2010.

[18] S. Zhang, N. Sun, X. He, X. Lu, and X. Zhang, "Physical properties of ionic liquids: Database and evaluation," *Journal of Physical and Chemical Reference Data*, vol. 35, no. 4, pp. 1475–1517, 2006.

[19] D. Moosbauer, S. Jordan, F. Wudy, S. S. Zhang, M. Schmidt, and H. J. Gores, "Determination of electrochemical windows of novel electrolytes for double layer capacitors by stepwise cyclic voltammetry experiments," *Acta Chimica Slovenica*, vol. 56, pp. 218–224, 2009.

[20] D. H. Zaitsau, G. J. Kabo, A. A. Strechan, Y. U. Paulechka, A. Tschersich, S. P. Verevkin, and A. Heintz, "Experimental vapor pressures of 1-Alkyl-3-methylimidazolium

Bis(trifluoromethylsulfonyl)imides and a correlation scheme for estimation of vaporization enthalpies of ionic liquids," *The Journal of Physical Chemistry A*, vol. 110, no. 22, pp. 7303–7306, 2006.

[21] D. Gilmore, *Spacecraft Thermal Control Handbook, Volume 1: Fundamental Technologies*. California: The Aerospace Press, 2002.

[22] W. C. Burson Jr. and P. C. Herren Jr., "Alternating current operation of a colloid source," *Journal of Spacecraft and Rockets*, vol. 8, no. 6, pp. 606–611, 1971.

[23] P. Lozano and M. Martínez-Sánchez, "Ionic liquid ion sources: suppression of electrochemical reactions using voltage alternation," *Journal of Colloid and Interface Science*, vol. 280, no. 1, pp. 149–154, 2004.

[24] J. A. Carretero Benignos, *Numerical Simulation of a single emitter colloid thruster in pure droplet cone-jet mode*. PhD thesis, Massachusetts Institute of Technology, Cambridge, MA, 2005.

[25] P. Lozano, B. Glass, and M. Martinez-Sanchez, "Performance characteristics of a linear ionic liquid electrospray thruster," in *29th International Electric Propulsion Conference*, (Princeton, NJ), 2005.

[26] P. Lozano and M. Martínez-Sánchez, "Experimental measurements of colloid thruster plumes in the ion-droplet mixed regime," in *38th AIAA/ASME/SAE/ASEE Joint Propulsion Conference & Exhibit*, (Indianapolis, IN), 2002.

[27] H. Helmholtz, "Ueber einige gesetze der vertheilung elektrischer ströme in körperlichen leitern mit anwendung auf die thierisch-elektrischen versuche," *Annalen der Physik*, vol. 165, no. 6, pp. 211–233, 1853.

[28] A. J. Bard and L. R. Faulkner, *Electrochemical Methods: Fundamentals and Applications*. New York: Wiley, 2 ed., 2001.

[29] M. Bathe, A. J. Grodzinsky, B. Tidor, and G. C. Rutledge, "Optimal linearized Poisson-Boltzmann theory applied to the simulation of flexible polyelectrolytes in solution," *Journal of Chemical Physics*, vol. 121, no. 16, 2004.

[30] O. Stern, "The theory of the electrolytic double-layer," *Z. Elektrochem*, vol. 30, no. 508, pp. 1014–1020, 1924.

[31] D. C. Grahame, "The electrical double layer and the theory of electrocapillarity," *Chemical Review*, vol. 41, no. 3, pp. 441–501, 1947.

[32] J. O. Bockris, M. A. V. Devanathan, and K. Müller, "On the structure of charged interfaces," *Proceedings of the Royal Society A*, vol. 274, no. 1356, 1963.

[33] B. E. Conway, "Transition from "supercapacitor" to "battery" behavior in electrochemical energy storage," *Journal of the Electrochemical Society*, vol. 138, no. 6, pp. 1539–1548, 1991.

[34] R. A. Marcus, "On the theory of oxidation-reduction reactions involving electron transfer. I," *The Journal of Chemical Physics*, vol. 24, no. 966, 1956.

[35] R. A. Marcus, "On the theory of oxidation-reduction reactions involving electron transfer. II. applications to data on the rates of isotopic exchange reactions," *The Journal of Chemical Physics*, vol. 26, no. 867, 1957.

[36] R. A. Marcus, "On the theory of oxidation-reduction reactions involving electron transfer. III. applications to data on the rates of organic redox reactions," *The Journal of Chemical Physics*, vol. 26, no. 872, 1957.

[37] R. A. Marcus, "Exchange reactions and electron transfer reactions including isotopic exchange. theory of oxidation-reduction reactions involving electron transfer. part 4.–a statistical-mechanical basis for treating contributions from solvent, ligands, and inert salt," *Discussions of the Faraday Society*, vol. 29, pp. 21–31, 1960.

[38] R. A. Marcus, "On the theory of oxidation-reduction reactions involving electron transfer. V. comparison and properties of electrochemical and chemical rate constants," *The Journal of Physical Chemistry*, vol. 67, no. 4, pp. 853–857, 1963.

[39] R. A. Marcus, "Chemical and electrochemical electron-transfer theory," *Annual Review of Physical Chemistry*, vol. 15, pp. 155–196, 1964.

[40] R. A. Marcus, "On the theory of electron-transfer reactions. VI. unified treatment for homogeneous and electrode reactions," *The Journal of Chemical Physics*, vol. 43, no. 679, 1965.

[41] K. A. Dill and S. Bromberg, *Molecular Driving Forces: Statistical Thermodynamics in Chemistry and Biology*. New York: Garland Science, 2003.

[42] M. S. Kilic, M. Z. Bazant, and A. Ajdari, "Steric effects in the dynamics of electrolytes at large applied voltages. II. Modified Poisson-Nernst-Planck equations," *Physical Review E*, vol. 75, no. 2, 2007.

[43] R. de Levie, "On porous electrodes in electrolyte solutions," *Electrochimica Acta*, vol. 8, pp. 751–780, 1963.

[44] P. M. Biesheuvel and M. Z. Bazant, "Nonlinear dynamics of capacitive charging and desalination by porous electrodes," *Physical Review E*, vol. 81, no. 3, 2010.

[45] R. A. Rica, R. Ziano, D. Salerno, F. Mantegazza, M. Z. Bazant, and D. Brogioli, "Electrodiffusion of ions in porous electrodes for capacitive extraction of renewable energy from salinity differences," *Electrochimica Acta*, vol. 92, pp. 304–314, 2013.

[46] G. Taylor, "Disintegration of water drops in an electric field," *Proceedings of the Royal Society A*, vol. 280, no. 1382, 1964.

[47] D. A. Saville, "Electrohydrodynamics: The Taylor-Melcher leaky dielectric model," *Annual Review of Fluid Mechanics*, vol. 29, pp. 27–64, 1997.

[48] F. J. Higuera, "Model of the meniscus of an ionic-liquid ion source," *Physical Review E*, vol. 77, no. 2, 2008.

[49] C. Coffman, *Electrically-Assisted Evaporation of Charged Fluids: Fundamental Modeling and Studies on Ionic Liquids*. PhD thesis, Massachusetts Institute of Technology, Cambridge, MA, 2016.

[50] M. Z. Bazant, B. D. Storey, and A. A. Kornyshev, "Double layer in ionic liquids: Overscreening versus crowding," *Physical Review Letters*, vol. 106, no. 4, 2011.

[51] R. R. Dogonadze and Y. A. Chizmadzhev, "Structure and capacitance of the metal-fused salt," *Interface Proceedings Academy of Sciences USSR Physical Chemical Section*, vol. 157, no. 944, pp. 778–781, 1964.

[52] A. Kisza, "The capacitance of the diffuse layer of electric double layer of electrodes in molten salts," *Electrochimica Acta*, vol. 51, no. 11, pp. 2315–2321, 2006.

[53] S. Lamperski and J. Kłos, "Grand canonical monte carlo investigations of electrical double layer in molten salts," *The Journal of Chemical Physics*, vol. 129, no. 16, 2008.

[54] M. Rovere and M. P. Tosi, "Structure and dynamics of molten salts," *Reports on Progress in Physics*, vol. 49, no. 9, pp. 1001–1081, 1986.

[55] R. Parsons, "Electrical double layer: Recent experimental and theoretical developments," *Chemical Reviews*, vol. 90, no. 5, pp. 813–826, 1990.

[56] M. V. Fedorov and A. A. Kornyshev, "Ionic liquids at electrified interfaces," *Chemical Reviews*, vol. 114, no. 5, pp. 2978–3036, 2014.

[57] J. J. Bikerman, "XXXIX. Structure and capacity of electrical double layer," *Philosophical Magazine*, vol. 33, no. 220, pp. 384–397, 1942.

[58] G. Gouy, "Electrocapillarity function," *Annales de Physique*, vol. 7, pp. 129–184, 1917.

[59] A. Frumkin, "Über die beeinflussung der adsorption von neutralmolekülen durch ein elektrisches feld," *Zeitschrift für Physik*, vol. 35, no. 10, pp. 792–802, 1926.

[60] J. A. V. Butler, "The equilibrium of heterogeneous systems including electrolytes. part III. the effect of an electric field on the adsorption of organic molecules, and the interpretation of electrocapillary curves," *Proceedings of the Royal Society A*, vol. 122, no. 790, pp. 399–416, 1929.

[61] M. Eigen and E. Wicke, "The thermodynamics of electrolytes at higher concentration," *The Journal of Physical Chemistry*, vol. 58, no. 9, pp. 702–714, 1954.

[62] A. Eucken, "Assoziation in flüssigkeiten," *Zeitschrift für Elektrochemie und angewandte physikalische Chemie*, vol. 52, no. 6, pp. 255–269, 1948.

[63] K. Bohinc, A. Iglič, T. Slivnik, and V. Kralj-Iglič, "Charged cylindrical surfaces: effect of finite ion size," *Bioelectrochemistry*, vol. 57, no. 1, pp. 73–81, 2002.

[64] I. Borukhov, D. Andelman, and H. Orland, "Steric effects in electrolytes: A modified poisson-boltzmann equation," *Physical Review Letters*, vol. 79, no. 3, pp. 435–438, 1997.

[65] I. Borukhov, "Charge renormalization of cylinders and spheres: Ion size effects," *Journal of Polymer Science Part B: Polymer Physics*, vol. 42, no. 19, pp. 3598–3615, 2004.

[66] D. Antypov, M. C. Barbosa, and C. Holm, "Incorporation of excluded-volume correlations into Poisson-Boltzmann theory," *Physical Review E*, vol. 71, no. 6, 2005.

[67] G. M. Torrie and J. P. Valleau, "Electrical double layers. I. Monte Carlo study of a uniformly charged surface," *The Journal of Chemical Physics*, vol. 73, no. 11, pp. 5807–5816, 1980.

[68] A. A. Kornyshev, "Double-layer in ionic liquids: Paradigm change?," *The Journal of Physical Chemistry B*, vol. 111, no. 20, pp. 5545–5557, 2007.

[69] Y. Levin, "Electrostatic correlations: from plasma to biology," *Reports on Progress in Physics*, vol. 65, pp. 1577–1632, 2002.

[70] K. B. Oldham, "A Gouy-Chapman-Stern model of the double layer at a (metal)/(ionic liquid) interface," *Journal of Electroanalytical Chemistry*, vol. 613, no. 2, pp. 131–138, 2008.

[71] D. Henderson and S. Lamperski, "Simple description of the capacitance of the double layer of a high concentration electrolyte," *Journal of Chemical & Engineering Data*, vol. 56, no. 4, pp. 1204–1208, 2011.

[72] M. V. Fedorov and A. A. Kornyshev, "Towards understanding the structure and capacitance of electrical double layer in ionic liquids," *Electrochimica Acta*, vol. 53, no. 23, pp. 6835–6840, 2008.

[73] M. S. Kilic, *Induced-charge Electrokinetics at Large Voltages*. PhD thesis, Massachusetts Institute of Technology, Cambridge, MA, 2008.

[74] Y. Han, S. Huang, and T. Yan, "A mean-field theory on the differential capacitance of asymmetric ionic liquid electrolytes," *Journal of Physics: Condensed Matter*, vol. 26, no. 28, 2014.

[75] M. S. Kilic, M. Z. Bazant, and A. Ajdari, "Steric effects in the dynamics of electrolytes at large applied voltages. I. Double-layer charging," *Physical Review E*, vol. 75, no. 2, 2007.

[76] V. Kralj-Iglič and A. Iglič, "A simple statistical mechanical approach to the free energy of the electric double layer including the excluded volume effect," *Journal de Physique II*, vol. 6, no. 4, pp. 477–491, 1996.

[77] M. Z. Bazant, M. S. Kilic, B. D. Storey, and A. Ajdari, "Towards an understanding of induced-charge electrokinetics at large applied voltages in concentrated solutions," *Advances in Colloid and Interface Science*, vol. 152, pp. 48–88, 2009.

[78] B. D. Storey and M. Z. Bazant, "Effects of electrostatic correlations on electrokinetic phenomena," *Physical Review E*, vol. 86, no. 5, 2012.

[79] G. Feng, J. Huang, B. G. Sumpter, V. Meunier, and R. Qiao, "A "counter-charge layer in generalized solvents" framework for electrical double layers in neat and hybrid ionic liquid electrolytes," *Physical Chemistry Chemical Physics*, vol. 13, no. 32, pp. 14723–14734, 2011.

[80] A. A. Kornyshev, N. B. Luque, and W. Schmickler, "Differential capacitance of ionic liquid interface with graphite: the story of two double layers," *Journal of Solid State Electrochemistry*, vol. 18, no. 5, pp. 1345–1349, 2013.

[81] A. A. Kornyshev and R. Qiao, "Three-dimensional double layers," *The Journal of Physical Chemistry C*, vol. 118, no. 32, pp. 18285–18290, 2014.

[82] D. Bedrov, J. Vatamanu, and Z. Hu, "Ionic liquids at charged surfaces: Insight from molecular simulations," *Journal of Non-Crystalline Solids*, 2014.

[83] C. Merlet, B. Rotenberg, P. A. Madden, and M. Salanne, "Computer simulations of ionic liquids at electrochemical interfaces," *Physical Chemistry Chemical Physics*, vol. 15, no. 38, pp. 15781–15792, 2013.

[84] V. Ivaništšev and M. V. Fedorov, "Interfaces between charged surfaces and ionic liquids: Insights from molecular simulations," *Interface*, pp. 65–69, 2014.

[85] M. V. Fedorov and A. A. Kornyshev, "Ionic liquid near a charged wall: Structure and capacitance of electrical double layer," *The Journal of Physical Chemistry B*, vol. 112, no. 38, pp. 11868–11872, 2008.

[86] M. Fedorov, N. Georgi, and A. Kornyshev, "Double layer in ionic liquids: The nature of the camel shape of capacitance," *Electrochemistry Communications*, vol. 12, no. 2, pp. 296–299, 2010.

[87] J. N. Canongia Lopes, J. Deschamps, and A. A. H. Pádua, "Modeling ionic liquids using a systematic all-atom force field," *The Journal of Physical Chemistry B*, vol. 108, no. 6, pp. 2038–2047, 2004.

[88] J. N. Canongia Lopes and A. A. H. Pádua, "Molecular force field for ionic liquids composed of triflate or bistriflylimide anions," *The Journal of Physical Chemistry B*, vol. 108, no. 43, pp. 16893–16898, 2004.

[89] K. Shimizu, A. Pensado, P. Malfreyt, A. A. H. Pádua, and J. N. C. Lopes, "2D or not 2D: Structural and charge ordering at the solid-liquid interface of the 1-(2-hydroxyethyl)-3-methylimidazolium tetrafluoroborate ionic liquid," *Faraday Discussions*, vol. 154, pp. 155–169, 2012.

[90] P. Ballone, M. G. D. Pópolo, S. Bovio, A. Podestà, P. Milani, and N. Manini, "Nano-indentation of a room-temperature ionic liquid film on silica: a computational experiment," *Physical Chemistry Chemical Physics*, vol. 14, no. 7, pp. 2475–2482, 2012.

[91] D. Dragoni, N. Manini, and P. Ballone, "Interfacial layering of a room-temperature ionic liquid thin film on mica: A computational investigation," *ChemPhysChem*, vol. 13, no. 7, pp. 1772–1780, 2012.

[92] R. M. Lynden-Bell, A. I. Frolov, and M. V. Fedorov, "Electrode screening by ionic liquids," *Physical Chemistry Chemical Physics*, vol. 14, no. 8, pp. 2693–2701, 2012.

[93] J. Vatamanu, O. Borodin, D. Dedrov, and G. D. Smith, "Molecular dynamics simulation study of the interfacial structure and differential capacitance of alkylimidazolium bis(trifluoromethanesulfonyl)imide [$C_n$mim][TFSI] ionic liquids at graphite electrodes," *The Journal of Physical Chemistry C*, vol. 116, no. 14, pp. 7940–7951, 2012.

[94] Z. Hu, J. Vatamanu, O. Borodin, and D. Bedrov, "A molecular dynamics simulation study of the electric double layer and capacitance of [BMIM][PF_6] and [BMIM][BF_4] room temperature ionic liquids near charged surfaces," *Physical Chemistry Chemical Physics*, vol. 15, no. 34, pp. 14234–14247, 2013.

[95] X. Si, S. Li, Y. Wang, S. Ye, and T. Yan, "Effects of specific adsorption on the differential capacitance of imidazolium-based ionic liquid electrolytes," *ChemPhysChem*, vol. 13, no. 7, pp. 1671–1676, 2012.

[96] E. Paek, A. J. Pak, and G. S. Hwang, "A computational study of the interfacial structure and capacitance of graphene in [BMIM][PF_6] ionic liquid," *Journal of the Electrochemical Society*, vol. 160, no. 1, 2013.

[97] K. Kirchner, T. Kirchner, V. Ivaništšev, and M. Fedorov, "Electrical double layer in ionic liquids: Structural transitions from multilayer to monolayer structure at the interface," *Electrochimica Acta*, vol. 110, pp. 762–771, 2013.

[98] C. Merlet, D. T. Limmer, M. Salanne, R. van Roij, P. A. Madden, D. Chandler, and B. Rotenberg, "The electric double layer has a life of its own," *The Journal of Physical Chemistry C*, vol. 118, no. 32, pp. 18291–18298, 2014.

[99] V. Ivaništšev, S. O'Connor, and M. Fedorov, "Poly(a)morphic portrait of the electrical double layer in ionic liquids," *Electrochemistry Communications*, vol. 48, pp. 61–64, 2014.

[100] L. H. Olesen, M. Z. Bazant, and H. Bruus, "Strongly nonlinear dynamics of electrolytes in large ac voltages," *Physical Review E*, vol. 82, no. 1, 2010.

[101] H. Zhao, "Diffuse-charge dynamics of ionic liquids in electrochemical systems," *Physical Review E*, vol. 84, no. 5, 2011.

[102] A. Yochelis, "Transition from non-monotonic to monotonic electrical diffuse layers: impact of confinement on ionic liquids," *Physical Chemistry Chemical Physics*, vol. 16, no. 7, pp. 2836–2841, 2014.

[103] A. Yochelis, "Spatial structure of electrical diffuse layers in highly concentrated electrolytes: A modified Poisson-Nernst-Planck approach," *The Journal of Physical Chemistry C*, vol. 118, no. 11, pp. 5716–5724, 2014.

[104] X. Jiang, J. Huang, H. Zhao, B. G. Sumpter, and R. Qiao, "Dynamics of electrical double layer formation in room-temperature ionic liquids under constant-current charging conditions," *Journal of Physics: Condensed Matter*, vol. 26, no. 28, 2014.

[105] J. Wu, T. Jiang, D. en Jiang, Z. Jin, and D. Henderson, "A classical density functional theory for interfacial layering of ionic liquids," *Soft Matter*, vol. 7, no. 23, 2011.

[106] D. en Jiang, D. Meng, and J. Wu, "Density functional theory for differential capacitance of planar electric double layers in ionic liquids," *Chemical Physics Letters*, vol. 504, pp. 153–158, 2011.

[107] V. Lockett, R. Sedev, and J. Ralston, "Differential capacitance of the electrical double layer in imidazolium-based ionic liquids: Influence of potential, cation size, and temperature," *The Journal of Physical Chemistry C*, vol. 112, no. 19, pp. 7486–7495, 2008.

[108] V. Lockett, M. Horne, R. Sedev, T. Rodopoulos, and J. Ralston, "Differential capacitance of the double layer at the electrode/ionic liquids interface," *Physical Chemistry Chemical Physics*, vol. 12, no. 39, pp. 12499–12512, 2010.

[109] M. T. Alam, M. M. Islam, T. Okajima, and T. Ohsaka, "Measurements of differential capacitance in room temperature ionic liquid at mercury, glassy carbon and gold electrode interfaces," *Electrochemistry Communications*, vol. 9, no. 9, pp. 2370–2374, 2007.

[110] M. T. Alam, M. M. Islam, T. Okajima, and T. Ohsaka, "Measurements of differential capacitance at mercury/room-temperature ionic liquids interfaces," *The Journal of Physical Chemistry C*, vol. 111, no. 49, pp. 18326–18333, 2007.

[111] M. T. Alam, M. M. Islam, T. Okajima, and T. Ohsaka, "Capacitance measurements in a series of room-temperature ionic liquids at glassy carbon and gold electrode interfaces," *The Jounal of Physical Chemistry C*, vol. 112, no. 42, pp. 16600–16608, 2008.

[112] M. T. Alam, M. M. Islam, T. Okajima, and T. Ohsaka, "Ionic liquid structure dependent electrical double layer at the mercury interface," *The Journal of Physical Chemistry C*, vol. 112, no. 7, pp. 2601–2606, 2008.

[113] M. T. Alam, M. M. Islam, T. Okajima, and T. Ohsaka, "Electrical double layer in mixtures of room-temperature ionic liquids," *The Journal of Physical Chemistry C*, vol. 113, no. 16, pp. 6596–6601, 2009.

[114] M. M. Islam, M. T. Alam, and T. Ohsaka, "Electrical double-layer structure in ionic liquids: A corroboration of the theoretical model by experimental results," *The Journal of Physical Chemistry C*, vol. 112, no. 42, pp. 16568–16574, 2008.

[115] M. M. Islam, M. T. Alam, T. Okajima, and T. Ohsaka, "Electrical double layer structure in ionic liquids: An understanding of the unusual capacitance-potential curve at a nonmetallic electrode," *The Journal of Physical Chemistry C*, vol. 113, no. 9, pp. 3386–3389, 2009.

[116] T. Pajkossy and D. M. Kolb, "The interfacial capacitance of Au(100) in an ionic liquid, 1-butyl-3-methyl-imidazolium hexafluorophosphate," *Electrochemistry Communications*, vol. 13, no. 3, pp. 284–286, 2011.

[117] B. Roling, M. Drüschler, and B. Huber, "Slow and fast capacitive process taking place at the ionic liquid/electrode interface," *Faraday Discussions*, vol. 154, pp. 303–311, 2012.

[118] M. Drüschler, N. Borisenko, J. Wallauer, C. Winter, B. Huber, F. Endres, and B. Roling, "New insights into the interface between a single-crystalline metal electrode and an extremely pure ionic liquid: slow interfacial processes and the influence of temperature on interfacial dynamics," *Physical Chemistry Chemical Physics*, vol. 14, no. 14, pp. 5090–5099, 2012.

[119] Y. Yasui, Y. Kitazumi, H. Mizunuma, N. Nishi, and T. Kakiuchi, "A comparison of the ultraslow relaxation processes at the ionic liquid|water interface for three hydrophobic ionic liquids," *Electrochemistry Communications*, vol. 12, no. 11, pp. 1179–1482, 2010.

[120] T. Kakiuchi, Y. Yasui, Y. Kitazumi, and N. Nishi, "Voltammetric manifestation of the ultraslow dynamics at the interface between water and an ionic liquid," *ChemPhysChem*, vol. 11, no. 13, pp. 2912–2918, 2010.

[121] R. Costa, C. M. Pereira, and A. F. Silva, "Dicationic ionic liquid: Insight in the electrical double layer structure at mercury, glassy carbon and gold surfaces," *Electrochimica Acta*, vol. 116, pp. 306–313, 2014.

[122] L. E. Barrosse-Antle, A. M. Bond, R. G. Compton, A. M. O'Mahony, E. I. Rogers, and D. S. Silvester, "Voltammetry in room temperature ionic liquids: Comparisons and contrasts with conventional electrochemical solvents," *Chemistry, an Asian Journal*, vol. 5, no. 2, pp. 202–230, 2010.

[123] F. Endres, "Ionic liquids: Solvents for the electrodeposition of metals and semiconductors," *ChemPhysChem*, vol. 3, pp. 144–154, 2002.

[124] L. Lin, Y. Wang, J. Yan, Y. Yuan, J. Xiang, and B. Mao, "An in situ STM study on the long-range surface restructuring of Au(111) in a non-chloroaluminumated ionic liquid," *Electrochemistry Communications*, vol. 5, pp. 995–999, 2003.

[125] M. Mezger, H. Schröder, H. Reichert, S. Schramm, J. S. Okasinski, S. Schöder, V. Honkimäki, M. Deutsch, B. M. Ocko, J. Ralston, M. Rohwerder, M. Stratmann, and H. Dosch, "Molecular layering of fluorinated ionic liquids at a charged sapphire (0001) surface," *Science*, vol. 322, no. 5900, pp. 424–428, 2008.

[126] N. Nishi, Y. Yasui, T. Uruga, H. Tanida, T. Yamada, S. chi Nakayama, H. Matsuoka, and T. Kakiuchi, "Ionic multilayers at the free surface of an ionic liquid, trioctylmethylammonium bis(nonafluorobutanesulfonyl)amide, probed by x-ray reflectivity measurements," *Journal of Chemical Physics*, vol. 132, no. 16, 2010.

[127] T. Cremer, M. Killian, J. M. Gottfried, N. Paape, P. Wasserscheid, F. Maier, and H.-P. Steinrück, "Physical vapor deposition of [EMIM][Tf_2N]: A new approach to the modification of surface properties with ultrathin ionic liquid films," *ChemPhysChem*, vol. 9, no. 15, pp. 2185–2190, 2008.

[128] T. Cremer, M. Stark, A. Deyko, H.-P. Steinrück, and F. Maier, "Liquid/solid interface of ultrathin ionic liquid films: [C_1C_1Im][Tf_2N] and [C_8C_1Im][Tf_2N] on Au(111)," *Langmuir*, vol. 27, no. 7, pp. 3662–3671, 2011.

[129] S. Bovio, A. Podestà, P. Milani, P. Ballone, and M. G. D. Pópolo, "Nanometric ionic-liquid films on silica: a joint experimental and computational study," *Journal of Physics: Condensed Matter*, vol. 21, no. 42, 2009.

[130] Y. Min, M. Akbulut, J. R. Sangoro, F. Kremer, R. K. Prud'homme, and J. Israelachvili, "Measurement of forces across room temperature ionic liquids between mica surfaces," *The Journal of Physical Chemistry C*, vol. 113, no. 37, pp. 16445–16449, 2009.

[131] Y. Yokota, T. Harada, and K. ichi Fukui, "Direct observation of layered structures at ionic liquid/solid interfaces by using frequency-modulation atomic force microscopy," *Chemical Communications*, vol. 46, no. 45, pp. 8627–8629, 2010.

[132] S. Perkin, L. Crowhurst, H. Niedermeyer, T. Welton, A. M. Smith, and N. N. Gosvami, "Self-assembly in the electrical double layer of ionic liquids," *Chemical Communications*, vol. 47, no. 23, pp. 6572–6574, 2011.

[133] R. Hayes, N. Borisenko, M. K. Tam, P. c. Howlett, F. Endres, and R. Atkin, "Double layer structure of ionic liquids at the Au(111) electrode interface: An atomic force microscopy investigation," *The Journal of Physical Chemistry C*, vol. 115, no. 14, pp. 6855–6863, 2011.

[134] M. Gnahm, T. Pajkossy, and D. Kolb, "The interface between Au(111) and an ionic liquid," *Electrochimica Acta*, vol. 55, no. 21, pp. 6212–6217, 2010.

[135] F. Endres, N. Borisenko, S. Z. E. Abedin, R. Hayes, and R. Atkin, "The interface ionic liquid(s)/electrode(s): *In situ* STM and AFM measurements," *Faraday Discussions*, vol. 154, pp. 221–233, 2012.

[136] X. Zhang, Y.-X. Zhong, J.-W. Yan, Y.-Z. Su, M. Zhang, and B.-W. Mao, "Probing double layer structures of Au(111)-$BMIPF_6$ ionic liquid interfaces from potential-dependent AFM force curves," *Chemical Communications*, vol. 48, pp. 582–584, 2012.

[137] R. Atkin, N. Borisenko, M. Drüschler, F. Endres, R. Hayes, B. Huber, and B. Roling, "Structure and dynamics of the interfacial layer between ionic liquids and electrode materials," *Journal of Molecular Liquids*, vol. 192, pp. 44–54, 2014.

[138] C. Nanjundiah, S. F. McDevitt, and V. R. Koch, "Differential capacitance measurements in solvent-free ionic liquids at Hg and C interfaces," *Journal of the Electrochemical Society*, vol. 144, no. 10, pp. 3392–3397, 1997.

[139] P. Lozano and M. Martínez-Sánchez, "Ionic liquid ion sources: characterization of externally wetted emitters," *Journal of Colloid and Interface Science*, vol. 282, pp. 415–421, 2005.

[140] T. M. Coles, T. P. Fedkiw, and P. C. Lozano, "Investigating ion fragmentation in electrospray thruster beams," in *48th AIAA/ASME/SAE/ASEE Joint Propulsion Conference & Exhibit*, (Atlanta, GA), 2012.

[141] T. M. Coles and P. C. Lozano, "Investigating efficiency losses from solvated ion fragmentation in electrospray thruster beams," in *49th AIAA/ASME/SAE/ASEE Joint Propulsion Conference*, (San Jose, CA), 2013.

[142] P. Lozano and M. Martínez-Sánchez, "On the dynamic response of externally wetted ionic liquid ion sources," *Journal of Physics D: Applied Physics*, vol. 38, no. 14, pp. 2371–2377, 2005.

[143] P. Lozano, M. Martínez-Sánchez, and J. M. Lopez-Urdiales, "Electrospray emission from non-wetting flat dielectric surfaces," *Journal of Colloid and Interface Science*, vol. 276, no. 2, pp. 392–399, 2004.

[144] N. Brikner and P. C. Lozano, "The role of upstream distal electrodes in mitigating electrochemical degradation of ionic liquid ion sources," *Applied Physics Letters*, vol. 101, no. 19, 2012.

[145] S. M. Arestie, "Porous material and process development for electrospray propulsion applications," Master's thesis, Massachusetts Institute of Technology. Department of Aeronautics and Astronautics, Cambridge, MA, 2014.

[146] T. F. Baumann, M. A. Worsley, T. Y.-J. Han, and J. H. Satcher Jr., "High surface area carbon aerogel monoliths with hierarchical porosity," *Journal of Non-Crystalline Solids*, vol. 354, pp. 3513–3515, 2008.

[147] C. Largeot, C. Portet, J. Chmiola, P.-L. Taberna, Y. Gogotsi, and P. Simon, "Relation between the ion size and pore size for an electric double-layer capacitor," *Journal of the American Chemical Society*, vol. 130, no. 9, pp. 2730–2731, 2008.

[148] A. M. O'Mahony, D. S. Silvester, L. Aldous, C. Hardacre, and R. G. Compton, "Effect of water on the electrochemical window and potential limits of room-temperature ionic liquids," *Journal of Chemical and Engineering Data*, vol. 53, no. 12, pp. 2884–2891, 2008.

[149] S. Liu, W. Liu, Y. Liu, J.-H. Lin, X. Zhou, M. J. Janik, R. H. Colby, and Q. Zhang, "Influence of imidazolium-based ionic liquids on the performance of ionic polymer conductor network composite actuators," *Polymer International*, vol. 59, no. 3, pp. 321–328, 2010.

[150] J. M. Slattery, C. Daguenet, P. J. Dyson, T. J. Schubert, and I. Krossing, "How to predict the physical properties of ionic liquids: A volume-based approach," *Angewandte Chemie International Edition*, vol. 46, pp. 5384–5388, 2007.

[151] H. Weingärtner, "The static dielectric constant of ionic liquids," *Zeitschrift für Physikalische Chemie*, vol. 220, no. 10, pp. 1395–1405, 2006.

[152] C. Fucetola. Private Communication.

[153] D. Krejci. Private Communication.

[154] A. Yochelis, M. B. Singh, and I. Visoly-Fisher, "Coupling bulk and near-electrode interfacial nanostructuring in ionic liquids," *Chemistry of Materials*, vol. 27, no. 12, pp. 4169–4179, 2015.

[155] A. A. Lee, D. Vella, S. Perkin, and A. Goriely, "Are room-temperature ionic liquids dilute electrolytes?," *Journal of Physical Chemistry Letters*, vol. 6, no. 1, pp. 159–163, 2015.

[156] J. Vatamanu, Z. Hu, and D. Bedrov, "Increasing energy storage in electrochemical capacitors with ionic liquid electrolytes and nanostructured carbon electrodes," *The Journal of Physical Chemistry Letters*, vol. 4, no. 17, pp. 2829–2837, 2013.

[157] E. Warburg, "Ueber das verhalten sogenannter unpolarisirbarer elektroden gegen wechselstrom," *Annalen der Physik und Chemie*, vol. 67, no. 3, 1899.

[158] S. R. Taylor and E. Gileadi, "Physical interpretation of the warburg impedance," *Corrosion*, vol. 51, no. 9, pp. 664–671, 1995.

[159] J. C. Wang, "Realizations of generalized warburg impedance with rc ladder networks and transmission lines," *Journal of the Electrochemical Society*, vol. 134, no. 8, pp. 1915–1920, 1987.

[160] J. Fox and S. Weisberg, *An R Companion to Applied Regression*. Sage, 2011.

[161] T. Umecky, Y. Saito, and H. Matsumoto, "Direct measurements of ionic mobility of ionic liquids using the electric field applying pulsed gradient spin-echo nmr," *The Journal of Physical Chemistry B*, vol. 113, no. 25, pp. 8466–8468, 2009.

[162] M. A. Gebbie, M. Valtiner, X. Banquy, E. T. Fox, W. A. Henderson, and J. N. Israelachvili, "Ionic liquids behave as dilute electrolyte solutions," *Proceedings of the National Academy of Sciences*, vol. 110, no. 24, pp. 9674–9679, 2013.

[163] M. Y. Lui, L. Crowhurst, J. P. Hallett, P. A. Hunt, H. Niedermeyer, and T. Welton, "Salts dissolved in salts: ionic liquid mixtures," *Chemical Science*, vol. 2, no. 8, 2011.

[164] H. Weingärtner, "Understanding ionic liquids at the molecular level: Facts, problems, and controversies," *Angewandte Chemie*, vol. 47, no. 4, pp. 654–670, 2008.

[165] S. Perkin, M. Salanne, P. Madden, and R. Lynden-Bell, "Is a stern and diffuse layer model appropriate to ionic liquids at surfaces?," *Proceedings of the National Academy of Sciences*, vol. 110, no. 44, p. E4121, 2013.

[166] M. A. Gebbie, M. Valtiner, X. Banquy, W. A. Henderson, and J. N. Israelachvili, "Reply to perkin et al.: Experimental observations demonstrate that ionic liquids form both bound (stern) and diffuse electric double layers," *Proceedings of the National Academy of Sciences*, vol. 110, no. 24, p. E4122, 2013.

[167] M. A. Gebbie, H. A. Dobbs, M. Valtiner, and J. N. Israelachvili, "Long-range electrostatic screening in ionic liquids," *Proceedings of the National Academy of Sciences*, vol. 112, no. 24, pp. 7432–7437, 2015.

[168] H. Kuninaka, "Round-trip deep space maneuver of microwave discharge ion engines onboard HAYABUSA explorer," in *32nd International Electric Propulsion Conference*, (Wiesbaden, Germany), 2011.

[169] B. Hirschorn, M. E. Orazem, B. Tribollet, V. Vivier, I. Frateur, and M. Musiani, "Determination of effective capacitance and film thickness from constant-phase-element parameters," *Electrochimica Acta*, vol. 55, no. 21, pp. 6218–6227, 2010.

[170] C. J. Wen, B. A. Boukamp, R. A. Huggins, and W. Weppner, "Thermodynamic and mass transport properties of "LiAl"," *Journal of the Electrochemical Society*, vol. 126, no. 12, pp. 2258–2266, 1979.

[171] J. Li, X. Xiao, F. Yang, M. W. Verbrugge, and Y.-T. Cheng, "Potentiostatic intermittent titration technique for electrodes governed by diffusion and interfacial reaction," *The Journal of Physical Chemistry C*, vol. 116, no. 1, pp. 1472–1478, 2012.

[172] F. G. Cottrell, "Residual current in galvanic polarization regarded as a diffusion problem," *Zeitschrift für Physikalische Chemie*, vol. 42, pp. 385–431, 1903.

[173] J. C. Myland and K. Oldham, "Cottrell's equation revisited: An intuititve, but unreliable, novel approach to the tracking of electrochemical diffusion," *Electrochemistry Communications*, vol. 6, no. 4, pp. 344–350, 2004.

[174] K. Gmucová, *A review of non-Cottrellian diffusion towards micro-and nano-structured electrodes*. INTECH Open Access Publisher, 2012.

[175] T. M. Nahir and R. P. Buck, "Modified cottrell behavior in thin layers: applied voltage steps under diffusion control for constant-resistance systems," *Journal of Electroanalytical Chemistry*, vol. 341, no. 1–2, pp. 1–14, 1992.

[176] N. Nishi, A. Hashimoto, E. Minami, and T. Sakka, "Electrocapillarity and zero-frequency differential capacitance at the interface between mercury and ionic liquids measured using the pendant drop method," *Physical Chemistry Chemical Physics*, vol. 17, no. 7, pp. 5219–5226, 2015.

[177] M. Chu, M. Miller, and P. Dutta, "Crowding and anomalous capacitance at an electrode-ionic liquid interface observed using operando x-ray scattering," *ACS Central Science*, vol. 2, no. 3, pp. 175–180, 2016.

[178] J. Song. Private Communication.

[179] M. Hahn, A. Würsig, R. Gallay, P. Novák, and R. Kötz, "Gas evolution in activated carbon/propylene carbonate based double-layer capacitors," *Electrochemistry Communications*, vol. 7, pp. 925–930, 2005.